UNIVERSITA' DI ROMA
TOR VERGATA

*Dottorato di ricerca in Astronomia - XVII Ciclo*

# Physics and Cosmology of dark energy

*Supervisor*: Prof. Luca Amendola
*Tutor*: Prof. Roberto Buonanno

*Ph.D. thesis of* :
**Claudia Quercellini**

Figure 1: Cornelia Parker, *Cold Dark Matter* : *an exploded view* [London, Tate Modern Gallery].

# Contents

# Introduction

Seven years after the first observational hints from the Supernovae Ia Hubble diagram about the existence of a dominant component of unclustered matter with negative pressure (Riess et al. 1998; Perlmutter et al. 1999), the so-called dark energy or quintessence (Wetterich 1988; Ratra & Peebles 1988; Caldwell et al. 1998), there are still very few indications as to its nature. The main reason, perhaps, is that we lack any specific theoretical suggestion on the properties of the dark energy, i.e. on its self-interaction potential and on how it interacts with the other cosmological components. At first stage, all we can do is to explore a wide range of phenomenological models specified by the potential and the coupling to the other fields in order to provide an overall best fit to the current data. But on the other hand the probed presence of this new dark form of energy (currently dominating the expansion of the Universe) needs a much more accurate analysis than a general phenomenological description. The comprehension of this directely-undetectable component is not just a matter of cosmology, but involves the understanding of its physical origin and meaning. This is what makes the "dark energy problem" now so worth investigating: a proper dark energy model must reconcile the cosmological evolution with the fundamental theories of particle physics. In fact, to investigate its physical properties the dark energy is often represented by a scalar field that rolls on its potential. In addition, due to its dark nature, it is amazing that cosmological observations now can tell us much more about dark energy than what laboratory experiments can. Fortunately, there are now several cosmological observations that are at least potentially able to put stringent constraints on the nature of dark energy.

As with any other fundamental field, the dark energy can be characterized by how it interacts with itself and with the other fields. In other words, it can be characterized by its potential and couplings. While there have been several papers that tried to constrain the potential or the equation of state of the dark energy (Amendola 2000; Baccigalupi et al. 2002; Corasaniti & Copeland 2002; Bean & Melchiorri 2002), the study of its coupling has been relatively scarce, although it has been suggested several times that we cannot expect a vanishing coupling (Carroll 1998).

The observations that can reveal dark energy are varied, and can be classified into those that take into account only the evolution of the homogeneous background and those that investigate the growth of perturbations. Up to few years ago the latter class was poor of results, due to the large errors in the observations of the growth of clustering. But now, with the new large surveys, such as Sloan Digital Sky survey and the Two degree Field Galaxy Redshift Survey, the prospects are really interesting.

The background observations all reduce essentially to the use of a standard measure, either candles, rods or clocks: any of this standard is in fact subject to a geometric apparent variation when seen at high redshift that depend on cosmology. The standard candles have been employed in the method based on the supernovae Ia, while standard rods are assumed in the Alcock-Paczinsky method (or rather, a standard isotropy, see e.g. Calvão et al. (2002b), in the lensing statistics (e.g. Cooray & Huterer (1999), Giovi & Amendola (2001)) and in the size of the sound horizon at decoupling as detected from the CMB acoustic peaks (see e.g. Doran et al. (2001)). They all rely on the fact that the proper distance to an object at redshift $z$ depends on cosmology. It is clear therefore that all quantities that depend on distance, like luminosity, angular sizes, ages, also depend on cosmology. For instance, the method based on the Supernovae Ia Hubble diagram determines the distance to a supernova (whose absolute magnitude $M$ has been inferred and corrected by local observations), via the distance modulus

$$m - M = 5 \log dL(z) + 25$$

(plus possibly a $K$-correction) and then compares this value to the theoretical luminosity distance $dL(z) = r(z)(1+z)$ to find the best fit in terms of the parameters. The main advantages with this approach are that one can observe $r(z)$ at different redshifts, depending on the object. So far, SNe Ia have been seen up to $z > 1$ (with a couple of SNe beyond this), but future experiments can extend the observations up to $z > 2$ and to a much extended dataset. The distance of the sound horizon at decoupling, expressed as the angular diameter distance $d_A(z) = r(z)/(1+z)$ , in turn, reaches $z > 1000$ , the redshift of the last scattering surface. The crucial point is that $r(z)$depends on the parameters $in\ a\ different\ way\ for\ different\ redshifts$. Therefore, observations at low redshift, like the SNIa, and at high redshift, like the sound horizon at decoupling, can give orthogonal constraints, thereby determining with high precision the cosmological parameters.

For what concerns the investigation of growth of perturbations (and the consequent structure formation) the analysis must in turn be split into two regimes: the linear and the non-linear regime. The first one is valid when the perturbations around the background value are small and their evolution can be treated analytically with a first order perturbative analysis. When the perturbations than detach from the background expansion collapsing via gravitational instability they reach the non-linear regime. Here either the analytic treatment needs a second order perturbative analysis or one needs to perform numerical techniques, like N-body codes, in order to follow the trajectories of the single particles in the collapse. As we will see, dark energy not only affects the background expansion, but also the growth of matter perturbations and it generates its own perturbations modifying the gravitational clustering in a way that is not easily predictable.

This thesis is structured as follows: in the first Chapter we will review the state of art of dark energy and the basic equations that will be used in the next Chapters; in the second Chapter we will introduce dark energy modeled as a scalar field with a potential and interactions; taking into account both the modified background evolution and the growth of linear perturbations, the third Chapter

presents the constraints on the main parameters in an uncoupled dark energy model from galaxy surveys, while the fourth Chapter analyses the effect of dark energy on the Cosmic Microwave Background radiation in a more general coupled model; in the fifth Chapter we will present the first step beyond linearity, investigating the third order moment of the galaxy distribution in several dark energy models; the sixth Chapter completes the non-linear analysis with a full numerical treatment in an N-body code, where clustering properties such as mass function and density profiles are derived; the seventh Chapter concludes with some hints about the backreaction of dark energy perturbations and prospects.
In all the thesis we will use $\hbar = c = 1$.

# Chapter 1

# A bit of cosmology

A very remarkable and philosophical feature of the present epoch, and in particular of the last few years, is the emergence of Cosmology as a mature science in which most of the questions have a precise answer. These answers are possible in the context of the Standard Cosmological Model (SCDM), that arised in the second half of the last century with the discovery of the Cosmic Microwave Background, but have their theoretical foundation in General Relativity.
Within this theory there are four main SCDM strong pillars: 1)The Cosmological Principle, introduced by Einstein in 1917, that states the homegeneity and isotropy of the Universe; 2)The Hubble law, discovered by Hubble in 1929, that is the relation between galaxy recession velocity (and acceleration) and distance; 3)The CMB, corresponding to a blackbody radiation at temperature T=2.725 K, accidentally discovered by Penzias and Wilson in 1964, whose mean isotropy

supports the cosmological principle and whose small anisotropies in the spatial distribution of the sky temperature contain a wealth of information of the cosmological parameters; 4)The light elements cosmological abundances, namely $^1$H, $^2$D,$^3$He, $^4$He and $^7$Li, originated during the primordial Big Bang Nucleosynthesis (BBN), whose theoretical analysis was pioneered by G. Gamow in 1948. To this list it should be added the analysis of the Large Scale Structure based on galaxy catalogs, recently improved by means of the Two degree Field Galaxy Redshift Survey (2dFGRS) and the Sloan Digital Sky Survey (SDSS).

## 1.1 Basic equations

Despite its weakness with respect to other fundamental forces, gravity is the driving force of the Cosmos, leading to the expansion and the formation of structures that we observe today. Gravity is well described by Einstein's General Relativity, which consists of two basic elements: *the equivalence principle* and *Einstein's field equations*.

In its Newtonian version the equivalence principle amounts to the identification of the gravitational mass entering Newton's gravity and the inert mass entering the second law of Newtonian mechanics. The most accurate test that all bodies fall with the same acceleration in a gravitational field comes from the comparison of the accelerations of the Moon and the Earth as they fall around the Sun by means of lunar laser ranging, and they agree to an accuracy of $1.5 \times 10^{-13}$ (Anderson & Williams 2001).

This led Einstein to formulate the relativistic version of the equivalence principle by identifying the gravitational field with the metric tensor $g_{\mu\nu}$ describing the geometry of the space-time manifold.

Einstein's field equations were derived by Hilbert & Einstein in 1916 and relate the geometry of the Universe to the energy source term of the gravitational field:

$$G_{\mu\nu} \equiv R_{\mu\nu} - \frac{1}{2} g_{\mu\nu} R = 8\pi G T_{\mu\nu} + \Lambda g_{\mu\nu}, \tag{1.1}$$

where $G_{\mu\nu}$ is the Einstein's tensor function of the Ricci tensor $R_{\mu\nu}$ and the metric, $T_{\mu\nu}$ is the stress-energy tensor and $\Lambda g_{\mu\nu}$ is the Cosmological Constant term.
The Cosmological Principle together with the equivalence principle dictates the geometry of the Universe given by the Robertson-Walker metric

$$ds^2 = -dt^2 + a(t)^2\Big[\frac{dr^2}{1-kr^2} + r^2(d\theta^2 + sin^2\theta d\phi^2)\Big], \tag{1.2}$$

where the function $a(t)$ is the scale factor, the constant $k = 1, 0, -1$ specifies the sign of the spatial curvature of the Universe, and $t$ is the cosmic time, that is the time measured by comoving observers which are at rest with respect to the expansion. The coordinates $r, \theta, \phi$ are spherical comoving coordinates meaning that comoving observers remain at rest in this coordinates.
The Cosmological Principle also restricts the form of the material content of the Universe. Since a perfect fluid can be characterised by its isotropy around observers comoving with the fluid, the stress-energy tensor for the material content must have the perfect fluid form

$$T_{\mu\nu} = pg_{\mu\nu} + (\rho + p)u_\mu u_\nu, \tag{1.3}$$

where $\rho$ e $p$ are the energy density and the pressure, and $u^\mu$ is the four velocity of the fluid.
Einstein's equations in a Robertson Walker metric leads to the Friedmann equation

$$H^2 = \frac{8\pi G}{3}\rho + \frac{1}{3}\Lambda - \frac{k}{a^2}, \tag{1.4}$$

where $H = \dot{a}/a$ is the Hubble parameter. Its present value $H_0$ is the Hubble constant, usually expressed in term of the adimensional number $h$, in the form $H_0 = 100\ h$ km s$^{-1}$ Mpc$^{-1}$.
From the covariant derivative of the stress-energy tensor

$$T^\mu_{\nu;\mu} = 0 \tag{1.5}$$

one obtains what can be expressed as the energy conservation equations for each component:

$$\dot{\rho} = -3H(\rho + p), \tag{1.6}$$

where the density $\rho$ is related to the pressure $p$ by the equation of state

$$p = w\rho. \tag{1.7}$$

The photons in the CMB as an ultrarelativistic plasma have $w = 1/3$, the cold non-relativistic matter $w = 0$ and the cosmological constant $w = -1$. Thus solving Eq.(1.4) together with Eq.(1.6) and Eq. (1.7) we can know the time evolution of the scale factor $a(t)$ and the energy density $\rho(t)$ with cosmic time.
In addition, the density parameters for each species are defined as $\Omega_i = 8\pi G\rho_i/3H^2$, where $\rho_c = 3H^2/8\pi G$ is the critical density corresponding to a flat Universe ($k = 0$) with $\Lambda = 0$. Moreover Eq.(1.4) can be rewritten as

$$\sum_i \Omega_i + \Omega_\Lambda - \frac{k}{a^2H^2} = 1, \tag{1.8}$$

including $\Omega_\Lambda = \Lambda/3H^2$. The flat Universes are those fulfilling the condition $\sum_i \Omega_i + \Omega_\Lambda = 1$.

## 1.2 Observational constraints

Recent developments in cosmology have been largely driven by huge improvement in quality, quantity and the scope of cosmological observations. The measurement of temperature anisotropy in the CMB has been arguably the most influential of these recent observational success stories. A glorious decade of CMB anisotropy measurments has been crowned by the data from the Wilkinson Microwave Anisotropy Probe (WMAP) of NASA. These observations have constrained theroretical scenarios and models more precisely.
The cosmological model can be broadly split into two distinct aspects: the nature and dynamics of the homogeneous background and the origin and evolution of perturbations leading to the large scale structure in the distribution of matter in the Universe. The most important cosmological constraints comes today not only from CMB pbservations, but also from Supernovae Ia luminosity distance and LSS. Here we review some of the most important experiments that pointed

out the existence of new dark forms of energy.

In 1929 Hubble discovered the law of expansion of the Universe by measuring

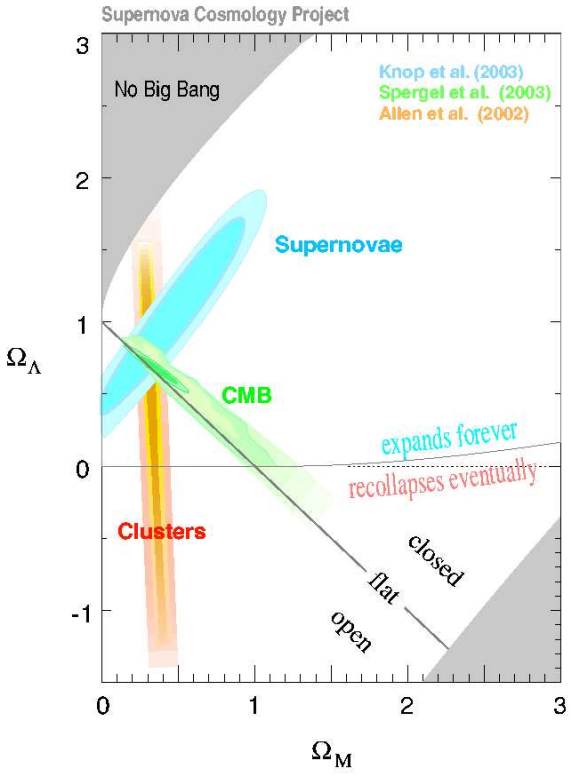


Figure 1.1: Matter density $\Omega_m$ vs. vacuum energy density $\Omega_\Lambda$, 68% and 95% C.L.. Contours for SNe Ia, clusters and CMB data (Supernova Cosmology Project).

distances to nearby galaxies. The slope of the relation between the distance and recession velocity is $H_0$ itself. Astronomers argued for decades on the systematic uncertainties in various methods and derived values over the wide range, 40 km $s^{-1}$ $Mpc^{-1}$ $< H_0 <$ 100 km $s^{-1}$ $Mpc^{-1}$. One of the most reliable results on the Hubble constant comes from the Hubble Space Telescope Key Project (Freedman et al. 2001) (hereafter HST). The group has used the empirical period-luminosity relations for Cepheid variable stars to obtain dis-

tances to 31 galaxies, and calibrated a number of secondary distance indicators (Type Ia Supernovae, Tully Fisher, surface brightness fluctuations and Type II Supernovae) measured over distances of 400 to 600 Mpc. They estimated $H_0 = 72 \pm 3(\text{statistical}) \pm 7(\text{systematic})$ km s$^{-1}$ Mpc$^{-1}$ ($1\sigma$ C.L.). It is remarkable that this result is in such good agreement with the result derived from the WMAP CMB and LSS measurements.

The relation between observed flux and the intrinsic luminosity of an object depends on the luminosity distance $d_L$, which in turn depends on cosmological parameters through an integral over the Hubble function,

$$d_L = (1+z) \int_0^z dz'/H(z'), \tag{1.9}$$

where $z = (1/a - 1)$ is the redshift. The peak luminosity of supernova of Type I (SNe Ia) can be used as an efficient distance indicator (Filippenko 2003). The favorite theoretical explanation for SNe Ia is the thermonuclear disruption of carbon-oxygen white dwarfs. Although not perfect standard candles, it has been demonstrated that by correcting for a relation between the light curve shape and the luminosity at maximum brightness, the dispersion of the measured luminosities can be greatly reduced. There are several possible systematic effects which may affect the accuracy of the SNe Ia as distance indicators, i.e. evolution with redshift and interstellar extinction in the host galaxy and in the Milky way, but there is no indication that any of these effects are significant for the cosmological constraints.

Two major projects, the "Supernova Cosmology Project" and the "High Supernova Search Team"(Perlmutter et al. (1999) and Riess et al. (1998) ), found evidence for an accelerating Universe, interpreted as due to a dark energy component. Recent results were obtained by Tonry et al (2003). The SNe Ia data alone can only constrain a combination of $\Omega_m$ and $\Omega_\Lambda$:

$$\Omega_\Lambda - 1.4\Omega_m = 0.35 \pm 0.14 \quad (1\sigma\ C.L.). \tag{1.10}$$

This degeneracy direction is almost orthogonal to the one inferred from the angular diameter distance at $z \sim 1100$ measured by the CMB (cf. Fig. 1.1). When

combined with the CMB data the best fit values are $\Omega_m \simeq 0.3$ and $\Omega_\Lambda \simeq 0.7$.
The existence of a Cosmic Microwave Background with present temperature around 5 K was theoretically predicted in 1948 by Gamow, Alpher and Hermann, as a necessary relic of a hot phase of the Universe, and later on accidentally discovered by Penzias and Wilson in 1964. Before recombination the baryons and the photons are tightly coupled, and the perturbations oscillate in the potential wells generated primarily by the dark matter perturbations. After decoupling the baryons are free to collapse into those potential wells. CMB carries a record of conditions at the time of decoupling, called primary anisotropies. In addition, it is affected by various processes as it propagates towards us, like the effect of a time-varying gravitational potential (the integrated Sachs-Wolfe effect), gravitational lensing, and scattering from ionized gas at low redshift. The detailed pattern of anisotropies ca be quantified by the angular power spectrum

$$C_l =< |a_{lm}|^2 >, \tag{1.11}$$

where the coefficients $a_{lm}$ are related to the CMB temperature distribution in the sky by means of its spherical harmonics expansion

$$\frac{\Delta T}{T}(\theta, \phi) = \sum_{lm} a_{lm} Y_{lm}(\theta, \phi). \tag{1.12}$$

This pattern depends on all of the cosmological parameters. In a typical cosmology, the anisotropy power spectrum features a flat plateau at large angular scales (small $l$), followed by a series of oscillatory features at higher angular scales, the first and most prominent being at around one degree ($l \simeq 200$). These acoustic peaks represent the oscillations of the photon-baryon fluid around the time of decoupling. The location of the first peak probe the spatial geometry, while the relative heights of the peaks probes the baryon density, but many other parameters combine to determine the overall shape.

The WMAP experiment (Bennett et al. 2003) has provided the most accurate results to date on the spectrum of CMB fluctuations (Hinshaw et al. 2003), with a precision determination of the temperature power spectrum up to $l \simeq 900$, shown in Fig. 1.2, and the first detailed mesurement of the correlation spectrum

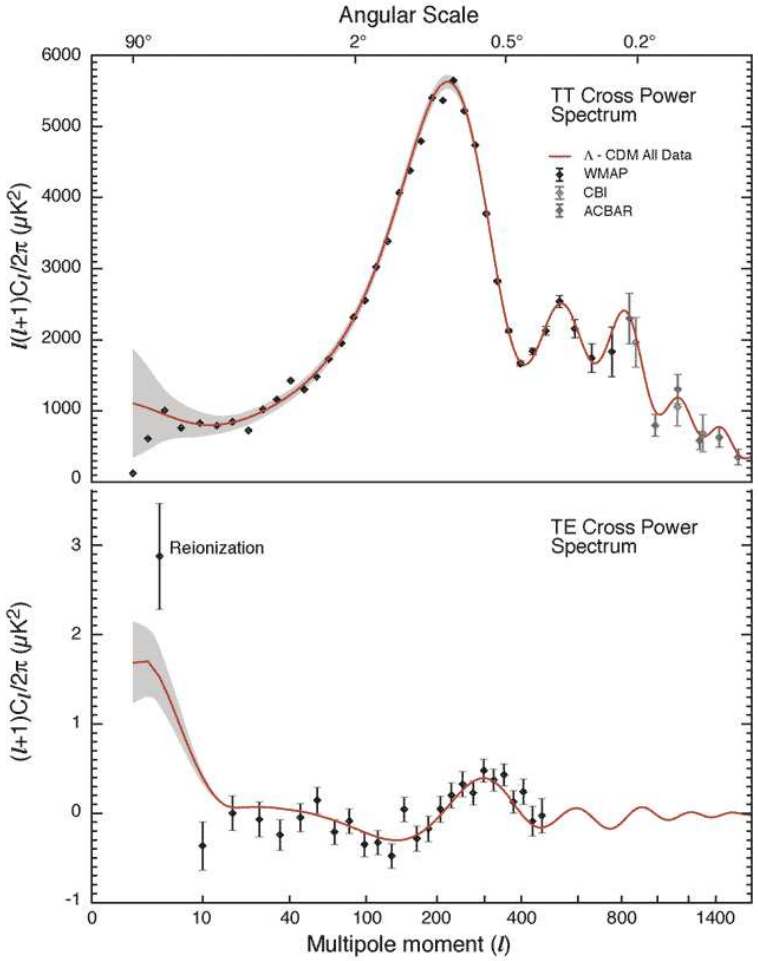


Figure 1.2: The dark points are the angular power spectrum of the CMB as measured by the WMAP satellite. The green ones are from the CBI experiment and the blue ones are from ACBAR. The solid line shows the prediction from the best fitting $\Lambda$ CDM model. The error bars on the data points indicate the observational errors, while the shaded region indicate the statistical uncertainty from being able to observe only one microwave sky, known as cosmic variance. The same applies to the bottom panel which represents the measurement of the correlation spectrum between temperature and polarization.

between temperature and polarization (Kogut et al. 2003), while the correlation having first being detected by DASI (Kovac et al. 2002). These are consistent with the values of the parameters that come from SNe Ia experiments ( Fig. 1.1). WMAP provides an exquisite measurements of the location of the first acous-

tic peak, which directly probes the spatial geometry and yields a total density $\Omega_{tot} = \sum \Omega_i + \Omega_\Lambda$ of

$$\Omega_{tot} = 1.02 \pm 0.02, \tag{1.13}$$

consistent with spatial flatness and compeletly excluding significantly curved Universes if one assumes a fairly strong prior on $H_0$ coming from experiments as the HST. It also gives a precision measurement of the age of the Universe. It gives a baryon density consistent with that coming from nucleosynthesis. However, to obtain the most powerful constraints, other data sets can be considered in addition to WMAP, with shorter-scale CMB measurements from CBI and ACBAR, and the galaxy power spectrum from 2df and SDSS. The value of $\Omega_m$ is beginning to be pinned down with some precision, with most observations indicating a value around 0.3, including the cluster number density, the mass-to-light ratio and the gravitational lensing.
If the data are to be explained, all these observations seem to affirm the urgent need for both dark matter and dark energy.

## 1.3 Cosmological constant?

From these observations we therefore infer the existence of a dark energy $\rho_\Lambda$ smoothly distributed through space, at least at the cluster scale (so that it does not influence the local motions of galaxies and clusters), with $\Omega_\Lambda \simeq 0.7$. SNe Ia measurements have provided evidence that the Universe is accelerating, i.e. that $\ddot{a} > 0$. The significance of this discovery can be appreciated by rewriting the Friedmann equation (1.4) after multiplying by $a^2$:

$$\dot{a}^2 = \frac{8\pi G}{3} a^2 \rho, \tag{1.14}$$

where we considered $k = 0$ and $\rho = \rho_i + \rho_\Lambda$. The energy density in matter (non-relativistic particles) diminishes as the number density is diluted by expansion, so that $\rho_m \propto a^{-3}$. If particles are relativistic, and thus classified as radiation, they

are both diluted in number density and have their individual energies redshift as $a^{-1}$, so that $\rho_\gamma \propto a^{-4}$. For either of these conventional sources of energy density, the right-hand side of Eq. (1.14) will be decreasing in an expanding Universe, so that $\dot{a}$ will be decreasing. The SNe Ia data therefore imply that, to make the Universe accelerate, the dark energy must be varying slowly with time (redshifting away more slowly than $a^{-2}$) as well as with space. Furthermore if we look at the space-space part of the Einstein equations (1.1)

$$\ddot{a} = -4\pi G a^2(\rho + 3p), \tag{1.15}$$

it comes out that in order to have acceleration today we need a dominant component with an equation of state $w < -1/3$.

There is a straightforward candidate for a dark energy component: vacuum energy or the cosmological constant (for review see Witten (2000)). The distinguishing feature of vacuum energy is that it is a minimum amount of dark energy in any region, strictly constant through spacetime and $w = -1$. To match the data, we require a vacuum energy

$$\rho_\Lambda^{obs} \sim (10^{-3} eV)^4. \tag{1.16}$$

The idea that the dark energy density is simply a constant inherent in the fabric of spacetime is in excellent agreement with the data, but raises two very difficult questions: why is it so much smaller than what we would think of as its natural value (the cosmological constant problem)? And why are the matter and the vacuum energy densities approximately equal today (the coincidence problem)? The first question is important even if the dark energy is not a cosmological constant, although a non-zero value for the vacuum energy makes its smallness perhaps even more puzzling than if it were simply zero. The crucial point is that there is no principle or symmetry which would prefer that the vacuum energy have the value zero than any other value. In richer theories there may be such principles, such as supersymmetry or conformal invariance; the observed Universe, however, shows no sign of such symmetries, so they must be severly broken if they exist at all. Hence, it requires fine-tuning to obtain a vanishing $\rho_\Lambda$.

We are unable to reliably calculate the expected vacuum energy in the real Universe, or even in some specific field theory such as the Standard Model of particle physics. At best we can offer order of magnitude estimates for the contributions for different sectors. In the Standard Model there are two important contributions from non-vanishing condensates in the vacuum: the potential energy of the Higgs field, expected to be of the order $(10^{11}$ eV$)^4$ and a QCD energy density in the condensate of quark bilinears responsible for chiral symmetry breaking, expected to be of the order $(10^8 eV)^4$. There is also a contribution from the quantum mechanical zero-point vacuum fluctuations of each field in the model. This contribution actually diverges and it is necessary to introduce a cutoff and hope that a more complete theory will eventually provide a physical justification for doing so. If this cutoff is the Planck scale $M_p = 10^{18} GeV$ we obtain a vacuum energy of the order of $(10^{27} eV)^4$. In addition there is no reason to exclude a bare classical contribution to the cosmological constant at the Planck scale $\rho_\Lambda \sim (10^{18} GeV)^4$. Since there is no apparent relationship between the values of the disparate contributions, we expect the total vacuum energy to be of the same order as that of the largest components:

$$\rho_\Lambda^{th} \sim (10^{27} eV)^4. \tag{1.17}$$

There is clearly a mismatch between the theoretical prediction and the observed value (1.16):

$$\rho_\Lambda^{th} \sim 10^{120} \rho_\Lambda^{obs}, \tag{1.18}$$

which is the famous 120 orders of magnitude discrepancy that makes the cosmological constant problem such embarassing (although it is somewhat unfair to emphasise the factor $10^{120}$ which depends on the fact that in those units energy density has units of [energy]$^4$). There have been many suggested resolutions to the cosmological constant problem (see Sahni & Starobinsky (2000) for reviews), but to date none has seemed exceptionally compelling, and most researchers believe that the correct solution has yet to be found.

The second issue is the coincidence between the oserved vacuum energy (1.16) and

the current matter density. The relative balance of vacuum and matter changes rapidly as the Universe expands:

$$\frac{\Omega_\Lambda}{\Omega_m} = \frac{\rho_\Lambda}{\rho_m} \propto a^3. \tag{1.19}$$

As a consequence, at early times the vacuum energy was negligible in comparison to matter and radiation, while at late times the latters are negligible. There is only a brief epoch of the Universe's history during which it would be possible to witness the transition from domination by one type of component to another. It seems remarkable that we live during the short transitional period between these two eras. Another great surprise is the comparable magnitudes of the baryon density ($\Omega_b \simeq 0.04$) and the dark matter density. However it is important to keep in mind the crucial distinction between the coincidences relating the various matter components and the one relating matter and vacuum energy: the former are set once and for all by primordial processes and remain unchanged as the Universe evolves, while the latter holds true only during a certain era. Some scenario were invoked to explain it, such as models in which the dark energy density has always been proportional to the dark matter one (Tocchini-Valentini & Amendola (2002), Ferreira & Joyce (1998)).

## 1.4 A simple extended form of dark energy [I]

The cosmological constant is but one example of a form of energy which could drive an accelerated phase in the history of our Universe. Although the observational evidence for dark energy implies a component which is unclustered in space as well as slow-varying in time, we may still imagine that it is not perfectly constant. There are good reasons to consider dynamical dark energy as an alternative to an simple cosmological constant. First, a dynamical dark energy can be evolving slowly to zero, allowing for a solution to the cosmological constant problem which makes the ultimate vacuum energy vanish exactly. Second, it poses an intersting and challenging observational problem to study the evolution of the dark energy, from which we might learn something about the underlying physical

mechanism. Perhaps more intriguingly, allowing the dark energy to evolve opens the possibility of finding a dynamical solution to the coincidence problem.

A convenient parametrization of the recent behaviour of any such candidate comes from generalising the vacuum energy equation of state, as in Eq. (1.7). This would be thought as a phenomenological relation reflecting the current amount of pressure and energy density in dark energy. In particular, the parameter $w$ is not necessarily constant. However, given that there are an uncountable number of conceivable behaviours for the dark energy, a simple relation as Eq. (1.7) is a useful way to characterise its current state, even if , as we shall see in the next Chapters, some simple parametrization of the time dependence of $w$ has been proposed.

The equation of state parameter is connected directly to the evolution of the energy density and, thus, to the expansion of the Universe. From Eq. (1.6) it follows that this component evolves with the scale factor as

$$\frac{d\ln\rho}{d\ln a} = -3(1+w). \tag{1.20}$$

We can notice that, while the vacuum energy remains constant, here the energy density would actually decrease in time if $w > -1$ and increase in time if $w < -1$. Combining the Friedmann equation (1.4) with a zero cosmological constant and equation (1.20) we see that a flat Universe dominated by a component with constant $w$ will expand as

$$a \propto t^{2/3(1+w)}, \tag{1.21}$$

unless $w = -1$, for which the expansion will be exponential (while for $w < -1$, one should choose $t < 0$ in this expression).

What can we tell about the expected value of the equation of state parameter? It is hard to make statements about a component of energy about which we know so little. In general relativity it is conventional to restrict the possible energy-momentum tensors by imposing energy conditions. Fluids satisfying $\rho + 3p \geq 0$ or $w \geq -1/3$ are said to satisfy the "strong energy condition" (SEC). Another condition which is usually assumed to be sacrosant, but has recently, but has recently been called into question is the "weak energy condition" (WEC) $\rho + p \geq 0$

or $w \geq -1$. Given that the dark energy should have positive energy density to account for the necessary density to make the Universe flat, and negative pressure to explain the acceleration, a violation of the WEC would imply $w < -1$. Failure to satisfy the WEC can result in faster than exponential expansion for the Universe and in a cosmic "Big Rip". Current limits (Melchiorri et al. 2003) obtained by combining results from CMB with LSS data, the HST and luminosity measurements from SNe Ia give $-1.62 < w < -0.74$ at the 95% C.L..I t is

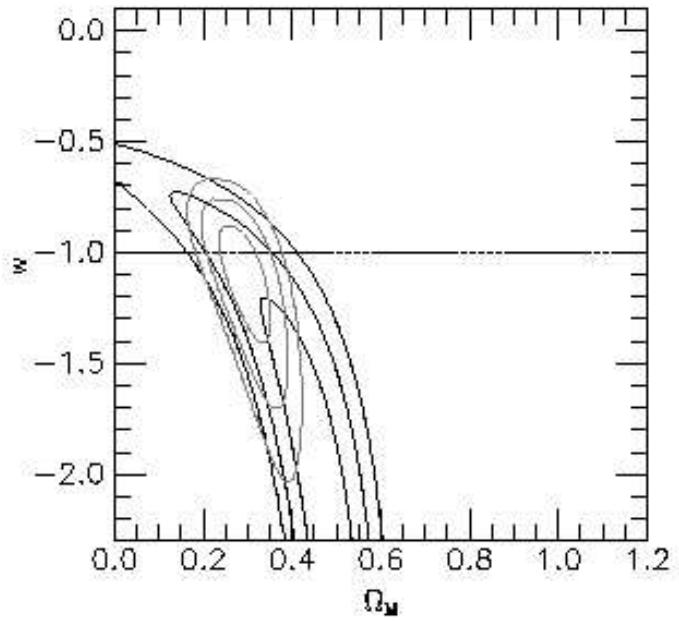


Figure 1.3: The SNe Ia contour plot from Riess et al. (2004).

straight forward to examine the cosmological consequences of a dark energy component which is strictly constant throughout space and evolving with any value of $w$. However any physical example of such a component will necessarily have fluctuations, as long as $w \neq -1$. It is therefore important to determine whether these fluctuations can lead to a catastrophic destabilization of the vacuum. Unfortunately, since Eq. (1.7) is a phenomenological description valid for a certain configuration rather than a true equation of state, specifying $w$ is not enough to sensibly discuss the evolution of perturbations, since $\delta p \neq w\delta\rho$. One should

better choose therefore a specific model.

# Chapter 2

# A "field" of interest

An important class of models of dynamical dark energy, is the one where dark energy is represented by a scalar field, usually called quintessence, named after the celestial fifth element of ancient philosophical thought. The idea is to use more or less the same mechanism of inflation, a scalar field rolling down towards the minimum of its potential, in order to obtain a late time acceleration epoch. Considering a scalar field instead of a phenomenological description of the dark energy by a simple constant or parametrised equation of state, has more basic motivations. A scalar field usually has got a physical meaning and can be related more easily to fundamental physics. In addition to that, as we will see in this Chapter, it can be characterised by a potential that allows interesting *tracking* solutions and may generate interactions with other components, which could never be analysed in a simple extended dark energy model. Furthermore, a scalar

field model is a dark energy model that garantees a complete general relativity perturbation analysis.

From now on we will consider a flat conformal metric

$$ds^2 = a^2(-d\tau^2 + \delta_{ij}dx^i dx^j), \tag{2.1}$$

where we introduce the conformal time $d\tau \equiv dt/a$.

## 2.1 When a scalar field is cosmological

A dark energy component can be represented by a scalar field which self-interacts through a suitable potential $V(\phi)$. The Lagrangian associated to such a scalar field results to be

$$L = \sqrt{-g}\Big[\frac{1}{2}\partial^\mu\phi\partial_\nu\phi - V(\phi)\Big], \tag{2.2}$$

where $g$ is the determinant of the metric. Its stress-energy tensor can be derived directly from the Lagrangian as

$$T^{\mu\nu} = \partial^\mu\phi\partial^\nu\phi - Lg^{\mu\nu}. \tag{2.3}$$

Comparing this expression to Eq. (1.3), we see that a cosmological scalar field is characterised by an energy density and a pressure equals to

$$\rho_\phi = T^0_0 = \frac{\dot\phi^2}{2a^2} + \nabla^2\phi + V(\phi); \qquad p_\phi = \frac{1}{3}T^i_i = \frac{\dot\phi^2}{2a^2} + \nabla^2\phi - V(\phi). \tag{2.4}$$

Since for a scalar field the sound velocity is always equal to the light velocity and observations seem to point out the homogeneity of dark energy at least up to the cluster scale, then the spatial variations of the scalar field, i.e. $\nabla^2\phi$, are considered to be vanishing.

Accordingly, the equation of state parameter for such a model is

$$w \equiv \frac{p_\phi}{\rho_\phi} = \frac{\dot\phi^2/2a^2 - V(\phi)}{\dot\phi^2/2a^2 + V(\phi)}, \tag{2.5}$$

which is time dependent and lays between $w = 1$ (when the kinetic term widely exceeds $V(\phi)$) and $w = -1$ (when the potential part dominates and mimics the

effect of a cosmological constant).

The actual behaviour of the scalar field depends on the potential, and, more precisely, on its equation of motion, which can be derived varying the Lagrangian (2.2) with respect to $\phi$:

$$\partial^\mu\phi\partial_\mu\phi = V'(\phi) \qquad \rightarrow \qquad \ddot{\phi} + 2H\dot{\phi} + a^2\partial_\phi V(\phi) = 0, \tag{2.6}$$

where dots represent derivation with respect to conformal time and the prime indicates the derivative with respect to the field. The cosmic expansion and the scalar field influence each other via the friction term $2H\dot{\phi}$, which couples this equation of motion to the Friedmann equation (1.4).

In order to get a good degree of homogeneity and an accelerated expansion today, the potential must reflect some features. First, the condition $w < -1/3$ translates into the request of a not too much steep potential, preferably with a minimum or a late-time plateau, in which

$$\dot{\phi}^2/2a^2 \ll V(\phi). \tag{2.7}$$

Second, if we require that the mass associated to the spatial fluctuations of the scalar field is tiny inside the horizon, i.e. $m_\phi \sim H_0 \sim 10^{-33}eV$, since $m_\phi \propto V''(\phi)$, we get a further motivation to consider potentials that are flat at present.

## 2.2 Appropriate potentials

To date, many investigations have considered scalar fields with potentials that asymptote gradually to zero. Some of them (like the Ratra & Peebles potential that we will analyse in more detail in the next Chapter, cf. Table 2.1) can have cosmologically interesting properties, including *tracking* behaviour that makes the current energy density widely independent of the initial conditions (Zlatev, Wang, & Steinhardt 1999). They can also be derived from physics model, such as dilaton, moduli of string theory or brane world cosmology (Pietroni 2003; Gasperini et al. 2002).

An extreme example of dark energy scalar field is provided by the exponential

potential $V = V_0 \exp(-\lambda\phi)$ (Ferreira & Joyce 1998; Wetterich 1988). In this case from a wide range of initial conditions the scalar field at some point reaches an actractor solution where the energy density parameter $\Omega_\phi$ is constant and depends on the parameters of the potential. In this model, if the attractor is reached at early time, the upper limit $\Omega_\phi < 0.2$ arises because of nucleosynthesis constraints which prevent the energy density in dark energy from being large initially, and some problem can be caused by the presence of an accelerating form of energy during the whole matter dominated era.

In the oscillating models (Dodelson et al. (2000), cf. Table 2.1) the potentials take the form of a decaying exponential with small perturbations superimposed $V = \exp(-\phi)(1 + \alpha cos(\phi))$. On average, the dark energy in such a model will track that of the dominant component: however there will be gradual oscillations from a negligible density to a dominant density and back, on a timescale set by the Hubble parameter.

| **Scalar field potential** | **Reference** |
|---|---|
| $V_0 \exp(-\lambda\phi)$ | Wetterich (1988), Ferreira & Joyce (1998) |
| $V_0/\phi^\alpha, \alpha > 0$ | Ratra & Peebles (1998) |
| $\mu^4(1 + cos(\phi))$ | Frieman et al. (1992) |
| $\exp(-\phi)(1 + \alpha cos(\phi))$ | Dodelson et al. (2000) |
| $V_0 \exp(\lambda\phi^2)/\phi^\alpha$ | Brax & Martin (2000) |
| $V_0(\exp(M_p/\phi) - 1)$ | Zlatev, Wang & Steinhardt (1999) |
| $V_0[(\phi - B)^\alpha + A] \exp(-\lambda\phi)$ | Albrecht & Skordis (2000) |

Table 2.1: Some scalar field potentials usually studied in dark energy models.

Rather than constructing models on the basis of cosmologically intersting dynamical properties, one may takes the complementary route of considering which models would appear most sensible from a particle physics point of view. An

accectable particle physics model would be one in which the scalar mass was naturally small. This requirement is met by Pseudo-Nambu-Goldston bosons (Frieman & Jaffe (1992), cf. Table 2.1), which arise in models with approximate global symmetries of the form $\phi \rightarrow \phi + const.$, and the potential takes a sinusoidal form. As a consequence, there is no easily characterised tracking or attractor behaviour.

Another model considered in literature is the $k$-essence idea (Armendariz-Picon et al. 2000), which does not put the field in a shallow potential, but rather modifies the form of the kinetic energy. If the Lagrangian is of the form $L = f(\phi)g(X)$, where $X$ is the conventional kinetic term, for certain choices of the function $f(\phi)$ and $g(X)$, the $k$-essence field naturally tracks the evolution of the total radiation energy density during the radiation era, but switches to being almost constant once matter begins to dominate.

We can deduce that a wide variety of possible behaviour should be taken seriously, with data providing the last guidance. Not ultimate, the possible interactions of the dark energy field with other form of energy.

## 2.3 Interactions

Provided that we don't know much about the properties of dark energy, there is no reason to exclude a priori the interaction that this new component can have with the other forms of energy. Actually, unless some symmetry doesn't prevent it we expect the scalar field to act on the other components. A way to describe this new physics is to modify the conservation equation of the single stress-energy tensors, coupling the equations, for example, of matter and dark energy. The most simple form of coupling is the linear one. Such a coupling can be obtained from the conformal transformation of a Brans-Dicke gravity (see e.g. Amendola (1999)), a generalised model of general relativity in which a term $\phi R$ (where $R$ is the Ricci scalar) arises. In a wide class of Brans-Dicke model after a conformal transformation of the metric one can obtain a linear coupling between dark energy and matter. It has also been considered several times in

literature, starting from Wetterich (1995, 1988) and Wands et al. (1993). It has been discussed in the context of dark energy models in Amendola (1999, 2000) and in Holden & Wands (2000), Chimento et al. (2000), Billyard & Coley (2000), Chiba (2001), Albrecht et al. (2002), Esposito-Farèse & Polarski (2001). In its conformally related Brans-Dicke form has been studied by Uzan (1999), Chiba (1999), Chen & Kamionkowski (1999), Baccigalupi et al. (2000), Sen & Sen (2001). Theoretical motivations in superstring models and in brane cosmology have been proposed in Gasperini et al. (2002) and Pietroni (2003), Brax et al. (2003).

Let's consider the two components (matter and dark energy), described by their stress-energy tensors $T_{\mu\nu(m)}$ and $T_{\mu\nu(\phi)}$, respectevely. General covariance requires the conservation of their sum, so that it is possible to consider an interaction between dark energy and matter such that

$$T^{\mu}_{\nu(\phi);\mu} = CT_{(m)}\partial_\nu\phi \tag{2.8}$$

$$T^{\mu}_{\nu(m);\nu} = -CT_{(m)}\partial_\nu\phi. \tag{2.9}$$

In the conformal metric (2.1) the scalar field and matter conservation equations, Eq. (1.6) and Eq. (2.6) respectevely, are modified in a such a way that

$$\ddot{\phi} + 2H\dot{\phi} + a^2V'(\phi) = C\rho_m a^2 \tag{2.10}$$

$$\dot{\rho_m} + 3H\rho_m = -C\rho_m\dot{\phi}. \tag{2.11}$$

The dimensionless coupling

$$\beta^2 = \frac{3C^2}{16\pi G} \tag{2.12}$$

can be seen as the ratio of the dark energy-matter interaction with respect to gravity (Damour & Nordtvedt 1993; Wetterich 1995). On the other hand, the Friedmann equation (1.4) can be written as

$$H^2 = \frac{8\pi G}{3}\Big(\frac{\rho_{m0}}{a}e^{(-C\phi)} + \frac{\rho_{\gamma 0}}{a^2} + \frac{1}{2}\dot{\phi}^2 + Va^2\Big), \tag{2.13}$$

where $\rho_{m0} = \rho_m(\tau_0)$ and $\rho_{\gamma 0} = \rho_\gamma(\tau_0)$. The specific coupling (2.8) is only one of the possible forms. Non-linear coupling as $CT_{(m)}F(\phi)\partial_\mu\phi$ or more complicate

functions are also possible. Also, as we will see in Chapter 4, one can think of different couplings to different matter species, for instance coupling the scalar field only to dark matter and not to baryons, as first proposed by Damour (1990) and Casas et al. (1992). Notice that the coupling to radiation vanishes, since $T_{(\gamma)} = 0$, and the conservation equation for its energy density is

$$\dot{\rho_\gamma} + 4H\rho_\gamma = 0. \tag{2.14}$$

The system (2.10 - 2.11) includes several qualitatively different behaviours, already discussed in Amendola (2000), Tocchini-Valentini & Amendola (2002). However, for the range of values that are of cosmological interest, the new and most important feature emerging from coupled dark energy is a phase called $\phi$MDE. The $\phi$MDE changes the expansion of the Universe and the evolution of the matter perturbations. Immediately after equivalence, the system enters a matter dominated epoch with a non-negligible $\phi$ contribution (cf. Fig. 2.1, in a case where dark energy couples only to dark matter), in which the dark energy potential density is negligible while the kinetic energy density parameter $\Omega_{k\phi}$ of the scalar field gives a constant contribution to the total density. The dynamics of the system is insensitive to the sign of $\beta$, since the $\phi$MDE and the tracking phases do not depend on ot. As will be shown in the following (from Chapter 4 on), the existence of such an epoch is crucial for the constraints that we will be able to put on the coupling. Along the $\phi$MDE the scale factor expands slower than a pure MDE, perturbations grow faster and the matter particle mass varies. We will analyse in detail different classes of models, but the important fact is that the existence of such a phase is independent of the potential, although it has to be verified for each potential whether it is a saddle point of the system or not.

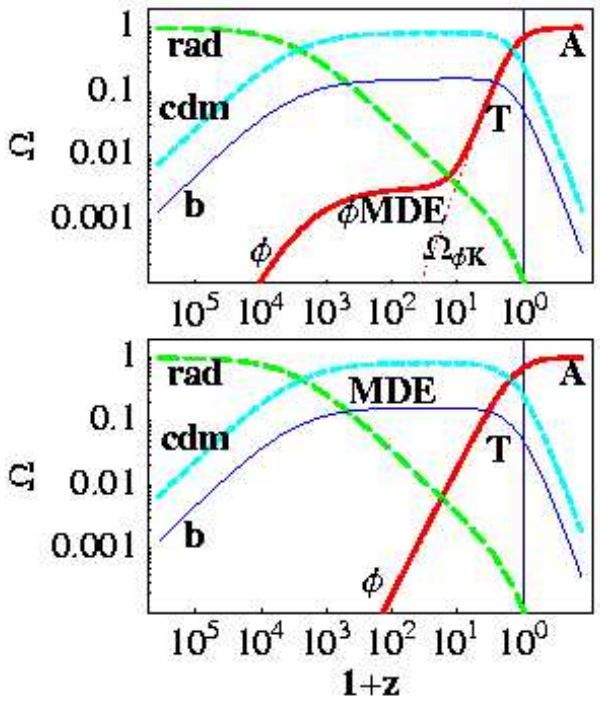


Figure 2.1: The evolution of energy density parameters with redshift. Radiation, dark matter, baryons and the scalar field are represented by green, light blue, blue and red lines. The dotted red line is the potential term in the dark energy density parameter. Bottom panel: uncoupled case. Upper panel: the same model, but with the coupling between dark energy and dark matter. The new $\phi$MDE clearly emerges.

# Chapter 3

# What can surveys tell about dark energy?

In this Chapter we discuss the constraints that future photometric and spectroscopic redshift surveys can put on dark energy through the baryon oscillations of power spectrum. Here the dark energy is modeled either with a perfect fluid (see Sec.1.4) or a scalar field (see Sec. 2.1) and take into account the information contained in the linear growth of density perturbations.
Since the characterization of dark energy has been to date based almost uniquely on background tests at rather low redshifts like SNe Ia experiments, or very large redshifts like the CMB measurements, if we aim at making real progress it is necessary to cross this informations with probes at intermediate $z$ and with other

observables such as the linear growth function. In this Chapter we will show how *future* observations of LSS at $z$ up to 3 can set interesting limits on models of dark energy. The method we use is based on recent proposals (Linder 2003; Blake & Glazebrook 2003; Seo & Eisenstein 2003) to exploit the baryon oscillations in the power spectrum as a standard ruler calibrated through CMB acoustic peaks. Most of the work presented in this Chapter has been published in Amendola, Quercellini, & Giallongo (2004).

## 3.1 Fisher Matrix Method

The method used to make predictions from future surveys is the Fisher matrix, an approximation to the likelihood function that provides under some conditions the minimal errors that a given experiment may attain (Eisenstein, Hu, & Tegmark 1999).

Our starting point is a cosmological model that predicts the evolution of the Hubble parameter and the growth of linear perturbations $G(z)$. From $H(z)$ we can estimate the angular diameter distance

$$d_A(z) = (1+z)^{-1} \int_0^z \frac{dz'}{H(z')}. \tag{3.1}$$

We choose a reference cosmology, denoted by a subscript $r$, for instance a model with a cosmological constant ($\Lambda$CDM), and calculate the matter power spectrum in real space at $z = 0$, $P_{0r(k_r)}$ (where $k_r$ is the wave number modulus). Then the predicted observable galaxy power spectrum in a different cosmology at $z$ in redshift space is

$$P_{obs}(z, k_r, \mu_r) = P_s(z) + \frac{d_{Ar}^2(z) H(z) G^2(z)}{d_A^2(z) H_r(z)} \frac{\Omega_m^{1.2}(z)}{\beta^2(z)} (1 + \beta\mu^2)^2 P_{0r}(k), \tag{3.2}$$

where $\mu$ is the direction cosine of the wave number. Several comments will clarify the meaning of this equation.

$P_s(z)$ is a scale indipendent offset due to incomplete removal of shot-noise. The factor $(d_A^2/H)/(d_{Ar}^2/H_r)$ takes into account the difference in comoving volum

between the two cosmologies. The factor $(1+\beta\mu^2)^2$ is the redshift distortion. $G(z)$ is the growth factor of the linear matter density contrast $\delta_m$, i.e.

$$G(z) = \frac{\delta_m(z)}{\delta_0}, \tag{3.3}$$

where $\delta_0$ is the present day density contrast (and therefore $G(z)$ is normalised to unity today).

The evolution of the matter density parameter also depends on the cosmology in a way such as, in a ΛCDM, it is given by

$$\Omega_m(z) = \frac{\Omega_{m0}(1+z)^3}{\Omega_{m0}(1+z)^3 + 1 - \Omega_{m0}}, \tag{3.4}$$

and it is therefore parametrised by the present density parameter $\Omega_{m0}$. The bias parameter $\beta(z) = \Omega_m^{0.6}(z)/b(z)$, assumed scale-invariant, is evaluated for the reference cosmology using the formula

$$\sigma_{8,g} = \beta(z)^{-1}\Omega_m^{0.6}(z)\sigma_{8,m}\sqrt{1 + \frac{2\beta(z)}{3} + \frac{\beta^2(z)}{5}}, \tag{3.5}$$

where $\sigma_8$ is the variance in spherical cells of 8 Mpc/$h$ for galaxies (subscript $g$) or matter (subscript $m$). Notice that the variance is calculated using the power spectrum averaged over $\mu$. Finally, we can include a redshift error by rescaling the power spectrum

$$P = P_{obs}e^{(-k^2\mu^2\sigma_r^2)}, \tag{3.6}$$

where $\sigma_r = \delta z/H(z)$ is the absolute error in distance and $\delta z$ the absolute error in redshift.

The observed power spectrum in a given redshift bin $z_0$ depends therefore on a number of parameters, denoted collectively $p_i$, such as $\Omega_{m0}$, $G(z_0)$, $H(z_0)$ ecc., as detailed in Table 3.1. The redshift dependent parameters ($P_s$, $H$, $G$, $d_A$, $\beta$) are assumed to be approximately constant in each redshift bin. Then we calculate, numerically or analitically, the derivatives of the power spectrum

$$\Big(\frac{\partial \ln P}{\partial p_i}\Big)_{ref}. \tag{3.7}$$

Finally, the Fisher matrix is

$$F_{ij} = \frac{1}{8\pi^2}\int_{-1}^{1}\int_{k_{min}}^{k_{max}} \Big(\frac{\partial \ln P}{\partial p_i}\frac{\partial \ln P}{\partial p_j}\Big)_{ref} V_{eff}(k,\mu)k^2 dk d\mu, \tag{3.8}$$

where the effective volume $V_{eff}$ is

$$V_{eff}(k,\mu) = \Big(\frac{nP(k,\mu)}{nP(k,\mu)+1}\Big)^2 V_{survey}, \tag{3.9}$$

$n$ being the number density of galaxies and $V_{survey}$ the volume of the survey.
In addition to that, we decided to use also the CMB Fisher matrix (Seljak (1996), Eisenstein, Hu, & Tegmark (1999))

$$F_{ij,CMB} = \sum_l \sum_{X,Y} \frac{\partial C_{X,l}}{p_i} (Cov_l)^{-1}_{XY} \frac{\partial C_{Y,l}}{p_j}, \tag{3.10}$$

where $C_{X,l}$ is the multiple spectrum of the component $X$ ($X = T, E, B, C$ denote the temperature $T$, $E$ and $B$ polarization, and the cross-correlation $TE$ respectevely), with covariance matrix $(Cov_l)_{XY}$. In this analysis we considered a future experiment similar to the Planck satellite. The spectra has been obtained numerically with the Boltzmann code CMBFAST (Seljak & Zaldarriaga 1997).
Once we have the Fisher matrices for all data we sum to obtain the total combined matrix

$$F_{ij} = F_{ij,CMB} + \sum F_{ij,survey}. \tag{3.11}$$

Then, the inverse of the diagonal elements of the (3.11) gives the predicted errors on the parameters.
As a reference, we used the ΛCDM with $\Omega_{m0} = 0.35$, $h = 0.65$, $\omega_b = 0.021$, $\tau = 0.05$, $n_s = 1$, $T/S = 0$, $P_s = 0$ (for the independent parameters that we included in the Fisher matrix see Table 3.1).

## 3.2 Surveys and data

One of the main aim of this work is to show how it is possible to build, using deep and wide multicolour surveys, a photometric redshift sample of galaxies suitable for the analysis of the galaxy power spectrum as a function of redshift. First of all spectroscopic surveys are clearly favourite with respect to photometric ones because any uncertainty $> 1\%$ in the photometric redshifts increases the uncertainty on $H(z)$ at $z > 0.5$ to $> 10\%$ for surveys covering areas of 100-1000 deg$^2$.

| **Parameters** | |
|---|---|
| $P_0(k)$ | |
| $\omega_m \equiv \Omega_{m0}h^2$ | Reduced total matter |
| $\omega_b \equiv \Omega_{b0}h^2$ | Reduced baryon density |
| $\tau$ | Optical thickness |
| $n_s$ | Primordial fluctuation slope |
| $\Omega_{m0}$ | Total matter density |
| **For each survey at $z$** | |
| $P_s$ | Shot noise |
| $d_A$ | Angular diameter distance |
| $H$ | Hubble parameter |
| $G$ | Growth function |
| $\beta$ | Bias |
| **Additional CMB parameters** | |
| $D_A$ | Decoupling angular diameter distance |
| $T/S$ | Tensor-to-scalar ratio |
| $A_s$ | $C_l$ normalization |

Table 3.1: Parameters on which the observed power spectrum depends.

Second, the relatively bright magnitude limit needed to keep a high completeness level in the spectroscopic follow up implies a low number density of sources per unit area. Large survey areas are hence neede to garantee adequate total number of objects. Here we show that it is possible to envisage a photometric survey with adequate depth and limited area of the sky at $z = 0.5 - 1$ and $z = 2.7 - 3.5$ that can provide constraints on the redshift dependence of the dark energy equation of state which are competitive with those obtained from SNe Ia and CMB in the foreseeable future.

To measure the redshift evolution of $H(z)$ and of the angular diameter it is important to analyse the power spectrum in a wide redshift interval with specific sampling at $z = 0.5 - 1$, and especially at $z = 3$ where the linear regime of glaxy clustering extends to smaller physical scales, allowing the analyses of acoustic oscillations to higher frequencies in the range $0.1 < k < 0.5h$ Mpc$^{-1}$. What is important is the estimate of the characteristic wavelength of the acoustic oscillations $k_a = 2\pi/s$ which is connected with sound horizon $s$ at recombination. For our reference $\Lambda$CDM model $k_a \simeq 0.06h$ Mpc$^{-1}$. It is crucial to emphasize that local surveys could probe only the first peak at $k \simeq 0.075h$ Mpc$^{-1}$. Thus, an appropriate comparison with the CMB power spectrum requires higer frequencies and consequentely high redshift surveys, in particular at $z = 3$.

Indeed, large scale galaxy surveys at $z \geq 3$ could in principle be built in a straightforward way, using the standard multicolor dropout technique which exploits the detection in the galaxy spectra of the UV Lyman absorption due to the local interstellar medium in the galaxy and in the intergalactic medium present along the line of sight. At $z = 2.5-3.5$ the Lyman series absorption progressively enters the UV filter causing a reddening in the U-R galaxy color. At $z = 3.5 - 4.5$ instead the droptout shifts in the blue causing a reddening in the B-R galaxy color, and so on. Spectroscopic confirmation has provided a relatively high success rate of 75% (Steidel 1998, 1996), although in practice it is difficult to obtain a high completeness level in the magnitude interval R$= 24 - 25.5$, which is the present limit for systematic spectroscopic follow up at $10m$ class telescopes. Surveys at $z \sim 3$ down to a magnitude limit of R$\sim 25$ are the best compromise for the study

of large scale structures at high redshift provided that efficient wide field imagers with high UV efficiency are used. The Large Binocular Camera in construction at the prime focus of the Large Binocular Telescope is an ideal imager to this aim (see Pedichini et al. (2003)). At $z = 3$ a photometric survey down to the

| **Surveys** | | |
|---|---|---|
| $z$ | $V_s(\mathrm{Gpc}^3)$ | n |
| $0.5 - 0.7$ | 0.030 | $6.9 \times 10^{-2}$ |
| $0.7 - 0.9$ | 0.040 | $4.2 \times 10^{-2}$ |
| $0.9 - 1.1$ | 0.050 | $3.1 \times 10^{-2}$ |
| $1.1 - 1.3$ | 0.0570 | $2.4 \times 10^{-2}$ |
| $2.7 - 3.5$ | 0.27 | $2 \times 10^{-3}$ |

Table 3.2: Densities and volumes for the basic surveys of area 100 deg$^2$.

magnitude limit of R$\leq$ 25 gives a total number density in the range $z = 2.7 - 3.5$ of $n \sim 2 \times 10^{-3} h^3$ Mpc$^{-3}$, after integration over the UV Schechter luminosity function of Poli et al. (2001). At $z = 1$ the same photometric survey at R$\leq$ 25 in the range $z = 0.5 - 1$ would give a total number density of $n \sim 4.5 \times 10^{-2} h^3$ Mpc$^{-3}$, as obtained from the blue luminosity function of Poli et al. (2001). For sake of comparison we adopt the same reshift binning at $z \sim 1$ as Seo & Eisenstein.

Detailed densities and volumes for the basic surveys of area 100 deg$^2$ are shown in Table 3.2, in the same redshift intervals used by Seo & Eseinstein. As we will see, we derived results also for larger surveys, corresponding to areas of 200 deg$^2$ and 1000 deg$^2$ respectevely, and with sparser surveys at $z \simeq 1$, adopting a density 10 times smaller as that quoted in Table 3.2. The absolute error in redshift is taken to be either zero (spectroscopic surveys) or $\delta z = 0.02$ and $\delta z = 0.04$ (photometric surveys). Finally we also consider a hybrid survey, i.e. a photometric survey with $\delta z = 0.02$ at $z \simeq 1$ combined with a spectroscopic one at $z \simeq 3$. Indeed a spectroscopic survey at $z \simeq 3$ appears more efficient.

To this surveys we add data from SDSS (Eisenstein et al. 2001), that are con-

sidered always spectroscopic. To the redshift surveys we add also CMB data, adopting the Planck-like specifications of Seo & Eseinstein. Finally, we evaluate SNe Ia constraints from surveys that produce approximatively near future catalogs from ground-based observations: 400 SNe Ia distributed uniformly in redshift between $z = 0$ and $z = 1.5$, with magnitude errors $\Delta m = 0.25$ and the same stretch factor correction as in the sample of Perlmutter et al 99. We marginalise over the $H$-dependent magnitude and the stretch factor. These SNe likelihood functions are therefore completely indipendent of the Hubble constant determination. Notice that the SNe Ia likelihood contours are estimated through the full likelihood function rather than with a Fisher matrix to facilitate the comparison with current estimates.

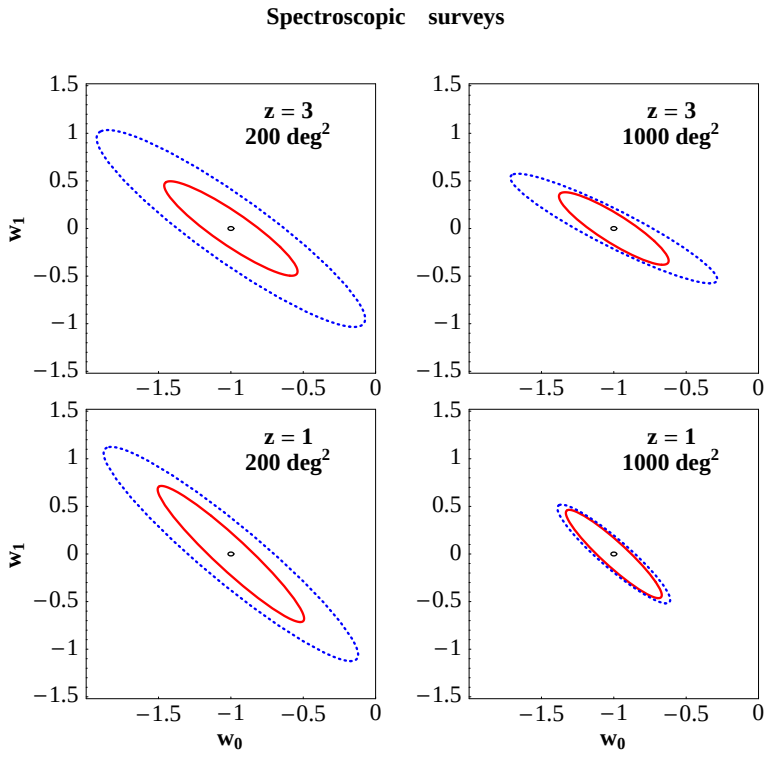


Figure 3.1: Effect of the growth function for spectroscopic surveys: confidence regions marginalizing over $G$ (dotted curves) and using the information in $G$ (full curves). The plots are for the surveys at $z = 3$ alone (upper panels) and for $z = 1$ alone (lower panels). Lines referring to $G$-marginalization are blue, those referring to the inclusion of $G$ are in red.

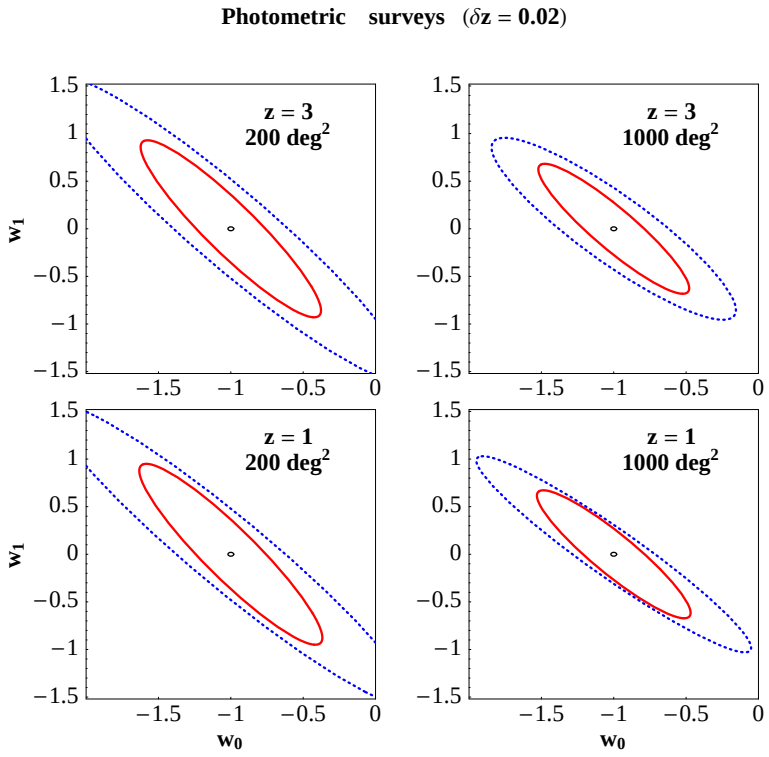


Figure 3.2: Effect of the growth function for photometric surveys: confidence regions marginalizing over $G$ (dotted curves) and including $G$ (full curves). The plots are for the survey at $z = 3$ alone (upper panels) and $z = 1$ alone (lower panels).

## 3.3 A simple extended form of dark energy [II]

We begin the analysis with a simple model of dark energy based on a perfect fluid representation, as reviewed in Sec. 1.4. In literature, many parametrization of the equation of state parameter as a function of redshift have been considered (Corasaniti et al. 2003); for our purpose, since we are dealing with low redshift data, a simple taylor expansion of $w(z)$ is sufficient:

$$w(z) = w_0 + w_1 z. \tag{3.12}$$

Such a perfect fluid model, as we already remarked, can be only a phenomenological description of the background dynamics. Beside the obvious fact that

$w$ diverges at high $z$, the problem is that a meaningful derivation of the fluctuation equations requires as additional prescription the dependence of $w$ on the perturbed dark energy density. Moreover, if one assumes for simplicity that $\delta w/\delta\rho = 0$, then the dark energy becomes highly unstable at small scales since the sound speed $c_s \equiv \sqrt{\delta p/\delta\rho}$ is immaginary for $w(z) < 0$. We can discuss therefore the growth function (5.23) only in the ΛCDM limit $w_0 = -1$, $w_1 = 0$. In this limit a useful approximation is

$$\frac{d\ln G}{d\ln a} = \Omega_m(a)^\gamma, \tag{3.13}$$

with $\gamma \simeq 0.6$. Since $G$ can be calculated only in the ΛCDM limit, we assume that $G$ does not depend on $w_0$ and $w_1$: this is a conservative statement, since any dependence would further restrict the area of the confidence region of parameters. Moreover, we found that, naively extending the validity of (3.13) to other values of $w_0$ and $w_1$ (i.e. assuming dark energy to be completely homogeneous), the results do not change sensitively. Therefore $G$ will be assumed in this Section to depend only on $\Omega_{m0}$. The derivative with respect to $\Omega_{m0}$ is

$$\frac{d\ln G}{d\Omega_{m0}} = \gamma\int \Omega_m(a)^\gamma \frac{d\ln\Omega_m}{d\Omega_{m0}}da = -\gamma\int \frac{e^{(3a)}\Omega_m(a)^\gamma}{[\exp(3a)(\Omega_{m0}-1)-\Omega_{m0}]\Omega_{m0}}da. \tag{3.14}$$

Once we have the total Fisher matrix, we invert it and extract a submatrix $F_{sub,ij}$ containing all the parameters $p_i$ that depend on the cosmological parameters $\omega_m$, $\Omega_{m0}$, $w_0$, $w_1$. Beside $\omega_m$ and $\Omega_{m0}$ these are, for each survey, $\ln d_A$, $\ln H$ and $\ln G$, plus $\ln d_A$ of the CMB. As we said, the diagonal elements of $F^{-1}_{sub,ij}$ give the square of the errors on the relative variables. In Amendola et al. (2004) the relative errors on $H$, $d_A$ and $G$ are derived. The final projected dark energy Fisher matrix is

$$F_{de,mn} = \Big(\frac{\partial p_i}{\partial d_m}\Big)F_{sub,ij}\Big(\frac{\partial p_j}{\partial d_n}\Big), \tag{3.15}$$

where $d_n = (\Omega_{m0}h^2, \Omega_{m0}, w_0, w_1)$. Then we again invert and take a submatrix whose eigenvalues and eigenvectors define the confidence ellipsoid on the plane $w_0$ and $w_1$, i.e. predictions on the dark energy equation of state parameters.

The results for the various surveys and for different redshift errors are in Figs. 3.1-3.4. In Fig. 3.1 and 3.2 we show the effect of marginalizing over $G$ versus fixing

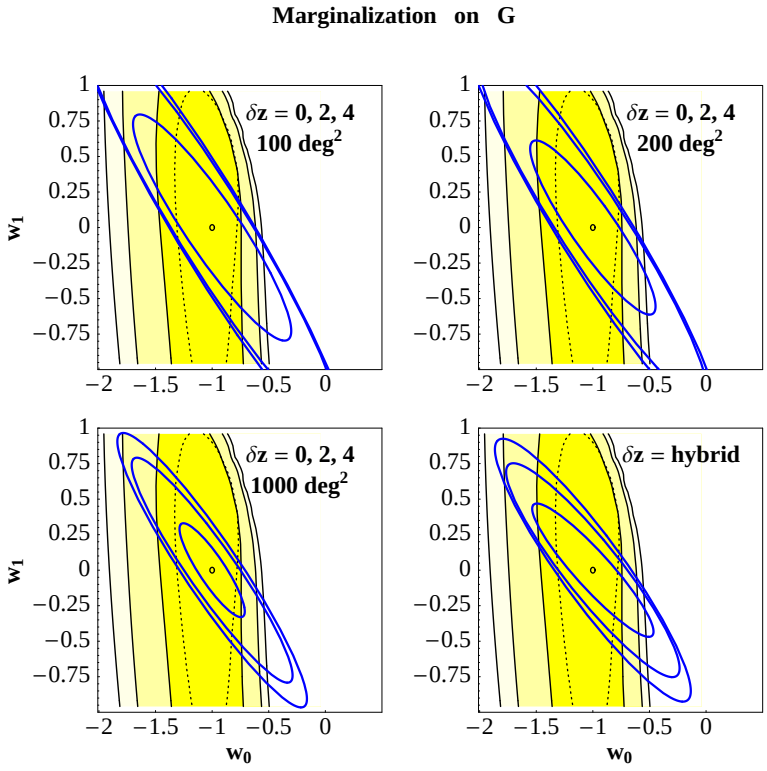


Figure 3.3: Confidence ellipsis for the combined data CMB, SDSS, surveys at $z \sim 1, 3$, for three redshift errors, $0, 0.02$ and $0.04$, inside to outside. Here and in all subsequent plots the redshift errors are indicated as $100 \times \delta z$. The central dot is the reference cosmology. The bottom right panel refers to the hybrid survey: here the contours are for surveys of $1000, 200$ and $100$ deg$^2$, inside to outside. The shaded areas are the confidence regions for 400 simulated SNe Ia distributed according to the reference cosmology up to $z = 1.5$, at 68%, 95% and 99%, inside to outside, marginalizing over $H_0$ (uniform prior) and over $\Omega_{m0}$ with a gaussian centered on the reference value and variance 0.1. The dotted contour (at 68% C.L.) assumes instead a 10% Gaussian error on $H_0$ for the SNe Ia data.

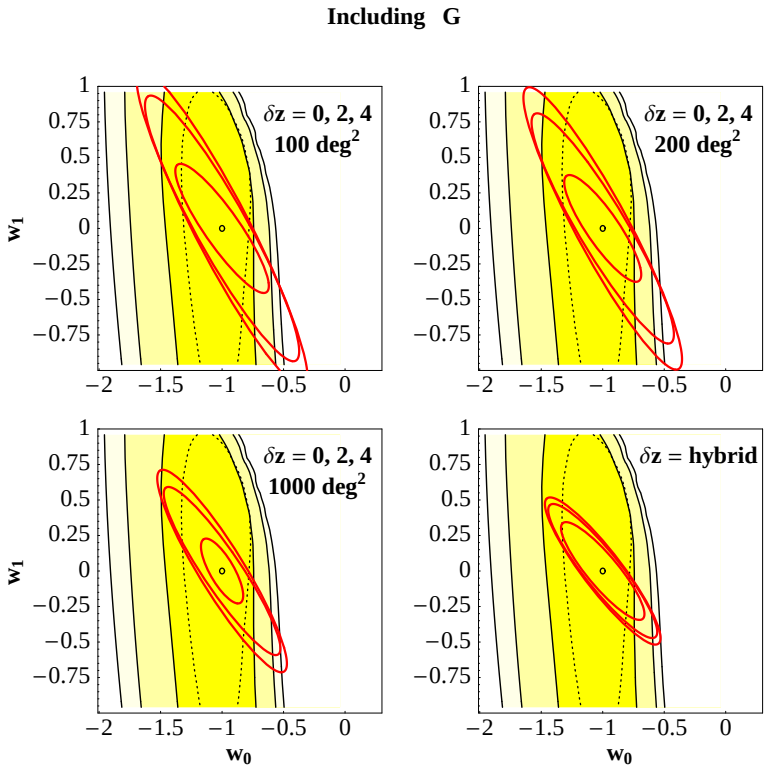


Figure 3.4: As in Fig. 3.3 but including the dependence of the growth factor and the dark energy parameters.

it for the four surveys at $z \simeq 1$ and the survey at $z = 3$, always including CMB and SDSS. At $z = 3$, we could say that a survey of 200 deg$^2$ that includes the information in $G$ is roughly equivalent in terms of constraining power to a survey of 1000 deg$^2$ with $G$ marginalization. The effect at $z \simeq 1$ is smaller, because the (3.14) is smaller at low $z$.

In Fig. 3.3 we show the results for all redshift bins marginalising over $G$, while in Fig. 3.4 we include $G$. In the same plots we show the contours of the likelihood for simulated SNe Ia data. It is interesting to notice that the supernovae constrain $w_0$ to a much higher precision than $w_1$. Multiplying the baryon oscillation contours with the SNe Ia limits one sees that the advantage of spectroscopy reduces considerably, at least below 200 deg$^2$, almost regardless of $\delta z$, as can be seen in Fig. 3.5.

We compare our baryon oscillation forecasts also with the *present* SNe Ia data.

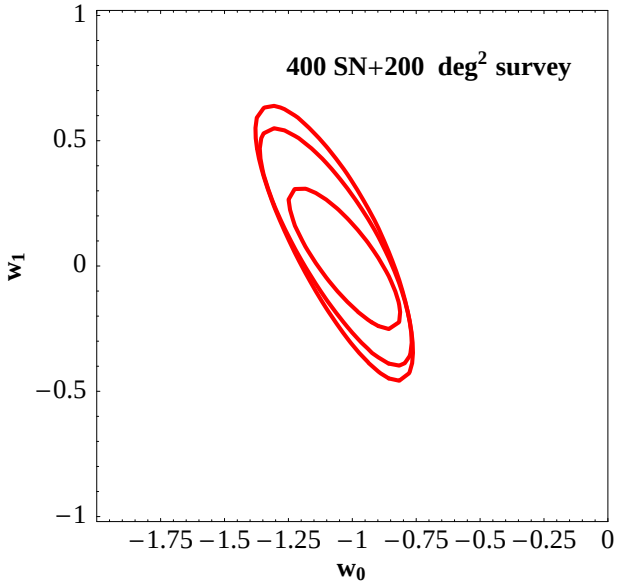


Figure 3.5: Contours at 68% of the combined likelihood of supernovae and surveys of 200 deg$^2$ with redshift errors $\delta z = 0, 0.02, 0.04$, inside to outside (including $G$).

In Fig. 3.6 we show the constraints from the current set of supernovae of Riess et al. (2004) (*gold* sample), along with the constraints for a 200 deg$^2$ survey with reference cosmology centered on the Riess et al. (2004) best fit, $w_0 \simeq -1.3$,

$w_1 \simeq 1.5$ and $\Omega_{m0} = 0.27$. This plot shows that the size and orientation of the Fisher contour regions depends in a significant way on the underlying reference cosmology, as already remarked in Seo & Eisenstein (2003). It also reveals that, in cases as this, the spectroscopic surveys maintain their advantage even using the SNe Ia information.

## 3.4 Surveys with a scalar field

Since, as already remarked, this perfect fluid model has no theoretical motivation and is incomplete for its capability to describe just the background dynamics at low redshift, we now adopt one of the first and simplest model among them reported in Table 2.1, the inverse power law potential (Ratra & Peebles (1988), Steinhardt et al. (1999))

$$V = A\phi^{-n}. \tag{3.16}$$

In this Chapter we don't take into account a possible extra-interaction. Hence the cosmological equations for this model happen to be Eq. (2.6) and the Friedmann equation

$$H^2 = H_0^2\Omega_{m0}a^{-3} + \frac{8\pi G}{3}\Big(\frac{\dot{\phi}^2}{2a^2} + V\Big). \tag{3.17}$$

In Steinhardt et al. (1999) it has been shown that such a model possesses a tracking solution, defined as a trajectory on which many initial conditions converge, as shown in Fig. 3.7. Once a solution reaches this trajectory its property are determined solely by the slope $n$ and the present value $\Omega_{m0}$. Since the variation of the equation of state parameter $w_\phi$ is relatively small, to a first approximation the inverse power law model for $n \ll 1$ resembles a perfect fluid with

$$w_\phi \simeq w_0 = -\frac{2}{(2+n)} \tag{3.18}$$

and $w_1 \simeq 0$. Further, we find that for the growth function the same approximation (3.13) adopted for ΛCDM remains valid, with deviation from the numerical result less than 0.1% in the range $z = 0 - 3$. For all practical purposes the

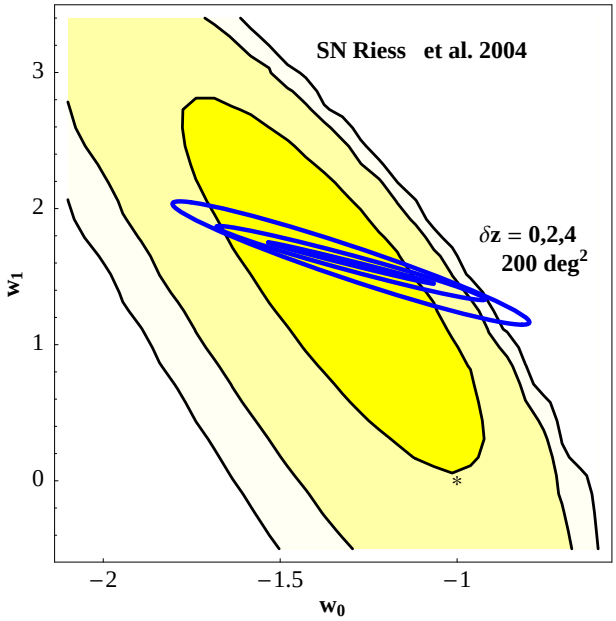


Figure 3.6: Here we compare the confidence regions of 200 deg$^2$ surveys with redshift errors of $0.0.02, 0.04$ (marginalized over $G$) to the recent SNe Ia data of Riess et al. (2004) assuming $\Omega_{m0} = 0.27 \pm 0.04$ (Gaussian errors). The SNe contours are $68, 90$ and $95\%$. The star marks the $\Lambda$CDM model.

dependence of $\gamma$ on $n$ can be neglected and we put $\gamma = 0.6$ in the whole interesting range. As in the previous Section, we project now the Fisher matrix in the subspace $d_n = (\Omega_{m0}h^2, \Omega_{m0}, n)$. The results are shown in Fig. 3.8, where the reference cosmology has $n = 0.05$, practically indistinguishable from $\Lambda$CDM, and are projected on the plane $\Omega_{m0}, n$. As expected, the SNe Ia contours are elongated towards the contours of $HD$ (see the contour plots in Fig. 3.9). The contours of the Fisher matrix are instead slanted toward the direction of the iso-G lines: this shows that it is the information in $G$ that drives the results, and optimises the complementarity between SNe Ia and LSS. The tracking scalar field model

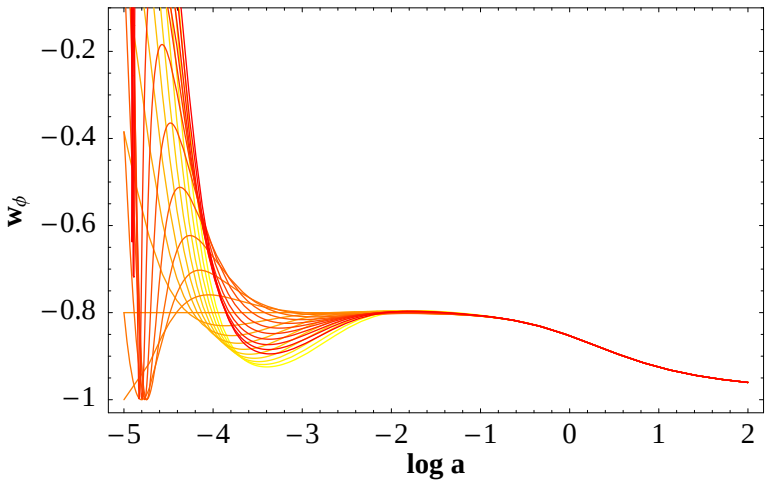


Figure 3.7: Equation of state of the scalar field model for several different initial conditions.

has been tested toward SNIa and CMB. We analysed the Riess 2004 data with the inverse power law potential and found the constraint $n < 0.9$ at 68% C.L. ($n < 0.5$ assuming $\Omega_{m0} = 0.3 \pm 0.05$). On the other hand, as we will see in the next Chapter, WMAP data allow for $n < 0.94$ (or $n < 0.74$ including the HST prior on the Hubble constant) at 68% (Amendola & Quercellini 2003). From Fig. 3.8 we see that the baryon oscillations for a scalar field model can constrain $\Omega_{m0}$ to better than 3%, and the slope $n$ to $n < 0.15$ and $n < 0.53$ depending on the survey strategy. For a spectroscopic survey the limit is $n < 0.26$ and for a survey with errorbars $\delta z = 0.02$ is $n < 0.40$. In all cases this is quite better than

the current and near-term SNe Ia and CMB constraint. Once again, most of

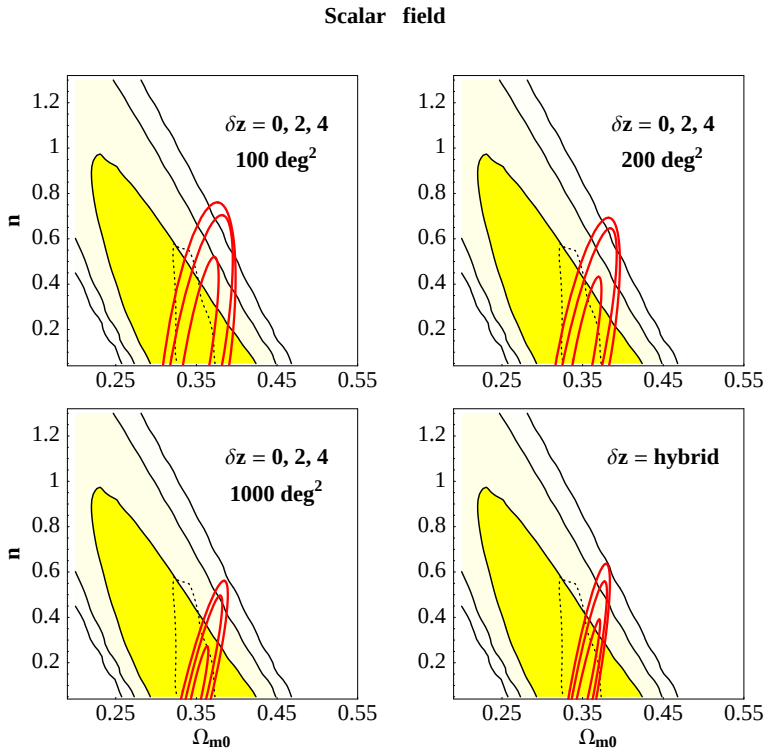


Figure 3.8: As in Fig. 3.3 but for the scalar field model.

the advantage of spectroscopic measures vanishes if one takes into account the SNe Ia contours (see Fig. 3.10). Here again we perform the comparison with the Riess et al. (2004) *gold* sample of supernovae (Fig. 3.11). It can be seen that the present SNe Ia data already cut most of the vertical elongation of the contours for the photometric surveys, leading to constraints on $n$ which are similar to spectroscopic surveys. The spectroscopic errors on $\Omega_{m0}$ remain however competitive.

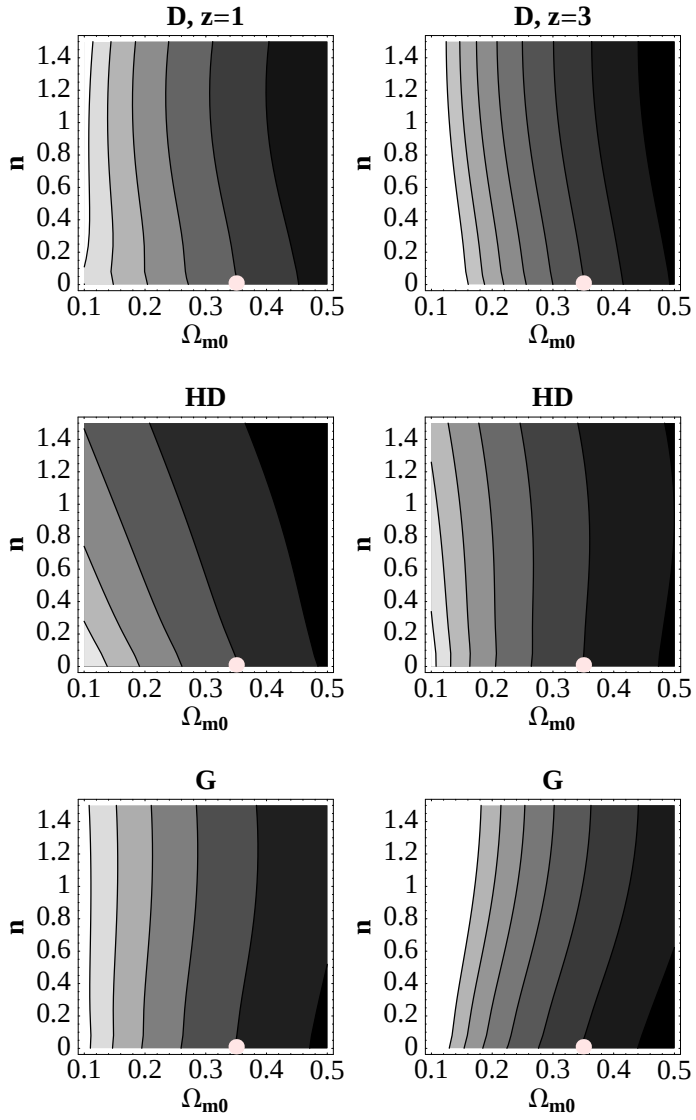


Figure 3.9: The plot displays the contours of $D$, $HD$, $G$ at $z = 1$ (left column) and $z = 3$ (right column). Each function is normalized by the value at the reference cosmology, marked by the white dot. The contours are for steps of 0.05, increasing from black to white.

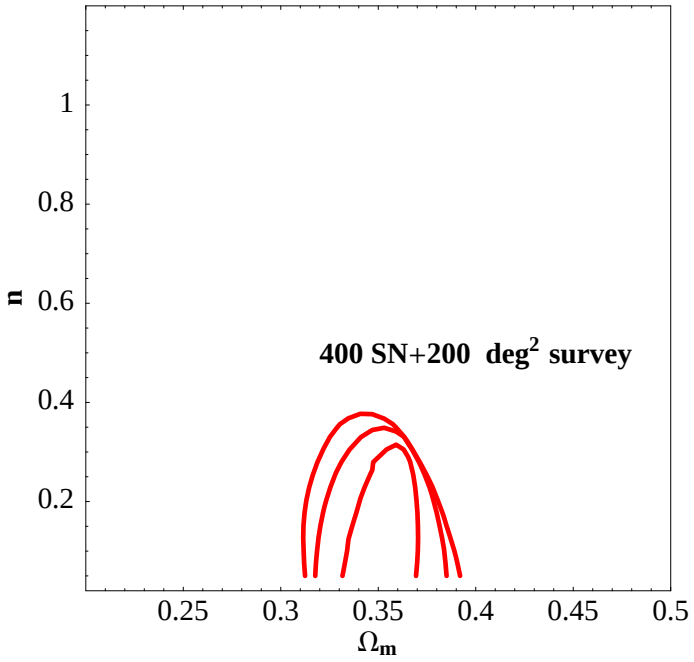


Figure 3.10: Scalar field: contours at 68% of the combined likelihood of supernovae and surveys of 200 deg$^2$ with redshift errors $\delta z = 0, 0.02, 0.04$, inside to outside (including $G$).

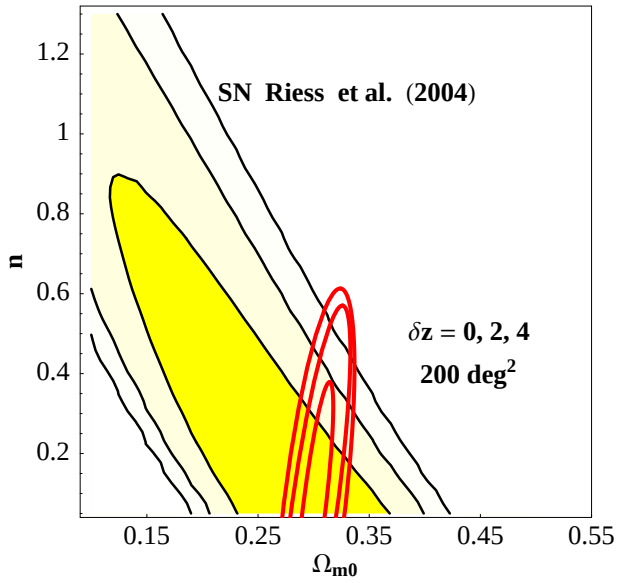


Figure 3.11: Here we compare the confidence regions of 200 deg$^2$ surveys with redshift errors of $0.0.02, 0.04$ with the confidence regions for the scalar field model with the recent SNe Ia data of Riess et al. (2004). For this plot the reference cosmology in the Fisher matrix coincides with the best fit to the SNe ($\Omega_{m0} = 0.3$, $n = 0$). The SNe contours are $68, 90$ and $95\%$.

# Chapter 4

# Dark energy on Cosmic Microwave Background

The WMAP data mark an important step: they represent the first publicly available multi-band high-resolution full-sky survey of the cosmic microwave sky. This experiment is likely to remain the highest quality CMB temperature anisotropy survey until the launch of the Planck satellite, not earlier than 2007. In this Chapter we address the question of what the first year of WMAP data can tell us about the properties of dark energy. Two classes of models will be considered, which are at the same time general (in the sense of covering most modelizations) and simple. First we consider dark energy as a scalar field with inverse power law potential, as in Chapter 3. In the second class we include models of dark

energy with an interaction between dark energy and dark matter (see Sec. 2.3). Since observations require the baryons to be decoupled from dark energy (or coupled much more weakly than dark matter), the search for a dark-dark coupling is also a test of the equivalence principle. In fact, with this extra-coupling, dark energy effectively violates the equivalence principle, wich states the universality of gravity force for every form of energy, and it is remarkable that in order to constrain it, the only possible way must be cosmological, since it would escape laboratory experiments. Cosmological observation like the CMB are the unique way to observe such a phenomenon.
The material presented in this Chapter can be found in Amendola & Quercellini (2003) and Amendola et al. (2003).

## 4.1 Uncoupled dark energy

All the constraints for CMB presented in the literature on dark energy equation of state are necessarily somewhat model-dependent, since the fundamental quantity, namely the angular dianeter distance to last scattering (3.1), in general dependes on $w_\phi$ through two integrals over the cosmic evolution that do not allow to distinguish among different parameters along degeneracy curves. Although at low multiples the geometric degeneracy could in principle be broken by the integrated Sachs Wolf effect, the cosmic variance and the weakness of the effect make this possibility unrealistic in most cases. This is the reason why it is convenient to gather the possible models into classes.
The Ratra & Peebles potential (3.16) also recovers the exponential potentials for large values of $n$; in all the cases , the equation of state at the present is roughly constant and equal to (3.18), due to the tracking mechanism (cf. Fig. 3.7). This approximates also the cases in which the dark energy is a perfect fluid with constant $w_\phi$, since the angular size of the acoustic horizon depend on the equation of state only, and includes also the cases in which the $\Omega_\phi$-weighted average of a slowly varying function $\hat{w}_\phi(a)$ (see e.g. Doran et al.2001).
The WMAP team analysed their power spectrum including dark energy with a

constant equation of state (and no coupling). They found for the equation of state $w_\phi < -0.5$ with CMB alone and $w_\phi < -0.78$ including supernovae. Although dark energy with an inverse power law potential has an equation of state which is constant only near the present epoch, we will recover very similar results for this class of models, as expected.

## 4.2 The method

We compare the models to the combined power spectrum estimated by WMAP (Hinshaw et al. 2003). To derive the likelihood we adopt a version of the routine described in Verde et al. (2003), which takes into account all the relevant experimental properties (calibration, bin uncertainty, window functions, ecc.). Since the likelihood routine employs approximations that work only for spectra not too far from the data, we run it only for models whose $\chi^2$ is less than fou times the degree of freedom. We experimented with increasing the $\chi^2$ cut and found no important variations.

We also compare the data to the whole set of pre-WMAP data. To do this, we use the power spectrum provided by Wang et al. (2002), which is a compression of essentially all the available data up to mid-2002 in 25 $l$-bins, from $l = 2$ to $l = 1700$, complete of correlation matrix and window functions (calibration and beam uncertainty are included in the correlation matrix). The main entries in this compilation are COBE (Bennett et al. 1996), Boomerang (Netterfield et al. 2002), DASI (Halverson et al. 2002), Maxima (Lee et al. 2001), CBI (Pearson & Cosmic Background Imager Collaboration 2002), VSA (Scott et al. 2003). To this we add Archeops (Benoît et al. 2003) with its correlation matrix, window functions, beam and calibration uncertainties. For the pre-WMAP data we assume no reionization ($\tau = 0$) because this was the best fit before WMAP, and integrate out analytically the calibration, the beam uncertainties and the overall normalization.

Let us denote with $N_e$, $\sigma_e$, $\sigma_{w,e}$ the correlation matrix, the calibration uncertainty and the beam uncertainty, respectevely, of the $e$-th experiment, and with

$I_e = 1, 1, 1, ...$, a vector of dimensions equal to the number of bins in the $e$-th experiment. Moreover, let $C_{l,t'}$ be the theoretical CMB spectrum binned in the $l$-th bin with the experimental window function. Then one gets the remarkably simple likelihood function (see Amendola & Quercellini (2003) for details)

$$L = \exp\Big[ -\frac{1}{2}\Big(\gamma - \frac{\beta^2}{\alpha}\Big)\Big], \tag{4.1}$$

where

$$\alpha = \sum_e I_e^T M_e^{-1} I_e \tag{4.2}$$

$$\beta = \sum_e I_e^T M_e^{-1} (Z_t - Z_d) \tag{4.3}$$

$$\gamma = \sum_e (Z_t - Z_d)^T M_e^{-1} (Z_t - Z_d), \tag{4.4}$$

the matrix $M_e$ being

$$M_e = (C_{l,d}^T C_{l,d})^{-1} N_e + \sigma_e^2 I_e^T I_e + \sigma_{w,e} A^T A, \tag{4.5}$$

where $Z_t = \ln(C_{l,t'})$ and $Z_d = \ln(C_{l,d})$ and where the vector $A$ expresses the dependence on $l$ of the beam uncertainty (in the case of a Gaussian beam, $A = l_1^2, l_2^2, ..., l_i^2$). This is the likelihood we use for the pre-WMAP data.
Our theoretical model depends on two scalar field parameters [$n$ for the uncoupled case, and $n$, $\beta$ for the coupled case], and four cosmological parameters plus the overall normalization

$$n_s, h, \omega_b, \omega_c, A, \tag{4.6}$$

where the $c$ subscript donotes the dark matter, while the $b$ subscript donotes baryons. We fix the optical depth to $\tau = 0.17$, the best fit found by WMAP (Kogut et al. 2003). We derived the likelihood also for $\tau = 0.1$ and found no significant difference for as concerns the dark energy parameters. The initial conditions for the scalar field are found iteratively fo each set of cosmological parameters. The overall normalization is integrated out numerically. We again calculate the theoretical $C_{l,t}$ by a modified paralellized CMBFAST code (Seljak & Zaldarriaga 1997) that includes the full set of coupled perturbation equation

(see Amendola (2000)). The other parameters are set as follows: $T_{cmb} = 2.726K$, $Y_{H_e} = 0.24$, $N_\nu = 3.04$.

We evaluated the likelihood on two grids of roughly $50,000$ models each (for each normalization): a sparse grid that covers a broad volume was used as a preliminary exploration; a second denser grid centered on the peaks of the first was then used for the actual calculations. For the first grid we adopted the following top-hat broad priors: $\beta \in (0, 0.3)$ , $n \in (0.25, 20)$, $\omega_b \in (0.005, 0.04)$, $\omega_c \in (0.05, 0.3)$. For the Hubble constant we adopted the top-hat prior $h \in (0.5, 0.9)$; we also employed the HST result but found only minor differences, since the WMAP results are already very close to it, for what concern the Hubble constant. Finally we put a reasonable age constraint ($> 10$ Gyr).

## 4.3 Coupled dark energy

In this second class of coupled dark energy models the background continuity equations for the scalar field, dark matter and radiation are Eq. (2.10), Eq. (2.11), Eq. (2.14), while the baryon energy density evolve in the usual way, i.e. $\dot{\rho_b} + 3H\rho_b = 0$. Immediately after equivalence, the Universe enters the $\phi$MDE stage (see Sec. 2.3), where $V$ is negligible and, accordingly, the correction is indipendent of the potential shape. By solving the Friedmann equation (2.13) we find that

$$a \propto t^{4/(6+4\beta^2)}, \tag{4.7}$$

i.e. the scale factor grows more slowly than in a pure matter dominated era. During the $\phi$MDE, $V$ gradually increases and, eventually, approaches and exceeds the dark energy kinetic term; then the Universe enters the tracking phase, and finally reach the *global attractor*, when the dark energy density overwhelms dark matter and any other densities.

Along the expansion history, the scaling of $\rho_c$ is modified with respect to the uncoupled case and reads

$$\rho_c = \frac{\rho_{c0}}{a^3} e^{(-\sqrt{\frac{16\pi G}{3}}\beta(\phi-\phi_0))}, \tag{4.8}$$

meanwhile the baryon density grows as $a^{-3}$, as usual. In Chapter 5 we shall see in more details that these behaviours strongly affect the fluctuation growth, even in the newtonian regime: the dark matter density fluctuations, instead of growing as $\sim a$ are enhanced during all the $\phi$MDE, and grow as

$$\delta \sim a^{1+\frac{4}{3}\beta^2}. \tag{4.9}$$

This epoch has several features that distinguish it from tracking: it is very long (from equivalence up to $z \approx 10$); it cannot be avoided even assuming an extremely small initial dark energy density (contrary to the tracking that may be avoided by selecting initial conditions with very low scalar field energy - the so called "undershooting" trajectories). Since during the tracking phase the equation of state of dark energy depends only onthe potential parameter $n$ (cf. Eq. (3.18)), the cosmic evolution depends on $\beta$ alone during the $\phi$MDE, and on $n$ alone during the tracking. Since the position of the acoustic peaks is related to the equation of state through the angular diameter distance, it appears that the CMB is able tu put direct constraints on both $\beta$ and $n$.

There is however a crucial difference between the $\phi$MDE and a tracking for what concerns here: while the present equation of state, set by the tracking, is degenerated with $h$ for as concerns the CMB spectrum (see e.g. Bean & Melchiorri (2002)), the equation of state during $\phi$MDE is not. In fact, the angular diameter distance to the last scattering surface is degenerate along lines $h(w_\phi)$ for which

$$d_A \sim \int_{a_{dec}}^{1} [\omega_c a + (h^2 - \omega_c) a^{4-3w_\phi}]^{-1/2} da = const., \tag{4.10}$$

(although it is exact only for $\beta = 0$ it remains a good approximation even for small non-zero values). On the other hand , the fact that $\Omega_\phi \neq 0$ at decoupling in coupled models implies that the effect of the coupling on the CMB are not due solely to the angular diameter distance, and therefore the geometric degeneracy can be broken. This is shown in Fig. 4.1 in which $C_l$ spectra for various values of $\beta$ (all other parameters being equal) are shown: the spectra change both in amplitude and in peak's position.

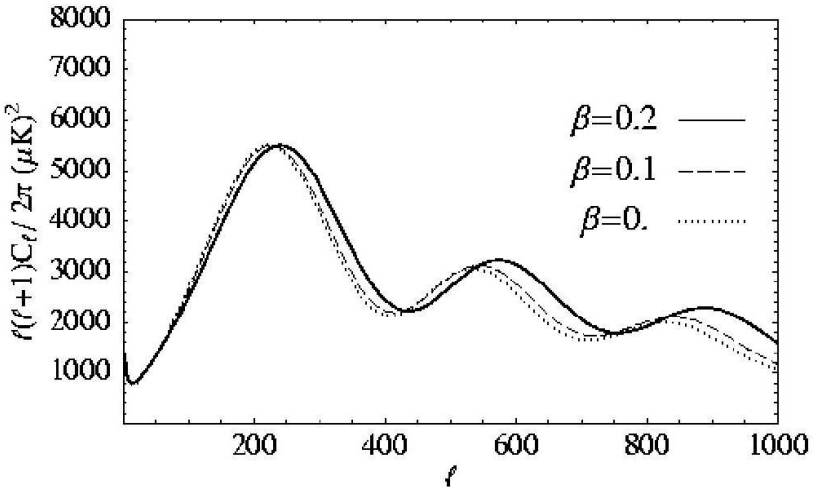


Figure 4.1: Different CMB anisotropy power spectra for different values of $\beta$.

## 4.4 Constraints

We begin by putting $\beta = 0$. In Fig. 4.2 we show the likelihood for each parameter, marginalizing in turn over the others. The dotted line is for the HST prior. Notice that, due to the degeneracy between $w_\phi$ and $h$, the limits on $w_\phi$ are rather weak, especially if no prior is assumed. The numerical results are in Table 4.1. Here and in the following the limits are always at the 68%(95%) C.L., while the errors are at 68% C.L.. As expected, we find results very close to those in Spergel et al. (2003). The small residual differences are probably due to the fact that we use a grid instead a Markov chain and fix $\tau$ instead of marginalizing over it. In Fig. 4.3 we show the likelihood for $w_\phi$ and for the potential parameter $n$, marginalizing over the other parameters. We find the following constraints at 95% C.L.:

$$n < 2.08, \qquad \beta < 0.13. \tag{4.11}$$

Notice that this implies that an exponential potential (corresponding to $n \to \inf$) is rejected even for $\beta \neq 0$. In place of $n$ one can use as well as likelihood variable the equation of state during tracking. Then we obtain at the 95% C.L.

$$-1 \leq w_\phi < -0.49. \tag{4.12}$$

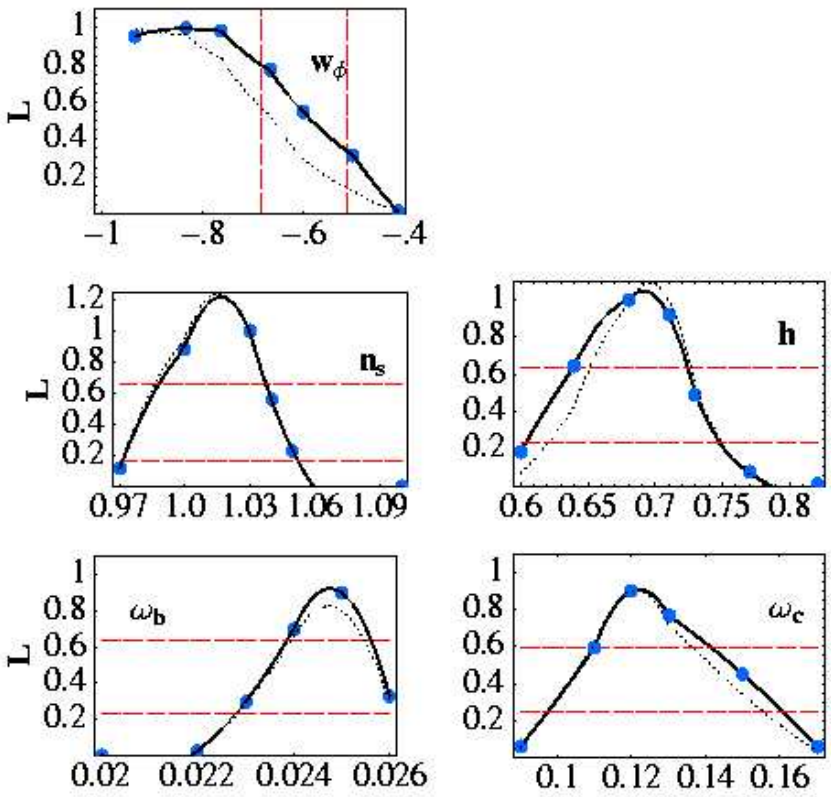


Figure 4.2: Likelihood functions for uncoupled dark energy models, in arbitrary units. In each panel the other parameters have been marginalized. The dotted lines are for the HST prior on the Hubble constant. The horizontal long-dashed lines are the confidence levels at 68 and 95%. The vertical long-dashed lines in the panel for $w_\phi$ mark the upper bounds at 68 and 95% C.L..

| Parameter | **WMAP** | **HST** |
|---|---|---|
| $w_\phi$ | $< -0.68(-0.51)$ | $< -0.73(-0.55)$ |
| $n$ | $< 0.94(1.92)$ | $< 0.74(1.64)$ |
| $h$ | $0.69^{+0.04}_{-0.05}$ | $0.70^{+0.03}_{-0.05}$ |
| $n_s$ | $1.01 \pm 0.022$ | $1.01 \pm 0.022$ |
| $\omega_b$ | $0.0247 \pm 0.001$ | $0.0247 \pm 0.0008$ |
| $\omega_c$ | $0.12^{+0.02}_{-0.01}$ | $0.12^{+0.015}_{-0.01}$ |

Table 4.1: Uncoupled case.

In Fig. 4.4 we report the likelihood for all the parameters, contrasting the WMAP

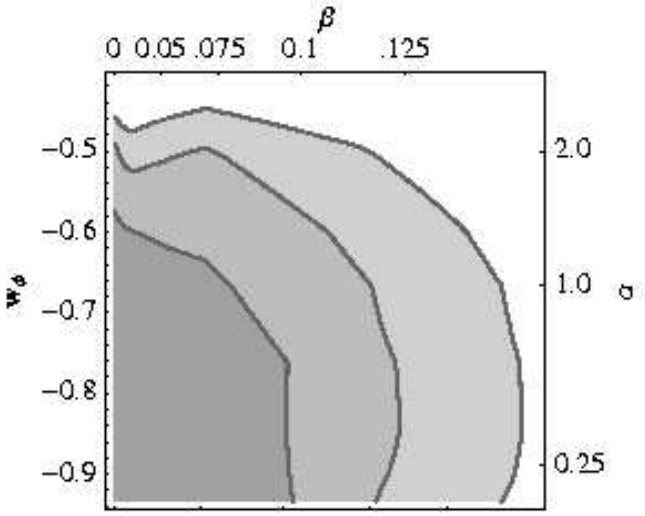


Figure 4.3: Likelihood contours plots in the space $n$ (or $w_\phi$), $\beta$, marginalizing over the other parameters at the $68, 95$ and $99\%$.

estimation with the pre-WMAP one (the limit on $\beta$ stated in Amendola et al. 2003 was slightly different because here we include more pre-WMAP data). As it can be seen, WMAP puts quite stronger limits on $w_\phi$ and on $\beta$. In particular, the likelihood for $w_\phi$ now vanishes for $w_\phi > -0.4$. However, CMB seems to be more sensitive to the dark energy coupling than to its potential.

The other parameters are given in Table 4.2. It appears that the limits on the cosmological parameters $n_s, \omega_b, \omega_c$ are almost independent of $\beta$, while a non-zero $\beta$ favors higher $h$. The degeneracy $\beta - h$ is reported in Fig. 4.5. In Fig. 4.6 we show the contour plot of the likelihood $L(\Omega_m, w_\phi)$, where $\Omega_m = \Omega_c + \Omega_b$, marginalizing over the other parameters. We also add the confidence region from the Hubble diagram of SNe Ia (here we used the fit C of Perlmutter et al. 1999, plus the supernova SN1997ff at $z \approx 1.75$, Benitez et al. 2002). The product of the two likelihood functions is shown in the same figure. It turns out that $\Omega_\phi = 0.67 \pm 0.05$ and $w_\phi < -0.76(95\%\text{C.L.})$ (see Fig. 4.7). The limit on $w_\phi$ is very close to that obtained in Spergel et al. (2003): this shows that this bound is almost independent of the coupling $\beta$.

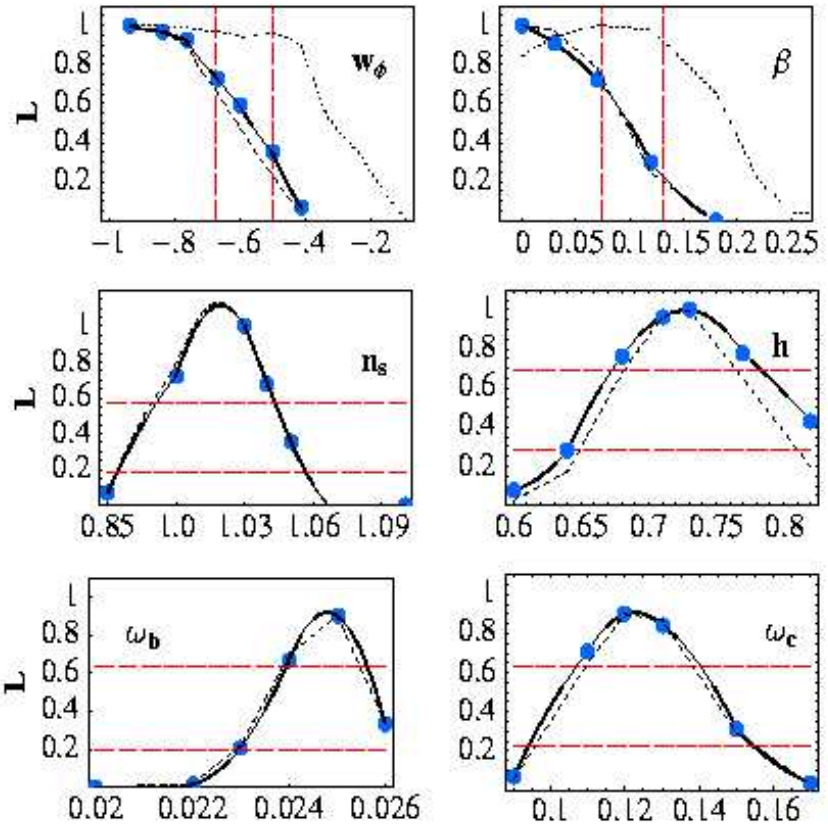


Figure 4.4: Marginalized likelihood for tracking trajectories. The solid curves are for the WMAP data, the short-dashed curves are for the HST prior, and the dotted curves in the panels for $w_\phi$ and $\beta$ for the pre-WMAP compilation. The horizontal long-dashed lines are the confidence levels at 68 and 95%. The vertical long-dashed lines in the panel for $w_\phi$ mark the upper bounds at 68 and 95% C.L..

| Parameter | **WMAP** | **HST** | **pre-WMAP** |
|---|---|---|---|
| $w_\phi$ | $< -0.67(-0.49)$ | $< -0.69(-0.52)$ | $< -0.50(-0.25)$ |
| $n$ | $< 0.99(2.08)$ | $< 0.90(1.84)$ | $< 2.0(6.0)$ |
| $\beta$ | $< 0.075(0.13)$ | $< 0.072(0.13)$ | $< 0.13(0.19)$ |
| $h$ | $0.73 \pm 0.05$ | $0.73 \pm 0.04$ | $> 0.62(0.55)$ |
| $n_s$ | $1.019 \pm 0.025$ | $1.018 \pm 0.025$ | $0.97 \pm 0.03$ |
| $\omega_b$ | $0.0247 \pm 0.0008$ | $0.0250 \pm 0.0008$ | $0.021 \pm 0.003$ |
| $\omega_c$ | $0.123 \pm 0.016$ | $0.120 \pm 0.016$ | $0.12 \pm 0.04$ |

Table 4.2: Coupled case.

The constraints on the coupling imply that this new interactions is at least $1/\beta^2 \approx 60$ times weaker than ordinary tensor gravity. As shown in Amendola (1999), the limit on $\beta$ can be restated as a limit on the constant $\xi$ of the non-minimally coupled gravity, $\xi < 0.01$. We have shown in Amendola et al. (2003) that an experiment like the planck mission can lower the upper bound to $\beta$ to 0.05, a limit comparable to the constraint that local gravity experiments impose on the extra coupling to baryons, $\beta^2_{baryons} < 10^{-2}$ (see e.g. Hagiwara et al. 2002).

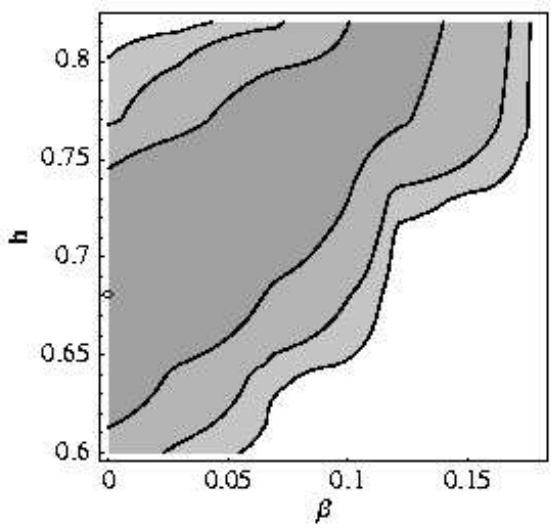


Figure 4.5: Likelihood for $\beta$ and $h$.

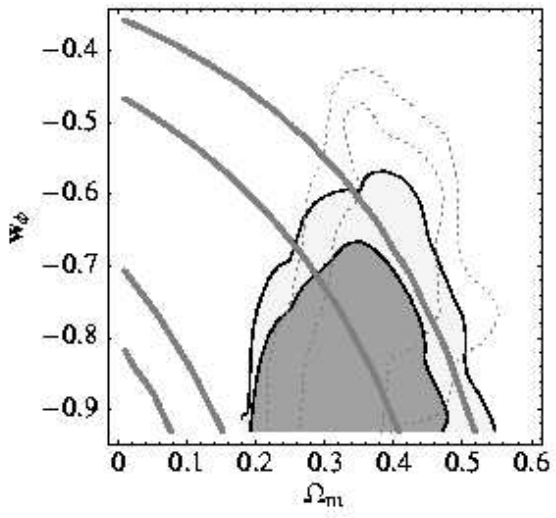


Figure 4.6: Contour plot of the likelihood function $L(\Omega_m, w_\phi)$. The dotted lines are for the WMAP only, the thick gray lines for the supernovae Ia, and the gray regions are for the combined WMAP+SNe Ia (all contours are at 68 and 95% C.L..)

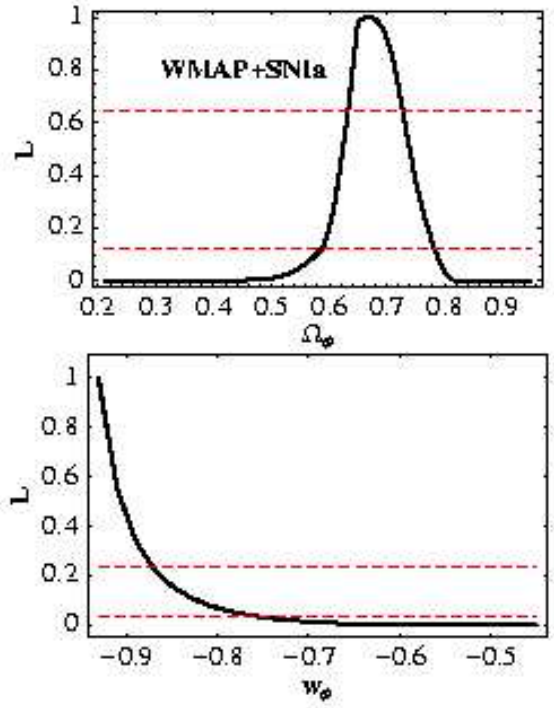


Figure 4.7: Likelihood for $\Omega_m$ and $w_\phi$ including the constraints from supernovae Ia (marginalizing over the other parameters including $\beta$).

# Chapter 5

# Beyond linearity: an analytical approach

Dark energy is defined as a fluid distributed almost homogeneously and whose potential energy dominates over kinetic energy. As such, it can be observed mainly through large scale effects as those relating to the cosmic expansion history and its linear fluctuations. Indications concerning the growth of linear fluctuations, e.g. via the ISW effect (Corasaniti et al. 2003; Fosalba et al. 2003) are still very tentative, although the prospects from e.g. weak lensing (Benabed & Bernardeau 2001) and Lyman-$\alpha$ clustering (Mandelbaum et al. 2003; Calvão et al. 2002a) appear promising. However, all these observables depend ultimately on dark energy only through the expansion history $H(z)$ and the linear growth function $G(z)$.

At any given redshift there will be different dark energy equations of state $w_\phi(z)$ that give indistinguishable $H(z)$ and the degree of degeneration will increase with redshift. In principle the degeneracy can be broken by a large number of observations at different $z$ of $H(z)$ and/or $G(z)$. However, this is hardly feasible, since real data is confined to small ($z < 5$, like SNe Ia) or large redshifts ($z \approx 1100$, like CMB). Moreover, in most models the dark energy component become subdominant at $z \gg 1$, so that both $H(z)$ and $G(z)$ becomes rapidly insensitive to $w_\phi(z)$ (see e.g. Kujat et al. (2002)). It would be desirable therefore to make a step forward from linearity. As usual, non-linearity can be approached in two ways: perturbatively, i.e. going up in perturbation theory, or non-perturbatively, i.e. performing fully non-linear $N$-body simulations. We will analyse the latter approach in the next Chapter. For as concern the perturbative approach we will see in this Chapter how the skewness results to be a third independent observable function of dark energy. Since the coupling is a form of species-dependent scalar gravity, the skewness will in fact measure the violation of the equivalence principle. Part of the material presented in this Chapter refers to Amendola & Quercellini (2004) and Macciò et al. (2004).

## 5.1 Dynamics in the newtonian regime

As we remarked in Sec. 4.4 the upper bounds on a scalar interaction with baryons are very strong, of the order of

$$\beta_b < 0.01, \tag{5.1}$$

(Hagiwara et al. 2002), (in Khoury & Weltman (2004) it has been proposed a model in which such constraints can be escaped but only for suitably chosen potentials). The bounds on a coupling to dark matter are however much weaker. In Gradwohl & Frieman (1992) astrophysical observations were employed to derive $\beta < 1.5$ (we keep on dropping the subscript $c$ for the dark-dark coupling) roughly; as we will see in details in the next Chapter, N-body simulations have shown that

the dark matter halo profile depends sensitively on $\beta$ in a class of dark energy models but, due to the controversial status of the halo profile observations, it is difficult to derive firm upper limits. Finally, in Chapter 4 we found that CMB requires $\beta < 0.13$; however, this result assumes that the coupling remains constant throughout the Universe lifetime and it is actually most sensitive to the value of $\beta$ at early times.We can summarise the observational situation with respect to $\beta$ by saying that there are no strong upper bounds to the *present* value af a scalar field coupling to dark matter; if $\beta$ varies with time, then even a value of order unity at present is not definitively excluded. Since the baryons are practically uncoupled , the scalar interaction violates the equivalnce principle. The value of $\beta$ is therefore also a measure of the equivalence principle violation.

### 5.1.1 Perturbation equations

Let us now consider density fluctuations and discuss their evolution in a coupled dark energy model. From now on for pratical reasons, in all the equations, the "time" independent variable will be $\alpha$, defined as $\ln a$.
First of all, the conformal metric must be modified to take into account the local gravitational fields and, in the absence of anisotropic stresses, reads

$$ds^2 = a^2[-(1+2\Phi)d\tau^2 + (1-2\Phi)dx_i dx^j], \tag{5.2}$$

$\Phi$ being the gravitational potential. Differentiation in respect to $\alpha$ will be indicated by $'$. As usual, fluctuations are expanded in Fourier components; let us then consider a component of wavenumber $k$ and define $\lambda = H/k$.
Baryons and CDM will be considered as fluids; fluctuations will then be characterized by density fluctuations

$$\delta^{c,b} = \delta\rho_{c,b}/\rho_{c,b} \tag{5.3}$$

($^{c,b}$ stand for CDM and bayons) and velocity fields $v_i^{c,b} \equiv dx_i/d\tau$, from which we build the scalar variables

$$\theta^{c,b} = i\frac{k_i v_i^{c,b}}{H}. \tag{5.4}$$

Scalar field fluctuations ($\delta\phi$) will then be described by the variable

$$\varphi = \sqrt{\frac{3}{4\pi G}}\,\delta\phi. \tag{5.5}$$

Dealing with fluctuation evolution well after recombination, we shall neglect their radiation component.

Taking into account density inhomogeneities, the conservation equations for the stress-energy tensor (1.5) yield the dependence of $\delta^{c,b}$ and $\theta^{c,b}$ on the scale factor $a$. The Friedman equation (2.13) shall then be used to obtain the dependence on time. We shall omit here the general form of these equations and will write them in the Newtonian limit, i.e. for small scales (in comparison with the horizon scale $\sim H^{-1}$) and small velocities (with respect to $c$). The former condition tells us to consider the lowest order terms in the wave length $\lambda$; in this limit, the gravitational potential fulfills equations that can be written in a simpler form by defining the function $f(\phi)$ according to

$$V(\phi) = A\exp\left[\sqrt{16\pi G/3}f(\phi)\phi\right], \tag{5.6}$$

as well as the functions

$$f_1 = \phi\frac{df}{d\phi} + f, \quad f_2 = f_1^2 + \sqrt{\frac{3}{16\pi G}}\frac{df_1}{d\phi}; \tag{5.7}$$

notice that this is no restriction on the potential shape. Then

$$\Phi = -\frac{3}{2}\lambda^2(\Omega_b\delta^b + \Omega_c\delta^c + 6X\varphi + 2X\varphi' - 2Y^2 f_1\varphi) \tag{5.8}$$

$$\Phi' = 3x\varphi - \Phi, \tag{5.9}$$

while the scalar field fulfills the equation

$$\varphi'' + \left(2 + \frac{H'}{H}\right)\varphi' + \lambda^{-2}\varphi - 12X\varphi + 4\Phi X + 2Y^2(f_2\varphi - f_1\Phi) = \beta\Omega_c(\delta^c + 2\Phi). \tag{5.10}$$

These expressions have been simplified by using the variables $X^2 = 8\pi G\rho_k(\phi)a^2/3H^2$ and $Y^2 = 8\pi GV(\phi)a^2/3H^2$, respectevely the kinetic and the potential fraction of dark energy density; notice that, if the dark energy kinetic (or potential) energy density gives a substantial contribution to the expansion source, $X$ (or $Y$)

is $\mathcal{O}(1)$.

In the Newtonian limit, however, we also neglect the derivatives of $\varphi$, averaging out the rapid oscillations of $\varphi$ and the potential term $f_2 Y^2 \varphi$; this actually requires that $\lambda \ll (f_2 Y)^{-1}$ (remind that $Y$ is $\mathcal{O}(1)$). Furthermore, in eq. (5.10), the metric potential $\Phi$, which is proportional to $\lambda^2$, can also be neglected. Accordingly, eq. (5.8) becomes

$$\Phi = -\frac{3}{2}\lambda^2(\Omega_b \delta^b + \Omega_c \delta^c), \tag{5.11}$$

which is the usual Poisson equation, while eq. (5.10) simplifies into

$$\lambda^{-2}\varphi \simeq \beta \Omega_c \delta^c. \tag{5.12}$$

In the same way, one obtains the continuity equations

$$\delta^{c\,\prime\prime} = -\frac{F_c}{2}\delta^{c\,\prime} + \frac{3}{2}S_c\delta^c, \tag{5.13}$$

$$\delta^{b\,\prime\prime} = -\frac{F_b}{2}\delta^{b\,\prime} + \frac{3}{2}S_b\delta^c, \tag{5.14}$$

and the Euler equations

$$\theta^{c\,\prime} = -\frac{F_c}{2}\theta^c - \frac{3}{2}S_c\delta^c, \tag{5.15}$$

$$\theta^{b\,\prime} = -\frac{F_b}{2}\theta^b - \frac{3}{2}S_b\delta^c, \tag{5.16}$$

where the two functions, the friction $F_{c,b}(\alpha)$ and the source $S_{c,b}(\alpha)$, are in general time dependent and correspond to

$$F_c(\alpha) = 2\Big(1 + \frac{H'}{H} - 2\beta X\Big); \qquad F_b(\alpha) = 2\Big(1 + \frac{H'}{H}\Big); \tag{5.17}$$

$$S_c(\alpha) = \Omega_c\Big(1 + \frac{4}{3}\beta^2\Big); \qquad S_b(\alpha) = \Omega_c + \Omega_b \approx \Omega_c. \tag{5.18}$$

## 5.2 Skewness

The normalised third order moment of the galaxy distribution, or *skewness*, is defined as

$$S_3 \equiv \frac{< \delta(x)^3 >}{(< \delta(x)^2 >)^2}, \tag{5.19}$$

where $\delta(x)$ is the density contrast at the point x. Its value at large (weakely non-linear) scales can be calculated exactly assuming that structure formation forms only via gravitational instability: in a flat Universe dominated by matter with Gaussian initial conditions the well-known result is $S_3 = 34/7$ (see Sec. 5.2.1, Peebles (1980)). If the density contrast is smoothed through a window function of typical size $R$ the skewness becomes (Fry 1986; Bernardeau 1994)

$$\hat{S_3} = S_3 + \frac{d \ln \sigma^2(R)}{d \ln R}, \tag{5.20}$$

where $\sigma^2$ is the variance of the density field smoothed through the same window function. In a series of papers it has been shown that $S_3$ remains extremely close to 34/7 in dark energy models (Martel 1995; Kamionkowski & Buchalter 1999; Benabed & Bernardeau 2001), in curved spaces (Bouchet et al. 1992; Catelan 1995), in brane induce gravity (Multamäki et al. 2003) and in Brans-Dicke model (Gaztañaga & Lobo 2001), with deviations that hardly exceed one per cent in the observationally acceptable range of cosmological parameters. These results have shown that $S_3$ can be considered one of the best probe of the gravitational instability picture at large scales (Bernardeau et al. 2002). Only scenarios with radically different features predict values of $S_3$ that deviates sensitively from the standard results: non-Gaussian initial conditions (Fosalba & Gaztanaga 1998), cosmic strings (Avelino et al. 1998), Cardassian cosmologies (Multamäki et al. 2003), and modified gravity models based on Birkhoff's law (Lue et al. 2004).
Since the skewness is such a good test of gravity, it seems interesting to ask whether it is also a good test of the universality of gravity, i.e. of the equivalence principle. Even more intersting is the question whether such a possible violation can be mediated by a dark energy scalar field. In other words, it's worth investigating the effect on $S_3$ of a scalar field coupled to matter in a species-dependent way.

### 5.2.1 Perturbation expansion

In this Subsection we will drop the subscript for baryons and dark matter and we will derive the general expression for second order perturbation equations and

the skewness for both baryons and dark matter.

Following the notation of **?**) and Kamionkowski & Buchalter (1999), we expand the scalar-Newtonian equations in a perturbation series,

$$\delta = \sum_i \delta^{(i)}, \tag{5.21}$$

and assume that $\delta^{(i)}$ is of order of the density contrast at initial time $[\delta^{(i)}]^i$. To the first order we obtain a generalization of the usual perturbation equations

$$\delta^{(1)\,\prime\prime} + \frac{F}{2}\delta^{(1)\,\prime} - \frac{3}{2}S\delta^{(1)} = 0. \tag{5.22}$$

It is convenient to define the growth function $D_1(\alpha)$,

$$\delta^{(1)} = D_1(\alpha)\delta_0^{(1)}, \tag{5.23}$$

where $\delta_0^{(1)}$ is the density contrast at the initial time (assumed Gaussian distributed); we also find it useful to define the growth exponent $m(\alpha) = d\log\delta^{(1)}/d\alpha = D_1{}'/D_1$. It follows then that $m(\alpha)$ is determined by the equation

$$m' + m^2 + \frac{F(a)}{2}m - \frac{3}{2}S(a) = 0. \tag{5.24}$$

For $F = S = 1$ the solutions are the standard growth and decaying exponents $m = 1, -3/2$.

We now proceed to the second order. The equation become

$$\delta^{(2)\prime\prime} + \frac{F}{2}\delta^{(2)\prime} - \frac{3}{2}S\delta^{(2)} = \frac{3}{2}S\delta^{(1)2} + \frac{3}{2}S\delta^{(1)}_{,i}\Delta^{(1)}_{,i} + \nabla_i\nabla_j[v_i^{(1)}v_j^{(1)}], \tag{5.25}$$

where $\Delta \equiv \Phi/(4\pi\rho a^2)$ and the Poisson equation (5.11) becomes

$$\nabla_i\nabla_i\Delta = \delta. \tag{5.26}$$

Taking the Fourier transform we obtain

$$\begin{aligned}\delta_k^{(2)\prime\prime} + \frac{F}{2}\delta_k^{(2)\prime} - \frac{3}{2}S\delta_k^{(2)} &= \frac{3}{2}S\left[\delta^{(1)}_{k_a} * \delta^{(1)}_{k_b}\right]_k - \frac{3}{2}S[\mathbf{k}_a\delta^{(1)}_{k_a} * \mathbf{k}_b\Delta^{(1)}_{k_b}]_k \\ &- [(\mathbf{k}_a + \mathbf{k}_b)\cdot\mathbf{v}^{(1)}_{k_a} * (\mathbf{k}_a + \mathbf{k}_b)\cdot\mathbf{v}^{(1)}_{k_b}]_k\end{aligned}$$

where the convolution $[*]$ is defined as

$$[F_{k_a} * F_{k_b}]_k \equiv \frac{V}{(2\pi)^3} \int d^3k_a d^3k_b \delta_D(k_a + k_b - k) F(k_a) F(k_b). \tag{5.27}$$

We need also the Fourier transform of the relation (6.2), which gives

$$\Delta_k = -\frac{\delta_k}{k^2}, \tag{5.28}$$

(from which we see that $\Delta_k^{(1)}$ grows with the same exponent as $\delta_k^{(1)}$, $\Delta_k^{(1)} \sim e^{\int m(\alpha) d\alpha}$) and the Fourier transform of (2.3) at first order

$$ik_i v_{k,i}^{(1)} = -m\delta_k^{(1)}, \tag{5.29}$$

which gives, if $\nabla \times v = 0$,

$$v_{k,i}^{(1)} = i\frac{k_i}{k^2} m\delta_k^{(1)}. \tag{5.30}$$

We obtain then

$$\begin{aligned} \delta_k^{(2)\prime\prime} + \frac{F}{2}\delta_k^{(2)\prime} - \frac{3}{2}S\delta_k^{(2)} &= (\frac{3}{2}S + m^2)\left[\delta_{k_a}^{(1)} * \delta_{k_b}^{(1)}\right]_k + (\frac{3}{2}S + 2m^2)[\mathbf{k}_a\delta_{k_a}^{(1)} * \frac{\mathbf{k}_b}{k^2}\delta_{k_b}^{(1)}]_k \\ &+ m^2[\frac{\mathbf{k}_a \cdot \mathbf{k}_b}{k_a^2}\delta_{k_a}^{(1)} * \frac{\mathbf{k}_a \cdot \mathbf{k}_b}{k_b^2}\delta_{k_b}^{(1)}]_k. \end{aligned}$$

We separate now the time dependence of the first order perturbation, using the relation $\delta_k^{(1)} = D_1(\alpha)\delta_{0k}^{(1)}$. Then we have

$$\delta_k^{(2)\prime\prime} + \frac{F}{2}\delta_k^{(2)\prime} - \frac{3}{2}S\delta_k^{(2)} = \frac{3}{2}SD_1^2(A_k + B_k) + m^2 D_1^2(A_k + 2B_k + C_k), \tag{5.31}$$

where

$$\begin{aligned} A_k &= \left[\delta_{0k_a}^{(1)} * \delta_{0k_b}^{(1)}\right]_k, \\ B_k &= [\mathbf{k}_a\delta_{0k_a}^{(1)} * \frac{\mathbf{k}_b}{k^2}\delta_{0k_b}^{(1)}]_k, \\ C_k &= [\frac{\mathbf{k}_a \cdot \mathbf{k}_b}{k_a^2}\delta_{0k_a}^{(1)} * \frac{\mathbf{k}_a \cdot \mathbf{k}_b}{k_b^2}\delta_{0k_b}^{(1)}]_k \end{aligned}$$

are time-independent terms.

The general solution of (5.31) is the sum of the homogeneous and a particular inhomogeneous solution. It will be shown that the latter always dominates. A particular solution will have the form (Kamionkowski & Buchalter 1999)

$$\delta_k^{(2)} = D_{2a}(\alpha)(A_k + B_k) + D_{2b}(\alpha)(A_k + 2B_k + C_k) \tag{5.32}$$

where the functions $D_{2a}, D_{2b}$ obey the equations

$$\begin{aligned} D''_{2a} + \frac{F}{2}D'_{2a} - \frac{3S}{2}D_{2a} &= \frac{3S}{2}D_1^2 \\ D''_{2b} + \frac{F}{2}D'_{2b} - \frac{3S}{2}D_{2b} &= m^2 D_1^2 \end{aligned} \tag{5.33}$$

(with initial conditions $D_{2a,b}(\alpha_{in}) = D'_{2a,b}(\alpha_{in}) = 0$ ). Moreover, it can be shown that

$$D_{2b} = (D_1^2 - D_{2a})/2 \tag{5.34}$$

Therefore the solution in terms of $\mu = D_{2a}/D_1^2$ is

$$\delta_k^{(2)} = \frac{1}{2}D_1^2[(1+\mu)A_k + 2B_k + (1-\mu)C_k] \tag{5.35}$$

or explicitely

$$\delta_k^{(2)} = \frac{1}{2}D_1^2\frac{V}{(2\pi)^3}\int dk_1 dk_2 \delta_D(k_1+k_2-k)K(k_1,k_2)\delta_{0k_1}\delta_{0k_2} \tag{5.36}$$

where the symmetrized kernel is (Fry 1986)

$$K(k_1,k_1) = (1+\mu) + \frac{\mathbf{k_1}\cdot\mathbf{k_2}}{k_1 k_2}\left(\frac{k_1}{k_2} - \frac{k_2}{k_1}\right) + (1-\mu)\left(\frac{\mathbf{k_1}\cdot\mathbf{k_2}}{k_1 k_2}\right)^2 \tag{5.37}$$

Let us now evaluate the third order moment of the spatial density field

$$< \delta(x)^3 > \approx 3 < \delta^{(1)2}\delta^{(2)} > \tag{5.38}$$

This gives

$$\begin{aligned} < \delta(x)^3 > &\approx 3 < \delta^{(2)}\delta^{(1)2} > = \\ & \frac{3}{2}D_1^4 \int dk_1 dk_2 dk_3 dk_4 < \delta_{k_1}\delta_{k_2}\delta_{k_3}\delta_{k_4} >_0 \; K(k_1,k_2)e^{i(k_1+k_2+k_3+k_4)x} \end{aligned} \tag{5.39}$$

where the coefficients inside average brackets are at the initial time. Since initially the field is assumed Gaussian, the average can be decomposed into a sum of all possible pairings

$$\begin{aligned} < \delta_{k_1}\delta_{k_2}\delta_{k_3}\delta_{k_4} >_0 &= < \delta_{k_1}\delta_{k_2} >_0 < \delta_{k_3}\delta_{k_4} >_0 + < \delta_{k_1}\delta_{k_3} >_0 < \delta_{k_2}\delta_{k_4} >_0 \\ &+ < \delta_{k_1}\delta_{k_4} >_0 < \delta_{k_2}\delta_{k_3} >_0 \end{aligned}$$

The first right-hand-side pair averages to zero because $< \delta^{(2)} >= 0$ , while the two remaining terms give an identical contribution (Bernardeau et al. 2002). Since by definition of power spectrum $< \delta_{k_1}\delta_{k_3} >_0 = P(k)\delta_D(k_1 - k_3)$ the result is

$$< \delta(x)^3 > \approx 3 < \delta^{(2)}\delta^{(1)2} >= 3D_1^4 \frac{V}{(2\pi)^3} \int dk_1 dk_2 P(k_1)P(k_2)K(k_1, k_2) \quad (5.40)$$

We can integrate out the angle between $k_1$ and $k_2$ , using the angular averages

$$\begin{aligned} < \left(\frac{\mathbf{k_1}\cdot\mathbf{k_2}}{k_1 k_2}\right)^2 > &= < \cos\theta_{12}^2 >= 1/3 \\ < \left(\frac{\mathbf{k_1}\cdot\mathbf{k_2}}{k_1 k_2}\right) > &= < \cos\theta_{12} >= 0 \end{aligned} \quad (5.41)$$

so that finally the *unsmoothed* spatial skewness is

$$S_3 = \frac{< \delta(x)^3 >}{(< \delta(x)^2 >)^2} = 3[(1+\mu) + (1-\mu)/3] = 4 + 2\mu \quad (5.42)$$

It is easy to see that in the pure matter case $\mu = 3/7$ and $S_3 = 34/7$ (Peebles 1980).

### 5.2.2 Dark energy with constant equation of state

As shown before , the skewness only depends on the solutions $D_1, D_2 \equiv D_{2a}$ of the equations

$$D_1'' + \frac{F}{2}D_1' - \frac{3S}{2}D_1 = 0, \quad (5.43)$$

$$D_2'' + \frac{F}{2}D_2' - \frac{3S}{2}D_2 = \frac{3S}{2}D_1^2, \quad (5.44)$$

that in general have to be solved numerically. Let us now assume the simplest model of dark energy, with a constant equation of state $w$. The background equations are then

$$\begin{aligned} S(a) = \Omega_c(a) &= \frac{\Omega_c}{\Omega_c + (1-\Omega_c)a^{-3w}}\,, \\ F(a) = 2 + 2\frac{H'}{H} &= \frac{\Omega_c + (1-3w)(1-\Omega_c)a^{-3w}}{\Omega_c + (1-\Omega_c)a^{-3w}}\,. \end{aligned}$$

In the future, for $a \to \infty$, and for $w < 0$, these reduce to $S(a) = \Omega_c a^{3w}/(1-\Omega_c)$ and $F(a) = 1 - 3w$ and we can find analytically that

$$m(a) \sim a^{(3w-1)/2}$$

The general solution however has to be obtained numerically. In Fig. 5.1 we

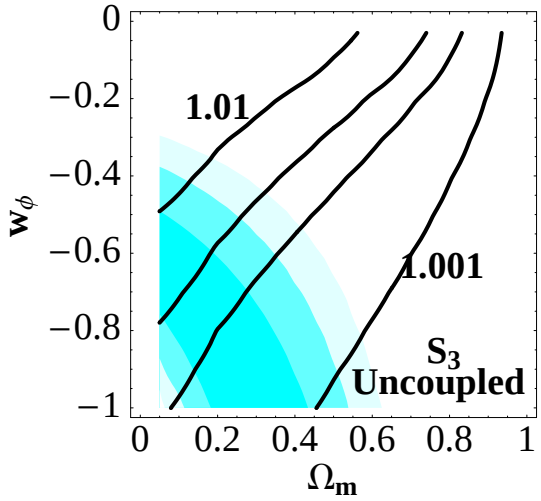


Figure 5.1: Contour plot of the skewness $S_3 \cdot (7/34)$ as a function of $\Omega_m, w_\phi$ at the present time for uncoupled dark ene. The contours are at 1.001,1.002,1.005,1.01, bottom to top. The shaded region is the confidence region of the SNIa at 68%, 95%, 99%, inside to outside.

show the contour plot of the skewness $\hat{S}_3 \equiv S_3 \cdot (7/34)$ at the present time on the parameter space $\Omega_m, w_\phi$ along with the allowed region according to the supernovae Ia (Riess et al. 1998). As anticipated, $S_3$ deviates from 34/7 by 1% at most within the SNIa range; only 0.05% if we further impose $0.2 < \Omega_m < 0.4$. Similar conclusions have been reached in other models of dark energy (Benabed & Bernardeau 2001). This shows that the skewness is not an efficient probe of dark energy.

### 5.2.3 Stationary dark energy

The system of Eq. (2.10), (2.11) and (2.13) is best studied in the new variables (Amendola 2000) $x = \frac{\kappa}{H}\frac{\dot{\phi}}{\sqrt{6}}$, $y = \frac{\kappa}{H}\sqrt{U/3}$, and $v = \frac{\kappa}{H}\sqrt{\rho_b/3}$. If we now consider

an exponential potential of the form

$$V(\phi) = V_0 e^{-\sqrt{\frac{16\pi G}{3}}\mu\phi}, \tag{5.45}$$

then we obtain

$$\begin{aligned} x' &= -\frac{1}{2}\left(3 - 3x^2 + 3y^2\right)x - \mu y^2 + \beta(1 - x^2 - y^2 - v^2), \\ y' &= \mu xy + \frac{3}{2}y\left(1 + x^2 - y^2\right), \\ v' &= -3/2v + \frac{3}{2}v\left(1 + x^2 - y^2\right). \end{aligned} \tag{5.46}$$

The CDM energy density parameter is obviously $\Omega_c = 1 - x^2 - y^2 - v^2$ while we also have $\Omega_\phi = x^2 + y^2$ and $\Omega_b = v^2$. The system is subject to the condition $x^2 + y^2 + v^2 \leq 1$.

The system (5.46) displays two accelerated asymptotic regimes, whose properties are summarized in Table 5.2.3 (a complete analysis of solutions is in Amendola (2000)). Since on these solutions the fluids scale identically with time, it is convenient to define a total equation of state

$$w_e = p_{tot}/\rho_{tot} = x^2 - y^2 \tag{5.47}$$

instead of $w_\phi = p_\phi/\rho_\phi$. The relation is simply

$$w_e = (1 - \Omega_m)w_\phi \tag{5.48}$$

so that now

$$\frac{H'}{H} = -\frac{1}{2}\left[1 + 3w_e\right] \tag{5.49}$$

On all critical points the scale factor expansion is given by $a \sim \tau^{p/1-p} = t^p$, where $p = 2/[3(1 + w_e)]$, while each component scales as $a^{-3(1+w_e)}$. In the same table we report the conditions of stability and acceleration of the critical points, denoting $\mu_+ = (-\beta + \sqrt{18 + \beta^2})/2$. The first accelerated solution ($a$) occurs for all $\beta$ and $\mu < \mu_+$ and $\mu < 3/\sqrt{2}$. This asymptotic solution is completely dominated by dark energy ($\Omega_\phi = 1$); as such it can be reached only in the future. The trajectories leading to it are not radically different from the usual uncoupled

Table 5.1: Critical points.

| Point | $x$ | $y$ | $v$ | $\Omega_\phi$ | $w_e$ |
|---|---|---|---|---|---|
| $a$ | $-\frac{\mu}{3}$ | $\sqrt{1-\frac{\mu^2}{9}}$ | 0 | 1 | $-1+\frac{2\mu^2}{9}$ |
| $b$ | $-\frac{3}{2(\mu+\beta)}$ | $\frac{\sqrt{4\beta^2+4\beta\mu+9}}{2\lvert\mu+\beta\rvert}$ | 0 | $\frac{2\beta^2+2\beta\mu+9}{2(\beta+\mu)^2}$ | $-\frac{\beta}{\mu+\beta}$ |

Table 5.2: Critical points.

| Point | stability | acceleration |
|---|---|---|
| $a$ | $\mu<\mu_+, \mu<\frac{3}{\sqrt{2}}$ | $\mu<\sqrt{3}$ |
| $b$ | $\beta>0, \mu>\mu_+$ | $\mu<2\beta$ |

models. It has been shown in Chapter 4 that in this case there is a strong upper limit on $\beta$ from comparison with CMB data: $\beta < 0.13$. For these values it can be seen that $S_3$ does not deviate much from the standard value.
The second case, $b$ , exists when $\beta > 0$ and $\mu > \mu_+$ and is accelerated for $\mu < 2\beta$. This is an example of stationary solution: $\Omega_c$ and $\Omega_\phi$ are constant. In Tocchini-Valentini & Amendola (2002) however it was found that in order to be consistent with CMB data the solution has to be modified in the past, for instance by making the coupling or the potential slope time-dependent. Here we assume that one such modification ensures the fulfilling of the CMB constraints and that the present universe already reached the stationary solution. This can be safely done for our purpose because the properties of the stationary solution do not depend on the initial conditions. In the following we will assume, accordingly, that the universe already entered this stationary epoch.

We now turn back to Eq. (5.13) and (5.14). Asimptotically , the dark matter drives the evolution of the baryons, so that the two components grow with the same exponent $m(\alpha)$, but with a biased amplitude $b = \delta_b^{(1)}/\delta_c^{(1)}$, which for $F_{c,b}, S_{c,b}$ constants are

$$\begin{aligned} b_\pm &= \frac{3S_b}{3S_c + m_\pm(F_b - F_c)} = [1 \pm \frac{4}{3}\beta(\beta + \frac{xm}{\Omega_c})]^{-1} \\ m_\pm &= \frac{1}{4}\left[-F_c \pm \sqrt{24S_c + F_c^2}\right] = \frac{1}{4}\left[-1 + 3w_e + 4\beta x \pm \Delta\right] \end{aligned} \tag{5.50}$$

where $\Delta^2 = 24(1+4\beta^2/3)\Omega_c + (-1+3w_e+4\beta x)^2$ . This shows that baryons follow the same growth as the dark matter but with a biased amplitude.

In stationary dark energy all the coefficients $F_b, S_b, F_c, S_c, m, b$ are constant, which is of course a powerful simplification. Then $\delta^{(2)}_{c,b}$ is asymptotically proportional to $D_1^2$, so we may put $\delta^{(2)}_c = dD_1^2$ and $\delta^{(2)}_b = b^{(2)}\delta^{(2)}_c$, with $d, b_2$ two constants to be determined. We further simplify by taking at this stage the angular average over the wavenumbers $k$ (5.41). This can be done since the dominant term in $<\delta(x)^3>$ is linear in $<\delta^{(2)}>$. We obtain

$$\delta_b^{(2)\prime\prime} + \frac{F_b}{2}\delta_b^{(2)\prime} - \frac{3}{2}S_b\delta_c^{(2)} = \left(\frac{3}{2}S_b b + \frac{4}{3}m^2b^2\right)D_1^2, \tag{5.51}$$

$$\delta_c^{(2)\prime\prime} + \frac{F_c}{2}\delta_c^{(2)\prime} - \frac{3}{2}S_c\delta_c^{(2)} = \left(\frac{3}{2}S + \frac{4}{3}m^2\right)D_1^2. \tag{5.52}$$

Now, since $D_1' = mD_1$and $D_1'' = m^2D_1$, and using the first order relations (see Eq. (5.24)) $2m^2 + F_cm - 3S_c = 0$ and $2m^2 + F_bm - 3S_b/b = 0$, we obtain

$$\begin{aligned} d &= \frac{8+9R_c}{12+9R_c} \\ b^{(2)} &= \frac{b}{6d}\frac{[9R_b(d+b)+8b^2]}{(2b+3R_b)} \end{aligned} \tag{5.53}$$

where $R_b = S_b/m^2$. Finally, the result is

$$\begin{aligned} S_{3c} &= 6\frac{\delta_c^{(2)}}{\delta_c^{(1)2}} = \frac{16+18R_c}{4+3R_c} \\ S_{3b} &= 6\frac{\delta_b^{(2)}}{\delta_b^{(1)2}} = \frac{b^{(2)}}{b^2}S_{3c} \end{aligned}$$

In terms of the parameters $\mu, \beta$ the results are cumbersome and uninformative, so we do not report them.

It is to be remarked that the second-order bias introduced here, $b^{(2)}$, is different from the second-order bias $b_2$ often employed in literature (see e.g. Bernardeau et al. (2002)). The latter is used to denote the coefficient of the second derivative of a Taylor expansion of the non-linear relation $\delta_g = F(\delta)$ between the underlying smoothed matter density field $\delta$ and the smoothed galaxy density field $\delta_g$. This bias is supposed to arise due to non-gravitational physics or to selection effects;

the bias we study in this paper is instead related to an effective violation of the equivalence principle due to the dark energy interaction.

Perhaps the most interesting property of stationary dark energy is its level of predictivity. We have six observable quantities $(\Omega_c, w_e, m, b, S_{3c}, S_{3b})$, i.e. two for each order (background, linear, second-order), in terms of only two basic parameters, $\mu$ and $\beta$. Since $\Omega_c$ and $w_\phi$ are functions of $\beta, \mu$, all the observable quantitites can be written equivalently in terms of $\Omega_c, w_\phi$, which is what we do in Fig. 5.2. The relations are

$$\beta = -\frac{3(1-\Omega_m)w_\phi}{\sqrt{2(1-\Omega_m)(1+w)}}\,, \tag{5.54}$$

$$\mu = \frac{3(w_\phi - \Omega_m + 1)}{\sqrt{2(1+w_\phi)(1-\Omega_m)}}\,. \tag{5.55}$$

Here $\Omega_m = \Omega_c + \Omega_b$. Let us remark again that all the observables here mentioned are constant in space (on Newtonian scales) and time (after the Universe enters the attractor).

Both skewnesses are observable, at least in principle. In fact, we can estimate the baryonic $S_{3b}$ by looking directly at the distribution of luminous sources and the dark matter $S_{3c}$ by observing the distribution of dark matter through the peculiar velocity field and the weak lensing field. However, the distribution of luminous matter does not necessarily coincide with that of the baryons, although we can expect it does so at very large scales, when the effects of hydrodynamics and strong non-linearities are smeared out. We'll comment on real data in the next Section.

Two limits may be worth citing. For $\beta \to \infty$, $S_{3c} = 14/3 \approx 4.67$ and $S_{3b} \to \infty$, while for $\beta \to 0$ (i.e. for an uncoupled exponential model as in Ferreira & Joyce (1998))

$$S_{3b,c} = \frac{378 + 4(-22\mu^2 + \mu\sqrt{25\mu^2 - 108})}{81 + (-19\mu^2 + \mu\sqrt{25\mu^2 - 108})}\,, \tag{5.56}$$

which is again close to 34/7 within 1% if $\Omega_\phi = \frac{9}{2\mu^2}$ has to be smaller than 0.2 to allow for sufficient structure formation (Ferreira & Joyce 1998). In Fig. 5.2 we show the results in graphical form as contour plots of $m, b, S_{3b}, S_{3c}$ in the plane

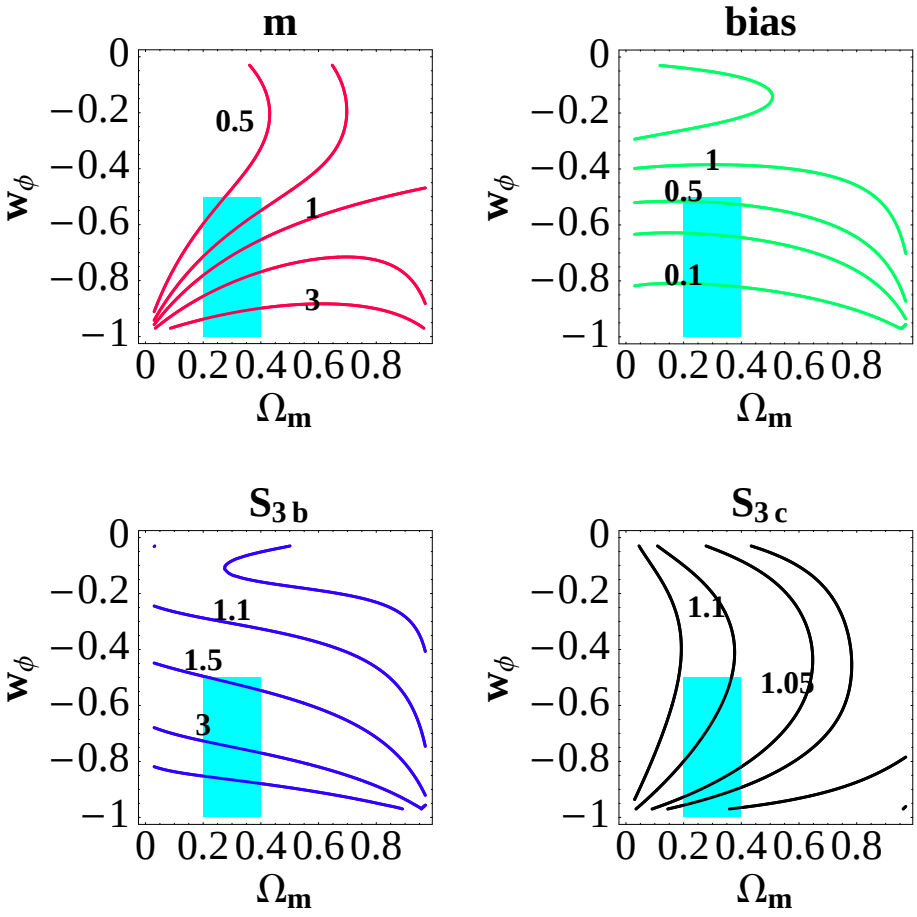


Figure 5.2: Contour plot of the observable quantities $m, b, S_{3b} \cdot (7/34), S_{3c} \cdot (7/34)$ as function of $\Omega_m, w_\phi$. In the plot $m$, the contours are for $m = 0.5, 0.75, 1, 1.5, 3$, top to bottom. In the plot *bias*, the contours are for $1.5, 1, 0.5, 0.3, 0.1$, top to bottom. In the plot $S_{3b}$, the contours are for $1, 1.1, 1.5, 3, 6$, top to bottom. In the plot $S_{3c}$ the contours are for $1.15, 1.1, 1.05, 1.02, 1$, left to right. The shaded area is the allowed region of the SNIa and cluster masses.

$\Omega_m, w_\phi$, overimposing the bounds from SNIa and from cluster masses ($\Omega_m \in (0.2, 0.4)$). This figure summarizes all our findings concerning the six observable quantitites. So far, reliable limits exist only on $\Omega_m$ and $w_\phi$ so we use them to delimit the allowed parameter space.

In Fig. 5.2 we plot first $m(\Omega_m, w_\phi)$. The allowed region constrain $m > 0.5$, roughly, with no upper limit. Interestingly, these values are only slightly larger than those predicted in ΛCDM, $m \approx \Omega_m^{0.6} \approx 0.5$. This makes it clear once again that higher order moments might be necessary to distinguish between models. The plot of $b$ shows that the baryon bias should be smaller than 0.5 (anti-bias). This seems contradicted by observations, that rather point towards $b = 0.8 \pm 0.2$ (see e.g. Bernardeau et al. (2002)), but again we have to remember that most indications of bias are still at scales contaminated by non-gravitational effects; moreover, we refer to the bias of all baryons, not only the small fraction that lights galaxies. The baryons skewness, in units of the standard value 34/7, is predicted to be $S_{3b} > 1.5$, while the CDM skewness $0.96 < S_{3c} < 1.15$. In other words the baryons should be at least 50% more skewed than in the standard case, while the dark matter cannot exceed 15%. It is interesting that in no case $S_3$ can be lower than 34/7 by more than a few percent.

The contour plots render graphically evident the predictive power of stationary dark energy: the contours are not degenerate one with another. A determination of any two quantities would be sufficient to fix $\Omega_m, w_\phi$ , that is $\beta, \mu$. Any third quantity would either reject or confirm the model.

### 5.2.4 Inverse power law

Here and below we will assume for the numerical integrations the inverse power law potential $V \sim \phi^{-n}$, which appears only in the background equations. For this potential the present equation of state is approximated by (3.18) during the tracking regime (which may or may not extend to the present epoch; in the latter case $w_\phi \to -1$). Integrating numerically Eqs. (5.13-5.14) we find a fit for $m$

$$m \approx \Omega_m^{0.56(1-1.73\beta^2)}\,, \tag{5.57}$$

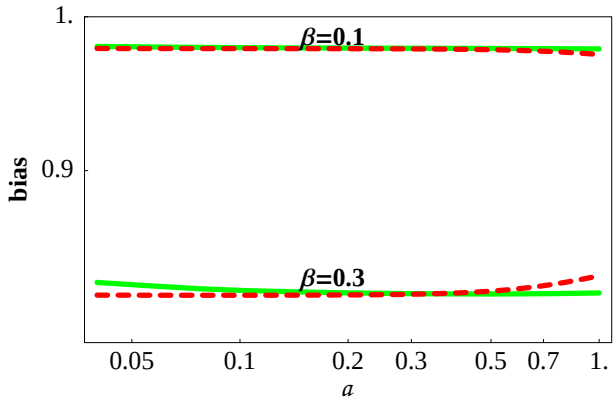


Figure 5.3: Plot of the bias as a function of the scale factor for two different values of the coupling. Solid curves: numerical function. Dashed curves: semianalytical function (Eq. (5.50)).

almost independently of $n$.

We proceed now to second order and go back to Eqs. (5.51-5.52), where for each component the second-order Fourier amplitude is $\delta^{(2)}(k,\alpha) = D_2(\alpha)\delta_k^{(2)}$. As it has been shown in Sec. 5.2.1, the dominant term in the skewness is

$$S_{3c} = 6\frac{D_{2c}}{D_1^2}\,, \quad S_{3b} = 6\frac{D_{2b}}{b^2 D_1^2}\,.$$

It turns out that we can obtain as the leading non-trivial term

$$\frac{S_{3b}}{S_{3c}} = \frac{b^{(2)}}{b^2} \approx 1 + \beta^2 \left[\frac{34\Omega_m}{28m^2 + 57\Omega_m}\right]\,. \tag{5.58}$$

(here we employed the fact that $S_{3c} \approx 34/7$, see below). Substituting (5.57) it appears that $S_{3b}$ is almost independent of the potential slope $n$ and, since, $m^2 \approx \Omega_m$, also almost independent of $\Omega_m$. The system (5.13-5.14-5.51-5.52), along with the background equations, constitute a complete set of differential equations for the unknowns $b, m, S_{3b}, S_{3c}$ as function of the cosmological parameters $w_\phi, \Omega_\phi, \beta$.

Each of the functions $b, m, S_{3b}, S_{3c}$ is in principle a test of the equivalence principle. However, $b$ and $S_{3c}$ require the detection of the large scale clustering of the dark matter component, while $m$, the clustering growth rate, requires accurate observations over an extended range of redshift and, consequently, a problematic removal of redshift dependent selection effects. On the other hand, $S_{3b}$ is an

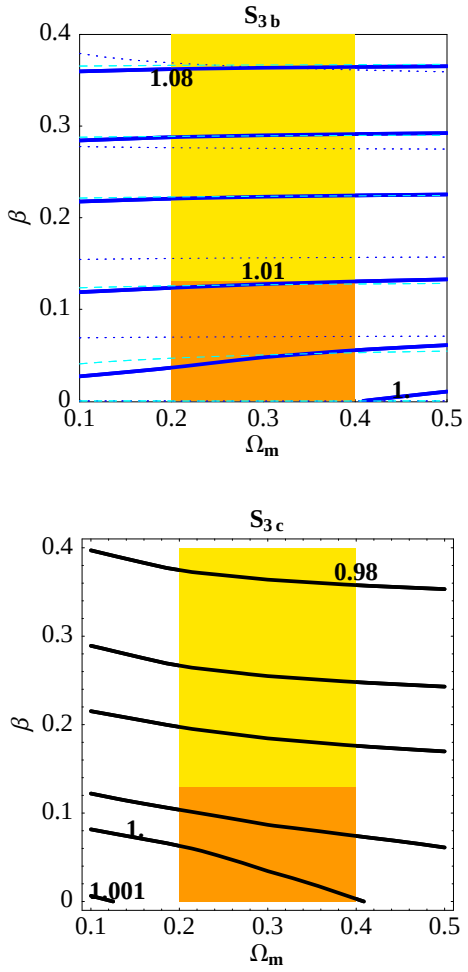


Figure 5.4: Contour plot of the observable quantities $S_{3b}\cdot(7/34), S_{3c}\cdot(7/34)$ calculated numerically as function of $\Omega_m, \beta$. For $S_{3b}$the lines correspond to the contour values $1., 1.002, 1.01, 1.03, 1.05, 1.08$, while for $S_{3c}$they are $1, 1.001, 0.999, 0.995, 0.99, 0.98$, both from bottom to top. The short-dashed curves in the plot $S_{3b}$ are the fit (5.59); the dotted curves the approximation (5.58). The rectangle marks the cosmological bounds on $\Omega_m, \beta$ .

efficient probe of the scalar interaction since it requires only observations of the baryon distribution at a fixed redshift.

We plot in Fig. 5.4 the numerical results as function of $\Omega_m$ and $\beta$ . As anticipated, we find that $S_{3c}$ is close to the standard value 34/7 in the whole parameter range while $S_{3b}$ deviates from 34/7 by more than 1% for $\beta > 0.1$, following the approximate fit

$$S_{3b} = \frac{34}{7}(1 + 0.6\beta^2)\Omega_m^{-0.0005\beta^{0.05}} \tag{5.59}$$

again almost independently of $\Omega_m$ and $n$ (in fact the last factor can be omitted). The analytical behavior (5.58) is relatively accurate (error on $S_{3b}$< 1%) only for $\beta < 0.2$.

In Bernardeau et al. (2002) the authors compiled an extensive list of present constraints on $\hat{S}_3$ from angular and redshift galaxy catalogs. Although most experiments quote values of $\hat{S}_3$ with errors of 5-10%, the results are clearly not compatible with each other. Same scatter, if not larger, can be seen in angular catalogs. This clearly points to the presence of systematic errors, that are likely to reside in sampling and finite volume effects and redshift distortions, so it is certainly premature to perform a direct comparison with data. Future analyses from larger redshift surveys like SDSS (see e.g. preliminary results in Gaztañaga (2002); Szapudi et al. (2002)) or 2DF survey (Croton et al. 2004) promise to measure $\hat{S}_3$ with a precision of less than 10% and perhaps down to 1%.

It is however to be stressed that our calculations refer to the properties of baryons, while observations deal with light, i.e. with the fraction of baryons that collapsed in sufficiently bright galaxies. The relation between the two populations is not well known, although at large scales, where hydrodinamical effects and strong non-linearities are smeared out, one does not expect significant segregation. To ascetrain this relation it is necessary to perform N-body simulations with broken equivalence, as we will see in the next Chapter.

On the other hand it is also possible to study objects that seem to trace with more accuracy (or at least in a simpler way) the underlying baryon content, such as Lyman-$\alpha$ clouds (Croft et al. 1998). Errors less than 10% in the bispectrum

at large scales are predicted in Mandelbaum et al. (2003) using a Lyman-$\alpha$ forest that simulate SDSS data.

Although models with non-Gaussian initial conditions, non-gravitational effects or non standard Friedmann equation predict $S_2 \neq 34/7$ (Multamäki et al. (2003), Bernardeau et al. (2002), Lue et al. (2004)), they also predict a specific time and/or scale dependence that make them distinguishable, at least in principle, from a scalar interaction. Further information can be gained by the full bispectrum $B(k_1, k_2) =< \delta_{k_1}\delta_{k_2}\delta_{-k_1}\delta_{-k_2} >$, rather than the integrated skewness. In Scoccimarro et al. (2004) it has been shown that the scale dependence of the bispectrum may be of great help in constraining primordial non-Gaussianity. Forecoming large scale skewness data offer therefore the exciting opportunity to test the interaction properties of a dark scalar field in a realm inaccessible to laboratory experiments.

# Chapter 6

# Beyond linearity: a numerical approach

The theoretical scenario that describes the scructure formation in the Universe is based on gravitational instability: once an initial small density fluctuation creates a local gravitational potential, it then accreates matter and consequently increases its gravitational field eventually leading the structure to collapse and virialize (Padmanabhan 1993). At the beginning, while the Universe is expanding, perturbations are so small ($\delta \ll 1$) that their growth is still influenced by the expansion and their evolution can be treated with an analytical approach in linear theory. On the other hand, when fluctuations enter a strongly non-linear regime (i.e. $\delta \gg 1$) the only way to follow completely their evolution is via

numerical techniques. In N-body codes, given the initial conditions in a specific cosmological model, the particle trajectories are followed applying the well known physical laws from the early Universe till today. These N-body codes are very time consuming, due to the high number of particles employed in order to have a good resolution. Up to date however, several techinques have been developed in order to reduce the computational load without loss of precision.
In this Chapter we will briefly review the properties of N-body, analysing then the application to cosmological model in which dark energy is present and coupled to dark matter (Macciò et al. 2004).

## 6.1 N-body codes

There are many different numerical techiques to follow the evolution of a system composed by many particles (see for more general discussion Bertschinger (1998)). Most of the methods for cosmological applications can be classified in three main basic categories: *i*) the Particle-Particle (PP) codes; *ii*) the Particle-Mesh (PM) codes; *iii*) the TREE codes.

*i*) The Particle-Particle approach is the simplest way to compute the forse among particles: the force experimented by one particle is obtained by a direct summation of the force due to all the other $N$ particles:

$$F_i = \sum_{j=1,N} -\frac{G m_i m_j (\mathbf{x_i} - \mathbf{x_j})}{(\epsilon^{\mathbf{2}} + |\mathbf{x_i} - \mathbf{x_j}|^{\mathbf{2}})^{\mathbf{3/2}}}, \tag{6.1}$$

where $\epsilon$ is the softening parameter used to suppress forces on scales $< \epsilon$. Since the number of operation to be done at each step is $\mathcal{O}(N^2)$, this approach becomes prohibitively expensive once $N > 10^4$.

*ii*) The Particle-Mesh method uses a mesh to compute density, and to solve the associated Poisson equation

$$\nabla^2 \psi = 4\pi G a^2 (\rho(\mathbf{x}, \mathbf{t}) - < \rho_{\mathbf{m}}(\mathbf{t}) >), \tag{6.2}$$

usually via a FFT (Fast Fourier Trasform) algorithm. The main advantages of this method are: it is faster than PP, because the number of operations is linked with the number of cells in the mesh ($N_g$), and it scales as $N_g \log_2 N_g$; it permits to use a large number of particles. the problem is that the grid method is only able to produce reliable inter particle forces down to a minimum of at least two grid cells.

*iii*) In TREE codes particles are devided in groups and subgroups ina a sort of tree-like hierarchy. The basic idea to compute the force on a particle is to treat the groups of particles far from it as a single big particle with position in the baricenter of the group and total mass equal to the sum of the masses of all the particles belonging to the group (Barnes (1986), Hernquist (1987)). This is the most flexible code, but it is more time expensive than a PM.

In addition to them there are also codes that use a combination of such methods as the AP$^3$M code (e.g. Couchman (1991)) which is a combination of PP and PM codes, or the ART code (Kravtsov et al. 1997).

### 6.1.1 The ART code

Multigrid methods were introduced long ago, but only recently they started to show a potential to produce real results. An example of a fully adaptive multigrid code is the Adaptative Refinement Tree code (ART). The ART code starts with a uniform grid, which covers the whole computational box. This grid defines the lowest (zeroth) level of resolution of the simulation. The standard Particles-Mesh algorithms are used to compute density and gravitational potential on the zeroth-level mesh. The ART code reaches high force resolution by refining all high density regions using an automated refinement algorithm. The refinements are recursive: the refined regions can also be refined, each subsequent refinement having half of the previous level's cell size. This creates a hierarchy of refinement meshes of different resolution, size, and geometry covering regions of interest.

Because each individual cubic cell can be refined, the shape of the refinement mesh can be arbitrary and match effectively the geometry of the region of interest.
The criterion for refinement is the local density of particles: if the number of particles in a mesh cell (as estimated by the Cloud-in-Cell method) exceeds the level $n_{tresh}$, the cell is split ("refined") into 8 cells of the next refinement level. For the zero's level it is $n_{tresh} = 2$. For the higher levels it is set to $n_{tresh} = 4$. The Poisson equation on the hierarchy of meshes is solved first on the base grid using FFT technique and then on the subsequent refinement levels. There is no particle-particle direct summation in the ART code and the actual force resolution is equal to $\sim 2$ cells of the finest refinement mesh covering a particular region. The code uses the expansion parameter $a$ as the time variable. During the integration, spatial refinement is accompanied by temporal refinement. Namely, each level of refinement, $l$, is integrated with its own time step $\Delta a_l = \Delta a_0/2^l$, where $\Delta a_0 = 3\times 10^{-3}$ is the global time step of the zeroth refinement level. When a particle moves from one level to another, the time step changes and its position and velocity are interpolated to appropriate time moments. This variable time stepping is very important for the accuracy of the results. As the force resolution increases, more steps are needed to integrate the trajectoriea accurately.
The code adopt a standard second order leapfrog integration scheme of advancing particles to the next time step. For a step $n$, corresponding to time step $a_n = a_{init} + n\Delta a$, the momenta and position of particles are updated as follows:

$$\mathbf{p}_{n+\frac{1}{2}} = \mathbf{p}_{n-\frac{1}{2}} - g_{model}\nabla\psi\Delta a \tag{6.3}$$

$$\mathbf{x}_{n+1} = \mathbf{x}_n - g_{model}\frac{\mathbf{v}_{n+\frac{1}{2}}}{\mathbf{a}^2_{n+\frac{1}{2}}}\Delta a, \tag{6.4}$$

where

$$g_{model} = \frac{dt}{da} = \left(aH_0\sqrt{\frac{\Omega_{m0}}{a^3\Omega_m(a)}}\right)^{-1} \tag{6.5}$$

is a function of the background cosmological model.
Here the indices $n$, $n+1$ and $n\pm\frac{1}{2}$ refer to quantities evaluated at $a_n$, $a_{n+1}$ and $a_n \pm \Delta a/2$ respectively. Extended tests of the code and comparison with

other numerical N-body codes can be found in Kravtsov (1999) and Knebe et al. (2000).

## 6.2 N-body with dark energy

Again, we focus on a cosmological model where the dark energy component is represented by a scalar field coupled to dark matter and self–interacting through a Ratra–Peebles potential (3.16).

Let us outline soon that our non–linear treatment sets precise constraints to coupled dark energy parameters. A wide parameter space however remains where, apparently, these models fit LSS data as well as those with (uncoupled) dynamical dark energy, although coupled dark energy, with Ratra & Peebles potential, allows no improvement of such fit. The motivations for coupled dark energy (see Sec. 2.3) however remain and, altogether, the non–linear test is successfully passed. N–body simulations of models with (uncoupled) dynamical dark energy were recently performed (Mainini et al. (2003), Linder (2003), Klypin et al. (2003)). Here we follow the same pattern of Klypin et al. (2003) and use the program ART providing, first of all, the fair dependence of the matter density parameter $\Omega_m$ on the scale factor $a$. To our knowledge, this is the first time an $N$-body simulation with species-dependent scalar gravity is carried out. Our conclusions are based on simulations of a variety of models with different Ratra & Peebles slopes $n$ and coupling parameters $\beta$. Let us list them soon: first of all, we test two $\alpha$ slopes: 0.143 and 2. The latter value approaches the greatest value for which agreement with CMB observations is granted (see Chapter 4). This is the range of Ratra & Peebles models which are most distant from ΛCDM. We explored also a wide set of $\beta$ couplings, ranging from 0.05 to 0.25. All simulations were performed starting from the same random numbers and, for the sake of comparison, we also run a ΛCDM simulation starting from such random numbers. The other parameters were set to values chosen in agreement with WMAP CMB experiment (Bennett et al. 2003): $\Omega_c h^2 = 0.15$, $\Omega_b h^2 = 0.01$, $h = 0.7$ ($\Omega_c$ is the (cold) dark matter density parameter). All models are normalized so that

$\sigma_8 = 0.75$ today, to match both CMB data and the observed cluster abundance (Schuecker et al. 2002). Further details on the simulation performed are listed in Table 6.1.

| Model | $n$ | $\beta$ | Box size ($h^{-1}$Mpc) | # of particle | Mass res. ($h^{-1}M_\odot$) | Force res. ($h^{-1}$kpc) |
|---|---|---|---|---|---|---|
| $RP_1$ | 0.143 | 0.05 | 80 | $128^3$ | $2.0\times10^{10}$ | 5 |
| $RP_2$ | 0.143 | 0.10 | 80 | $128^3$ | $2.0\times10^{10}$ | 5 |
| $RP_3$ | 0.143 | 0.15 | 80 | $128^3$ | $2.0\times10^{10}$ | 5 |
| $RP_4$ | 0.143 | 0.2 | 80 | $128^3$ | $2.0\times10^{10}$ | 1.2 |
| $RP_5$ | 0.143 | 0.25 | 80 | $128^3$ | $2.0\times10^{10}$ | 1.2 |
| $RP_6$ | 2.0 | 0.15 | 80 | $128^3$ | $2.0\times10^{10}$ | 5 |
| $\Lambda$CDM | 0 | 0 | 80 | $128^3$ | $2.0\times10^{10}$ | 5 |

Table 6.1

For all these models we also run an high-resolution simulation of a single halo, with a mass resolution of $2.5 \times 10^9\ h^{-1}M_\odot$ and a force resoltuion of $1.2\ h^{-1}$kpc.

## 6.3 Particle interactions

The N-body code was modified according to the coupled dark energy model. In this Section we analyse how the equation of motions are differently changed by the presence of coupled dark energy respectively for baryons and dark matter.
From Eqs. (5.13-5.14), we can derive the acceleration of a single dark matter or baryon particle (mass $m_{c,b}$), assuming that it lays in the empty space, at distance $r$ from the origin, where either a dark matter particle of mass $M_c$ or a baryon particle of mass $M_b$ are set.
In fact, owing to Eq. (4.8) and assuming that the density of the particle is much

larger than the background density, it shall be

$$\begin{aligned}\Omega_c\delta^c &= \frac{\rho_{M_c}-\rho_c}{\rho_{crit}} = \frac{8\pi G e^{-\sqrt{\frac{16\pi G}{3}}\beta\phi} M_c\delta(0)}{3\mathcal{H}^2 a}\\ \Omega_b\delta^b &= \frac{\rho_{M_b}-\rho_b}{\rho_{crit}} = \frac{8\pi G\delta(0)}{3\mathcal{H}^2 a},\end{aligned}$$

$\delta$ being the Dirac distribution. Then, reminding that the divergence $\nabla_i v_i^{c,b} = \theta^{c,b}H$, and using the ordinary (not conformal) time variable, instead of $\alpha$, eq. (5.15) yields

$$\nabla_i \dot{v_i^c} = -H(1-2\beta X)\nabla_i v_i^c - \frac{4\pi G^* M_c e^{-\sqrt{\frac{16\pi G}{3}}\beta\phi}\delta(0)}{a^2} - \frac{4\pi G M_b\delta(0)}{a^2}, \qquad (6.6)$$

where dots yield differentiation with respect to ordinary time and

$$G^* = G(1+\frac{4}{3}\beta^2) \qquad (6.7)$$

is the renormalised Newton constant for dark matter particles. We can integrate this equation, taking into account that the acceleration is radial, as the attracting particle lays in the origin. It will then be

$$\int d^3x\,\nabla\cdot\dot{\mathbf{v}} = 4\pi\int dx\frac{d(x^2\dot{v})}{dx} = 4\pi x^2\dot{v},$$

$\dot{v}$ being the modulus of the (radial) acceleration (in the second term $x = |\mathbf{x}|$). Accordingly, for a dark matter particle, the desired expression of the radial acceleration reads

$$\dot{v}^c = -(1-2\beta X)H\mathbf{v}^c\cdot\mathbf{n} - \frac{G^* M_c e^{-\sqrt{\frac{16\pi G}{3}}\beta\phi}}{r^2} - \frac{GM_b}{r^2}, \qquad (6.8)$$

($\mathbf{n}$ is a unit vector in the radial direction; $r = ax$) which has various peculiarities and ought to be suitably commented. To this aim it is important to compare it with the radial acceleration

$$\dot{v}^b = -H\mathbf{v}^b\cdot\mathbf{n} - \frac{GM_c e^{-\sqrt{\frac{16\pi G}{3}}\beta\phi}}{r^2} - \frac{GM_b}{r^2} \qquad (6.9)$$

of a baryon particle. In the expression (6.8), notice first the velocity term. This is a peculiar acceleration that exist even in the absence of particles displaying their

attraction; its presence means that dark matter is not expanding in a comoving way, due to the extra gravity it feels. Accordingly, its particles do not follow geodesics, because their mass changes in time, and their ordinary (not comoving) linear momentum obeys the equation

$$\dot{p_c} = -\frac{G^* M_c e^{-\sqrt{\frac{16\pi G}{3}}\beta\phi}}{r^2} - \frac{GM_b}{r^2}.$$

Baryon particles, instead, safely follow geodesics, although feeling that dark matter particle masses are varying.

Let us conclude this Section by summarising its specific findings: (i) The mass assigned to dark matter particles does vary in time, being $m_c = m_o e^{-\sqrt{\frac{16\pi G}{3}}\beta\phi}$, while baryon particles do keep a constant mass. (ii) When interacting between them, dark matter particles feel an effective gravitational constant $G^* = G(1 + 4\beta^2/3)$; any other particle–particle interaction occurs with the ordinary newtonian interaction constant $G$.

## 6.4 Methods

Let us now describe the three main modifications we made to handle coupled dark energy. A first step amounts to distinguish between baryons and dark matter particles, which feel different gravitational forces. Therefore, the potential on the grid is to be calculated twice, so to fix the different forces that baryon and dark matter particles feel. All particles act on baryons through the usual gravitational constant $G$, which sets also the action of baryons on dark matter particles. Dark matter particles instead, act on dark matter particles through a different interaction constant $G^* = G(1 + 4\beta^2/3)$. The gravitational force is then computed through the usual FFT approach.

A second step amounts to take into account that the effective mass of dark matter particles is time varying. Aside of the acceleration due to gravitation, each dark matter particle will therefore undergo an extra acceleration $2\beta X$. Besides of these two changes, peculiar of coupled dark energy models, we ought to take into account the right relation between $a$ and $t$, as shown in Eq. (6.5), where

$g_{model}(a) = dt/da$ is given. By solving the background equations, in a suitable file we provide $g_{model}(a)$ in $\simeq 200$ scale factor values $a_i$, that we than interpolate. The models listed in Table 6.1 were first simulated in a $80h^{-1}$Mpc box. We then selected the same halo in all simulations and magnified it. The low–resolution simulation, performed with a force resolution of $15\,h^{-1}$ Mpc and a mass resolution $\simeq 2 \cdot 10^{10}\,h^{-1}M_{\odot}$, allowed us to evaluate the halo mass function. The high–resolution simulation, performed with a force resolution of $\simeq 1.2\,h^{-1}$kpc and a mass resolution of $2.54 \cdot 10^{9}h^{-1}M_{\odot}$, magnified a sphere with a radius of $5\,h^{-1}$Mpc, centered on the halo, allowing us to compare halo profiles down to a radius $\simeq 5\,h^{-1}$kpc.

Besides of the above points, we could also test the non–linear evolution of the *bias* between the amplitudes of inhomogeneities in baryons and dark matter. Such bias is one of the most peculiar features of coupled dark energy models and we shall describe how non–linearity modifies it.

## 6.5 Mass function

We identify halos in simulations halos by using a Spherical Overdensity (SO) algorithm, that we shall now describe in more detail. As first step, candidate halos are located by a Friend of Friend (FOF) procedure, with linking length $\lambda = U \times d$ ($d$ is the average particle separation) and keeping groups with more than $N_f$ particles ($U$ and $N_f$ fixed herebelow). We then perform two operations: (i) we find the point, $C_W$, where the gravitational potential, due to the group of particle, has a minimum; (ii) we determine the radius $\overline{r}$ of a sphere, centered in $C_W$, where the density contrast is $\Delta_v$ (we use the virial density contrast found in the absence of dark–dark coupling (Mainini et al. 2003). Taking all particles within $\overline{r}$ we perform again the operations (i) and (ii). The procedure is iterated until we converge onto a stable particle set. The set is discarded if, at some stage, we have less than $N_f$ particles. If a particle is a potential member of two groups it is assigned to the more massive one. In this work we use $U = 0.2$ and take $N_f$ so to have a mass threshold $5.0 \cdot 10^{12}h^{-1}\mathrm{M}_{\odot}$.

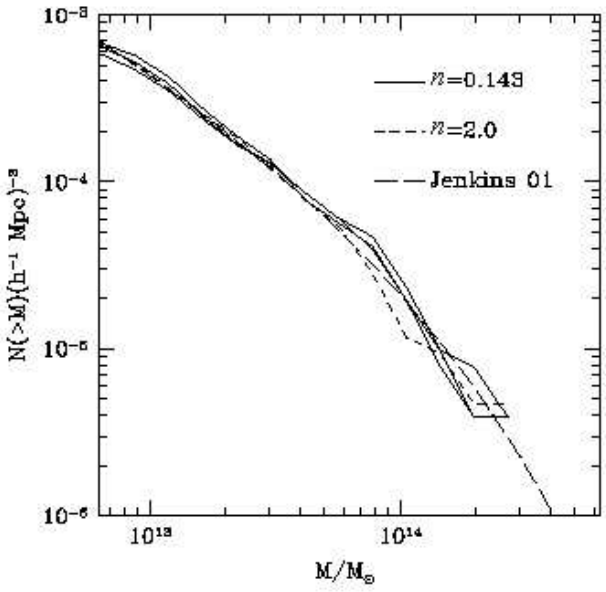


Figure 6.1: Mass function at $z = 0$ for $n = 2$ and $n = 0.143$. For $n = 0.143$ we report three curves, for different values of $\beta$. They are all practically indistinguishable and are well fitted the approximation of Jenkins et al. (2001).

Fig. 6.1 shows the mass function for isolated halos for models with different values of $n$ and $\beta$. Let us remind that the simulations have the same initial phases and the same value $\sigma_8 = 0.75$. Thus, the differences between models are only due to different couplings or $w(t)$. Remarkably, at $z = 0$ the mass-functions are practically indistinguishable: a mass-function has no "memory" of the past evolution. The mass-function obtained in this way is well fitted by the approximation provided by Jenkins et al. (2001) for ΛCDM models (long dashed line in Fig. 6.1).

## 6.6 Linear and non–linear bias

From eqs. (5.13), the linear evolution of the density perturbations can be easily worked out (in some cases (Amendola 1999) this can be done analytically). In Fig. 6.2 we show $\delta^{c,b}$ as a function of the scale factor $a$. As a consequence of

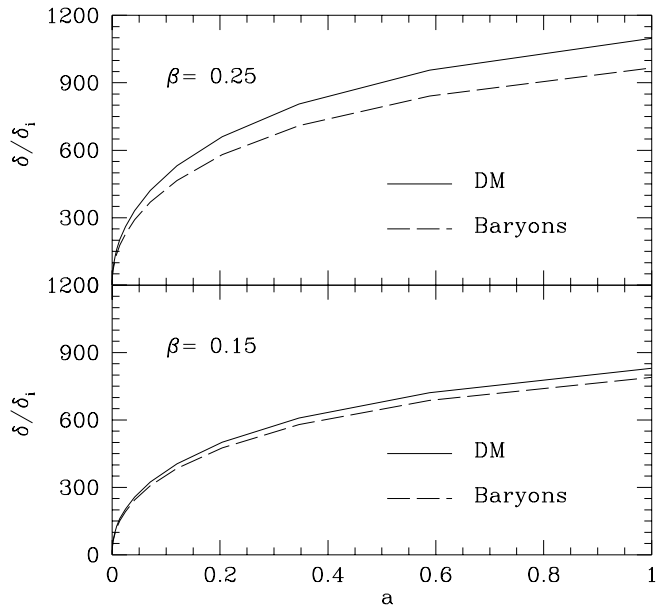


Figure 6.2: dark matter and baryons linear perturbation growth for two different values of $\beta$. The dependence on $n$ is weak and could not be appreciated in this plot.

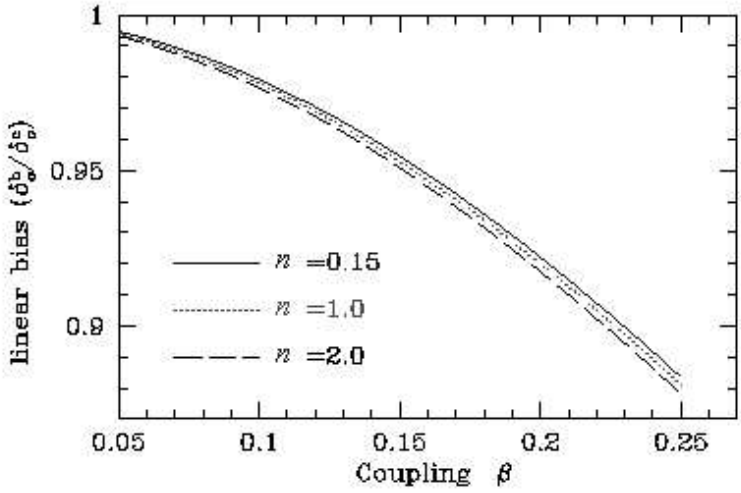


Figure 6.3: Linear bias as a function of $\beta$ for three values of $n$. Notice the very weak dependence on $n$.

these dynamical equations, $\delta^c$ develops a bias with respect to $\delta^b$, due to the extra gravity felt by dark matter. At the present epoch, this bias, found in the linear theory, is well fitted by the following empirical expression:

$$b(n,\beta) = \frac{\delta_o^b}{\delta_o^c} = \frac{1}{1 + 0.015\, n\beta + 2.1\, \beta^2}. \tag{6.10}$$

Both this expression and Fig. 6.3 show that the bias $b$ depends on $\beta$, while its dependence on $n$ is very weak.

Using the high resolution clusters we can test the behavior of the bias in the highly non–linear regime. To do so, we define the integrated bias $B$ as:

$$B(< r) = \frac{\rho_b(< r) - \hat{\rho}_b}{\hat{\rho}_b} \cdot \frac{\hat{\rho}_c}{\rho_c(< r) - \hat{\rho}_c},$$

where $\rho_c(< r)$ and $\rho_b(< r)$ are calculated inside a radius $r$ from the halo center and we use a hat ( $\hat{}$ ) to denote average densities. In order to avoid problems with force resolution, the central zone ($r < 10h^{-1}$kpc) of the halo is not used. In Fig. 6.4 we show $B(< r)$ for the same halo, in cosmologies characterized by different coupling parameters $\beta$, keeping all other parameters equal. Fig. 6.4 shows that non–linearity significantly enhances the expected bias; however, at larges scales, we recover the theoretical linear value, as provided by eq. (6.10). The scale dependence of bias can also be appreciated from Fig. 6.5, where power spectra for baryons and dark matter, worked out from simulations at $z = 0$, are shown.

## 6.7 Density profiles

Let us remind again that all simulations are started from the same random numbers. Therefore, it comes as no surprise that they yield similar world pictures. In the ΛCDM simulation, we selected a halo, whose *virial* radius $r_v = 812\, h^{-1}$kpc encloses a mass $M_v = 6.45 \cdot 10^{13} h^{-1} M_\odot$. Similar halos, located in the same place, are set in all other models considered. We then run new simulations of all models in Table 6.1, magnifying the region centered on this halo. To do so, short waves were first added to the initial perturbation spectrum in all simulations.

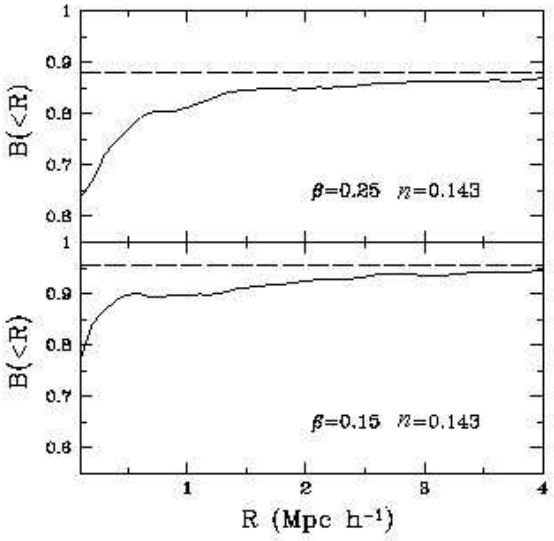


Figure 6.4: Behaviour of the integrated bias $B$ for $\beta = 0.15$ and for $\beta = 0.25$. Notice that $B$ tends to the predicted linear bias (dashed horizontal lines) at large scales.

In ΛCDM, the halo profile is accurately fitted by a NFW expression (Navarro, Frenk, & White 1997):

$$\frac{\rho(r)}{\rho_{cr}} = \frac{\delta^*}{\frac{r}{r_s}\left(1+\frac{r}{r_s}\right)^2}$$

with a scale radius $r_s = 0.249\,h^{-1}$Mpc (here $\rho_{cr}$ is the critical density and $\delta^*$ is a parameter which sets the halo density contrast).

When the same halo is magnified in coupled dark energy models, we find model dependent behaviors towards the halo center. The essential restrictions to coupled dark energy models, arising from the non–linear treatment, derive from these behaviors. However, in spite of such model dependence in the central areas, the outer parts of halos ($R > 100\,h^{-1}$Kpc) show discrepancies that, from $100\,h^{-1}$kpc to $700h^{-1}$kpc, never exceed $\sim 10\,\%$.

Let us now discuss the substantial model dependence found in the central region ($R < 100\,h^{-1}$kpc). It was already known that halos are denser in dynamical dark energy than in ΛCDM (Klypin et al. 2003), although the density enhancement is fairly small and hardly exceeds $\sim 40\,\%$. Higher density means smaller $r_s$. The

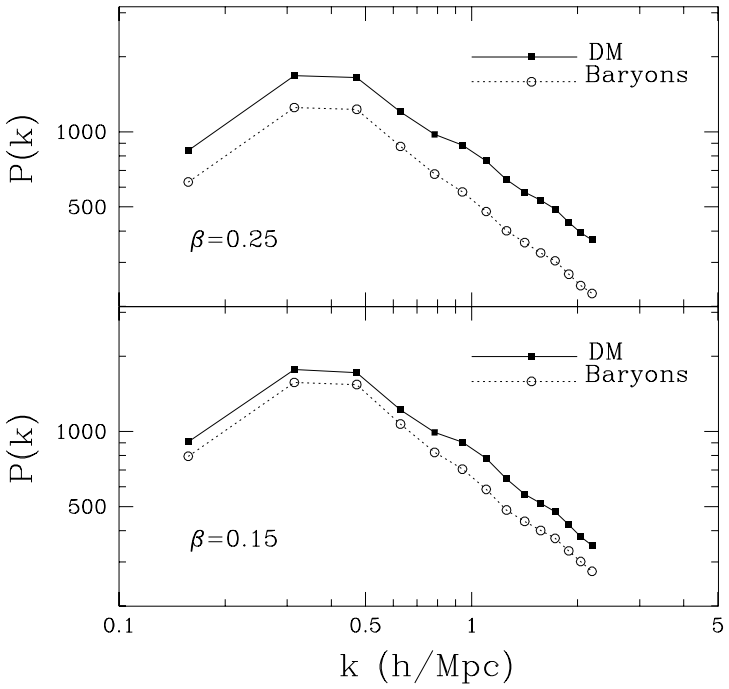


Figure 6.5: Power spectra for dark matter and baryon particles evaluated from the simulations averaging over 60 random observers. The increase of the bias at small scales appears clearly.

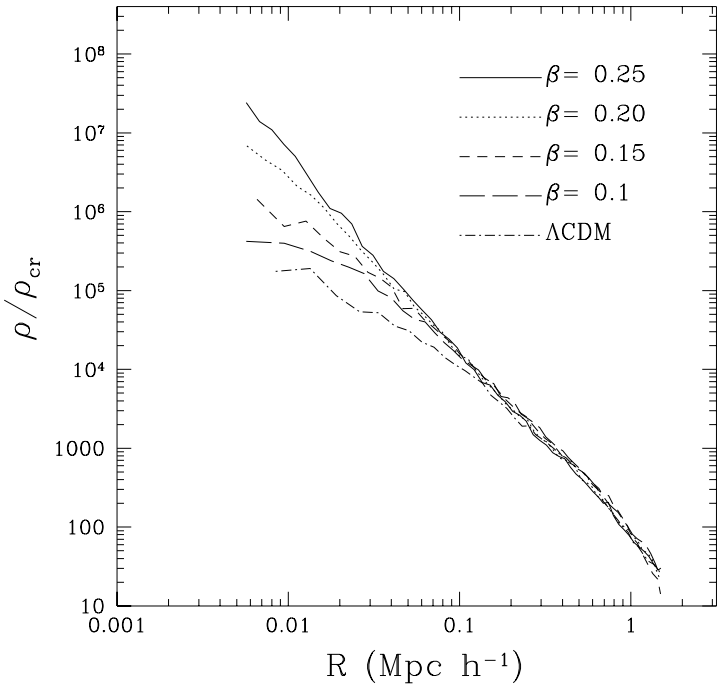


Figure 6.6: Dark matter density profile for four different coupling values and for ΛCDM.

coupled dark energy simulations we perfomed show that the dark–dark coupling tends to enhance such effect (cf. Fig. 6.10-6.11). In Fig. 6.5 we overlap the profiles of the dark matter components of all our models, starting from ΛCDM (lower curve), up to a Ratra & Peebles model with coupling parameter $\beta = 0.25$ (upper curve). The values of $r_s$ change from $\simeq 0.25\,h^{-1}$Mpc (ΛCDM) to $\simeq 0.022\,h^{-1}$Mpc ($\beta = 0.25$). The dependence of $r_s$ on $\beta$ is plotted in Fig. 6.7.

In order to make sure that this effect was not related to some peculiarity of the halo selected, we magnified two other halos of a simulation with $\beta = 0.25$. Here we found even lower values for the scale radius $r_s$ ($0.0105\,h^{-1}$Mpc and $0.0103\,h^{-1}$Mpc respectively).

As a matter of fact, the profiles found $\beta = 0.25$ or 0.2 can be fitted by a single power law:

$$\frac{\rho(r)}{\rho_{cr}} \propto r^{\gamma}$$

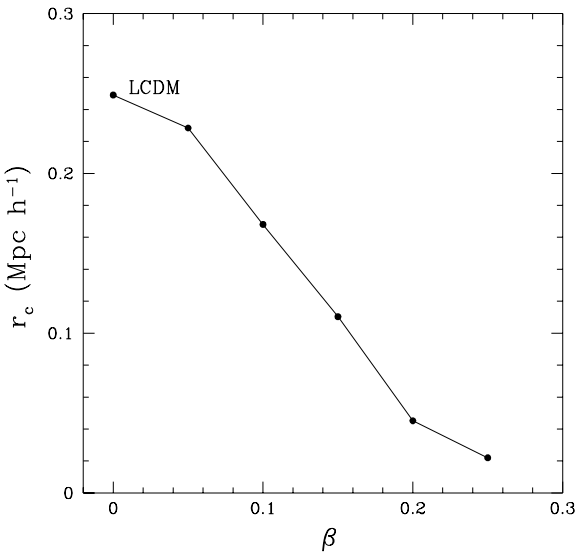


Figure 6.7: Scale radius of a NFW profile as a function of the coupling parameter $\beta$.

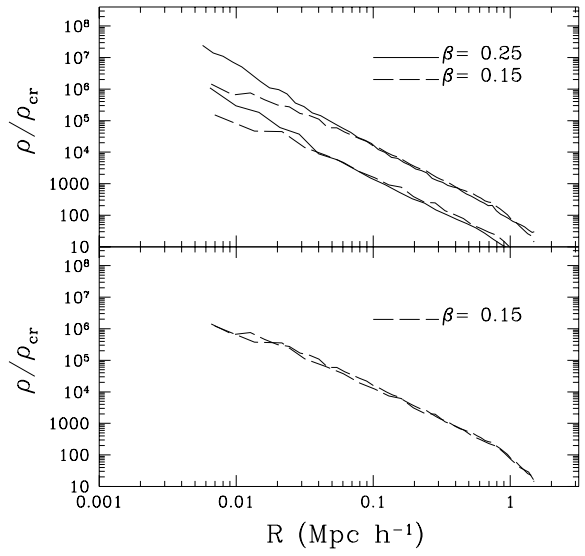


Figure 6.8: Upper panel: dark matter and baryons density profiles (respectively upper curve and lower curve) for $\beta = 0.15$ and for $\beta = 0.25$. Lower panel: once rescaled taking into account the different values $\Omega_b$ and $\Omega_c$, there is no discrepancy between dark matter and baryons.

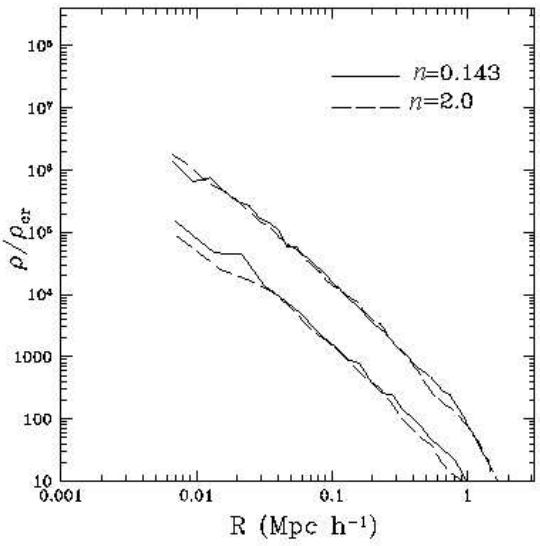


Figure 6.9: dark matter and baryons density profiles for $n = 2.$ and $n = 0.143$ (here $\beta = 0.15$).

in the whole dynamical range, i.e., from $r = 1.0h^{-1}$Mpc down to $r = 0.005h^{-1}$Mpc (resolution limit), with a value of $\gamma \simeq -2.30$.

An analysis of Fig. 6.7 shows that, only for $\beta$ as low as $\simeq 0.1$, $r_s$ attains half the value for ΛCDM. Accordingly, we may consider viable coupled Ratra & Peebles models only with $\beta < 0.1$.

Simulations distinguish baryons from dark matter particles, as already discussed above. This allows us to draw separate density profiles. They are shown in Fig. 6.8, for two different coupled dark energy models (upper panel). No apparent discrepancy between dark matter and baryon profiles can be seen: they overlap fairly well, once we rescale them taking into account the different values of $\Omega_b$ and $\Omega_c$ (Fig 6.8 lower panel).

In Fig. 6.9 we compare the profiles of the same halo, with two different values of $n$ (2.0 and 0.143), but with the same coupling ($\beta = 0.15$). The profiles overlap very well both for dark matter particles (upper curves) and for baryons (lower curves). We conclude that the slope of profiles depends very weekly on $n$.

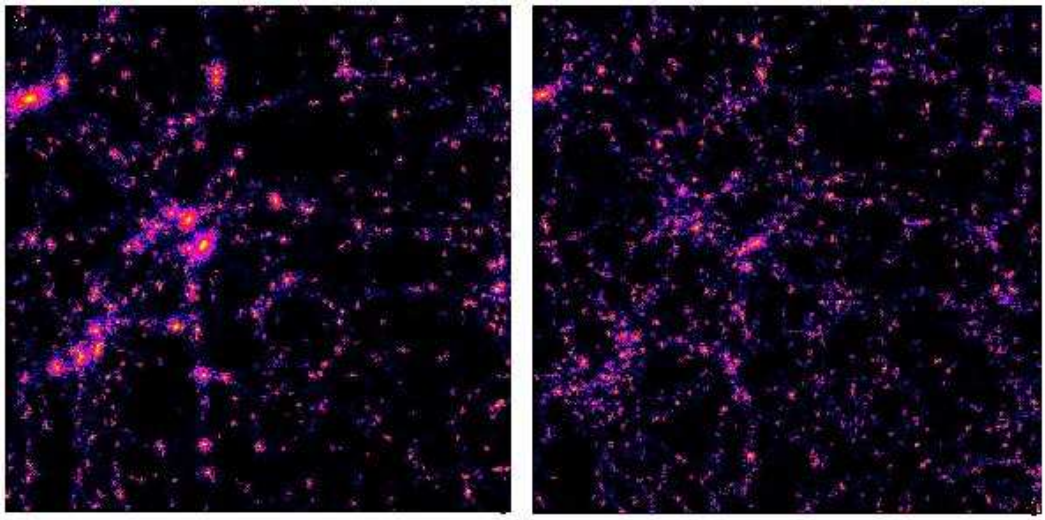

Figure 6.10: Map of the whole simulated box for a ΛCDM model and a model with $\beta = 0.25$.

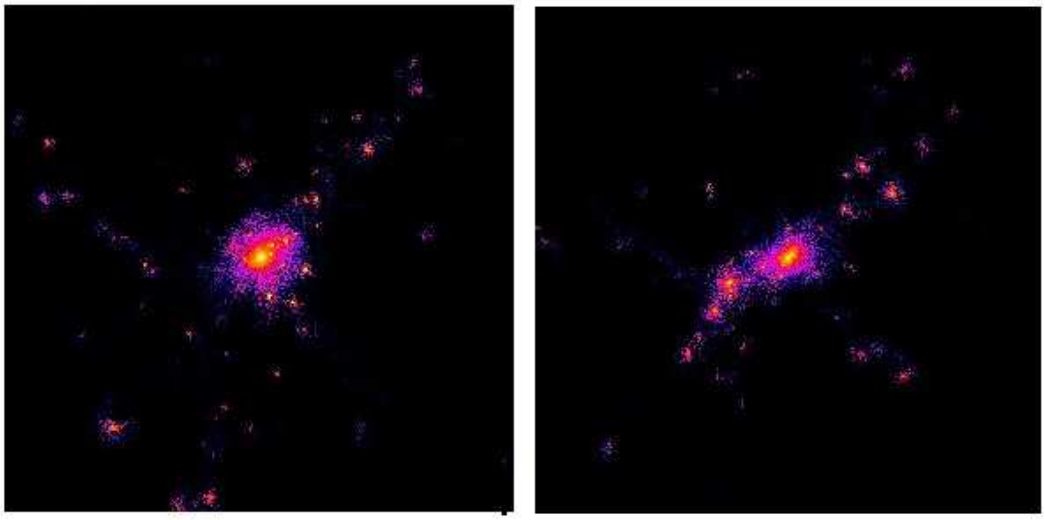

Figure 6.11: Simulation of a single cluster in models with two different values of $\beta$, respectively $\beta = 0.15, 0.25$.

# Chapter 7

# Comments and prospects

Cosmological observations probe the nature of dark energy. As we have seen in the previous Chapters, the anisotropy spectrum of the CMB, the shape of matter power spectrum and the distance-redshift relation are possible sources of information and will help us to distinguish between the different models of dark energy.

The behaviour of small perturbations in a scalar field and its effect on CMB anisotropies and structure formation has been investigated. However, the behaviour of dark energy during the gravitational collapse into the highly non-linear regime is not well understood and currently under investigation. Usually it is assumed that there are no density fluctuations in the quintessence field on cluster scale and below. The assumption of neglecting the effects of matter perturbations on the evolution of dark energy (and its backreaction) at small scales is

indeed a good approximation when perturbations of the metric are very small. Neverthless, even if the field is not coupled, one should be careful when extrapolating this approximation to the highly non-linear regime. In this final Chapter we present as a conclusion the possibility to investigate this backreaction and the methodology that should be adopted.

## 7.1 Dark energy backreaction

The reasons to assume that dark energy is an homogeneous field throughout the universe which is not affected by structure formation on small scales are several. Let us resume them:

*i*) According to linear perturbation theory, the mass of the field is very small (the associated wavelength of the particle is of the order of Hubble radius) and, hence, it does not feel overdensities of the size of tenth of Mpc or smaller (Wang & Steinhardt 1998).

*ii*) The sound velocity associated to a scalar field perturbation inside the horizon is $c_s^2 = 1$ (equal to the light speed), which means homogeneity at scales smaller than the horizon.

*iii*) Since the mass of the scalar field fluctuations is proportional to the second derivative of the potential, if we want the scalar field to act as a dark energy component, we need the latter to be very small today in order to have an accelerated expansion.

In addition, it is worth saying that there is no experimental evidence of dark energy in clustered objects. In the linear regime of the small cosmological perturbations, it can be shown that during the matter dominated epoch perturbations in the scalar field are described by (Hwang & Noh 2001)

$$\delta\ddot{\phi} + 2H\delta\dot{\phi} + a^2V''\delta\phi = \dot{\phi}\delta_c, \tag{7.1}$$

where the metric was perturbed about a flat FRW metric. From Eq. (7.1) the effective Jeans length for linear perturbation of the scalar field is roughly given by

$$\lambda_j \sim 2\pi/\sqrt{V''} \tag{7.2}$$

which turns out to be of the order of the horizon size (Ma et al. 1999). However the source term $\dot{\phi}\delta_c$ implies that dark energy is not smoothly spread (Caldwell et al. 1998). And in spite of the perturbations in dark energy are present and grow only on scales about the horizon size and larger, the effects on the evolution of matter overdensities are indeed important and significant (Ferreira & Joyce 1998).

In the highly non-linear regime, locally the flat FRW metric is not a good approximation anymore to describe the geometry of overdense regions. It is natural to think that once a dark matter overdensity decouples from the background expansion and collapses, the field inside the cluster feels the gravitational potential inside the overdensity and its evolution will be different from the background evolution. The backreaction effects in the highly non-linear regime could influence the evolution of perturbations in dark energy considerably, which in turn influence the evolution of matter perturbation.

It has already been shown, using the analytical spherical collapse model, that some of the properties of the clustering, such as the critical density contrast or the virial radius, can be strongly affected by the backreaction mechanism (Mota & van de Bruck 2004). If it turns out that backreaction effects of metric and density perturbations in dark matter could influence perturbations of quintessence on small scales, this could significantly change our understanding of structure formation on galactic and cluster scales in models with dark energy. This is the reason why it is important to analyse the mechanism with numerical techniques, like N-body codes.

### 7.1.1 Methodology

Once a dark matter overdensity decouples and collapses the field evolution inside the cluster will generally be different from the background evolution. Since locally (near a collapsing object) the flat FRW is not a good approximation, one needs to perform the full relativistic equations in the *perturbed* newtonian metric (5.2). The equation of motion of the dark energy scalar field calculated in this metric results to be

$$\phi^{;\mu}_{;\mu} = V' \qquad \rightarrow \qquad \ddot{\phi} + 2H\dot{\phi} + V'a^2(1+2\psi) - \nabla^2\phi - 4\dot{\psi}\dot{\phi} = 0. \tag{7.3}$$

Considering Eq. (2.3) in the newtonian metric, the usual Poisson equation is modified in a way that

$$\nabla^2\psi = c\psi + g + 3H\dot{\psi}, \tag{7.4}$$

where $c$ and $g$ are two function of the scalar field, $c = H^2 - 8\pi G[\frac{1}{2}\dot{\phi}^2 - \frac{1}{2}(\nabla\phi)^2]$ and $g = 4\pi G a^2\delta\rho_c + 4\pi G[\frac{1}{2}\dot{\phi}^2 - \frac{1}{2}\dot{\phi_0}^2 - V(\phi_0)a^2 + V(\phi)a^2]$, and the subscript 0 denotes the homogeneous quantities.

Usually in Nbody simulations the Poisson equation is easily solved by a FFT method. In this case it is not convenient anymore due to the coupling between Eqs.(7.3-7.4) and to the fact that the new Poisson equation is a general elliptic equation with non-constant coefficients.

The best method to solve this equations, after discretising them, is to integrate them both in time and in space on a grid. For the time integration it is sufficient a simple second order Runge Kutta method. For the space integration one we used an iterative method on a grid of point. Since the accuracy of the result depends on the number of grid points and in N-body codes (like for example the PM codes) a big number of grid points is requested, the appropriate method is a Multigrid Relaxation Method. The idea is to start with a grid and restrict to coarser and coarser grids: in this way the relaxation scheme (black-red Gauss Seidel) is cheaper and has marginally better convergence rate. In fact, smooth error is made oscillatory on the coarser grid. The Multigrid Relaxation method is comparable to the rapid methods in execution speed. The prospect is now to

insert these new equations in a N-body code, like the PM code, and to follow the gravitational collapse (e.g. of a single cluster) to see if the local coupling between the matter density contrast and the quintessence field via the perturbation of the metric leads to different clustering properties.

## 7.2 Conclusions

From the theoretical standpoint the important questions to be ask of dark energy are: *i*) if $w = -1$; *ii*) whether dark energy interacts with the other components or not, and, in case, what kind of couplings can affect normal gravity.

If future observations do answer the first question affirmative then, in all likelyhood the cosmological constant is the vacuum energy, with no interactions, and one will need to review the cosmological constant problem again. On the other hand, if $w \neq -1$, or if the dark energy is shown to be time dependent, then the cosmological constant problem may need to be decoupled from the dark energy conundrum and searches for evolving dark energy models will need to be examined deeply in the light of developments both in cosmology and high energy physics. In either case the key to determining the properties of dark energy to great precision clearly lies with ongoing and future astrophysical experiments and observations.

Since the original discovery of an accelerating Universe the SNe Ia data base has grown considerably and data pertaining to $\sim 200$ supernovae are avaliable in the literature. Although sistematic effects such as luminosity evolution, dimming by extragalactic material (or brightening due to gravitational lensing) continue to be a cause of some concern, it is reassuring that recent observations of CMB and estimates of galaxy clustering in the 2dF and SDSS surveys, make a strong and independent case for dark energy.

It is of great importance that SNe observations continue to be supplemented by other investigations which are sensitive to the geometry of space and can be used as independent test of the dark energy hypothesis. The volume-redshift test, Sunyaev-Zeldovich surveys, the Alcock-Paczynski test, the angular size-redshift

test and gravitational lensing have all been suggested as possible probes of dark energy, and will doubtless enrich the theory vs observations debate in the near future. In addition, the proposed SNAP satellite which aims to measure light curves of $\sim$ 2000 SNe within a single year, should provide a big step forward in our understanding of type Ia supernovae and help determine the cosmological parameters to great precision (http://snap.lbl.gov/). However, there are still no solid proposals for standard candles visible at redshifts significantly higher than $z \simeq 1.5$. Future deep and wide redshift surveys will have the chance to explore the little known landscape at $z \simeq 1-3$ between the recent and early Universe. This is the epoch at which dark energy begins to impel its thrust to the expansion: it is therefore of extreme interest for cosmology in order to gain hold of reliable data on its evolution. The use of baryon oscillations in the matter power spectrum is on the contrary based on well-known phenomena that have already seen a spectacular validation in CMB observations. Moreover, it can provide a tomography of the Universe expansion from $z = 0$ down to $z \simeq 3.5$, virtually without loss of precision. We found that a $200^2$ survey with absolute redshift error $\delta z = 0.02$ can limit $w_0, w_1$ by 0.39 and 0.54, respectively, assuming $w_0 = -1$, $w_1 = 0$ as reference values. If the dark energy is modeled as a scalar field with inverse power-law potential $n$, the limits are $n < 0.26$ (spectrosopic redshift) and $n < 0.40$ (redshift error $\delta z = 0.02$), along with an estimation of $\Omega_{m0}$ to better than 3%. Inclusion of SNe data further reduce the errorbars due to the different direction of degeneracy.

However, so far the most precise cosmological measurements come from the WMAP experiment. We have seen that CMB observations are a powerful probe to constrain the properties of dark energy. In particular, since a dark matter-dark energy interaction would obviously escape any local gravity experiment, cosmological observations like the CMB are the *only* way to observe such a phenomenon. Since observations require the baryons to be decoupled from dark energy (or coupled much more weakly than dark matter), the search for a non-zero coupling $\beta$ is also a test of the equivalence principle. We found that current CMB data are capable to pu intersting bound to dark energy cosmological pa-

rameters, $w_\phi < -0.49$, $\Omega_\phi = 0.67 \pm 0.05$ and $|\beta| < 0.13$ (all limits to 95% C.L.), regardless of the potential. We have also shown in Amendola et al. (2003) that an experiment like the Planck mission can lower the upper bound to $\beta$ to 0.05, a limit comparable to the one imposed on baryon coupling by local gravity experiments.

After finding that coupled dark energy models are consistent with those observables whose behaviour can be predicted at the linear level, a test of their non-linear behaviour had to be carried on. An optimistic hope was that coupled dark energy models helped to solve some of the long standing contradictions between observations and theoretical or numerical predictions (Moore 1994). In particular one coud hope to find halo profiles whose shapes is not NFW (if this is still a problem) with a slope distribution closer to the observed ones for low surface brightness galaxies and spiral galaxies. From this point of view, coupled dark energy with inverse power-law potential leads to modest results. Very high coupling levels, intead of producing a flatter core, yield profiles still farther from observations. In all cases, the problem with concentration distribution is not solved. In spite of the lack of improvement for what conserns slopes, N-body simulations lead to really significant results. First of all, the parameter space for coupled dark energy models is restricted to couplings $\beta < 0.1$, however leaving a wide room for significant couplings. Apart of the question of profiles, the halo mass function has been tested and found consistent with other dark energy models and with observations. Its evolution has been predicted and can be tested against future data. From this point of view, therefore, coupled dark energy passed the non-linear test. Future observations of the skewness will improve this probe, testing better the equivalence principle.

A better understanding of the behaviour of the quintessence field in highly non-linear regions is needed before predictions of the spherical collapse model can be trusted. The field can influence the dynamics of the collapse at late times and thus changing predictions of the turnaround, virialization and collapse time. To better undertand the mechanism, the most accuarate way will be to analyse the effect via numerical techinques.

# Bibliography


Albrecht, A., Burgess, C. P., Ravndal, F., & Skordis, C. 2002, *Phys. Rev. D*, 65, 123507

Albrecht, A. & Skordis, C. 2000, *Phys. Rev. Lett.*, 84, 2076

Amendola, L. 1999, *Phys. Rev. D*, 60, 043501

Amendola, L. 2000, *Phys. Rev. D*, 62, 043511

Amendola, L. & Quercellini, C. 2003, *Phys. Rev. D*, 68, 023514

Amendola, L. & Quercellini, C. 2004, *Phys. Rev. Lett.*, 92, 181102

Amendola, L., Quercellini, C., & Giallongo, E. 2004, 69, 123516

Amendola, L., Quercellini, C., Tocchini-Valentini, D., & Pasqui, A. 2003, *ApJ Letters*, 583, L53

Anderson, J. D. & Williams, J. G. 2001, *Classical and Quantum Gravity*, 18, 2447

Armendariz-Picon, C., Mukhanov, V., & Steinhardt, P. J. 2000, *Phys. Rev. Lett.*, 85, 4438

Avelino, P. P., Shellard, E. P. S., Wu, J. H. P., & Allen, B. 1998, *ApJ Letters*, 507, L101

Baccigalupi, C., Balbi, A., Matarrese, S., Perrotta, F., & Vittorio, N. 2002, *Phys. Rev. D*, 65, 063520

Baccigalupi, C., Matarrese, S., & Perrotta, F. 2000, *Phys. Rev. D*, 62, 123510

Barnes, J. E. 1986, *Lecture Notes in Physics*, Berlin Springer Verlag, 267, 175

Bean, R. & Melchiorri, A. 2002, *Phys. Rev. D*, 65, 041302

Benabed, K. & Bernardeau, F. 2001, *Phys. Rev. D*, 64, 083501

Bennett, C. L., Banday, A. J., Gorski, K. M., Hinshaw, G., Jackson, P., Keegstra, P., Kogut, A., Smoot, G. F., Wilkinson, D. T., & Wright, E. L. 1996, *ApJ Letters*, 464, L1+

Bennett, C. L., Halpern, M., Hinshaw, G., Jarosik, N., Kogut, A., Limon, M., Meyer, S. S., Page, L., Spergel, D. N., Tucker, G. S., Wollack, E., Wright, E. L., Barnes, C., Greason, M. R., Hill, R. S., Komatsu, E., Nolta, M. R., Odegard, N., Peiris, H. V., Verde, L., & Weiland, J. L. 2003, *ApJ Supplement Series*, 148, 1

Benoît, A., Ade, P., Amblard, A., Ansari, R., Aubourg, É., Bargot, S., Bartlett, J. G., Bernard, J.-P., Bhatia, R. S., Blanchard, A., Bock, J. J., Boscaleri, A., Bouchet, F. R., Bourrachot, A., Camus, P., Couchot, F., de Bernardis, P., Delabrouille, J., Désert, F.-X., Doré, O., Douspis, M., Dumoulin, L., Dupac, X., Filliatre, P., Fosalba, P., Ganga, K., Gannaway, F., Gautier, B., Giard, M., Giraud-Héraud, Y., Gispert, R., Guglielmi, L., & coauthors, . 2003, *Astronomy & Astrophysics*, 399, L19

Bernardeau, F. 1994, *ApJ*, 433, 1

Bernardeau, F., Colombi, S., Gaztañaga, E., & Scoccimarro, R. 2002, *Physics Reports*, 367, 1

Bertschinger, E. 1998, *Annual Review of Astronomy and Astrophysics*, 36, 599

Billyard, A. P. & Coley, A. A. 2000, *Phys. Rev. D*, 61, 083503

Blake, C. & Glazebrook, K. 2003, *ApJ*, 594, 665

Bouchet, F. R., Juszkiewicz, R., Colombi, S., & Pellat, R. 1992, *ApJ Letters*, 394, L5

Brax, P. & Martin, J. 2000, *Phys. Rev. D*, 61, 103502

Brax, P., van de Bruck, C., Davis, A.-C., & Rhodes, C. S. 2003, *Phys. Rev. D*, 67, 023512

Caldwell, R. R., Dave, R., & Steinhardt, P. J. 1998, *APSS*, 261, 303

Calvão, M. O., de Mello Neto, J. R., & Waga, I. 2002a, *Phys. Rev. Lett.*, 88, 091302

Calvão, M. O., de Mello Neto, J. R. T., & Waga, I. 2002b, in Astronomical Society of the Pacific Conference Series, 127–+

Carroll, S. M. 1998, *Phys. Rev. Lett.*, 81, 3067

Casas, J. A., Garcia-Bellido, J., & Quiros, M. 1992, 9, 1371

Catelan, P. 1995, *Mon. Not. R. Astron. Soc.*, 276, 115

Chen, X. & Kamionkowski, M. 1999, *Phys. Rev. D*, 60, 104036

Chiba, T. 1999, *Phys. Rev. D*, 60, 083508

Chiba, T. 2001, *Phys. Rev. D*, 64, 103503

Chimento, L. P., Jakubi, A. S., & Pavón, D. 2000, *Phys. Rev. D*, 62, 063508

Cooray, A. R. & Huterer, D. 1999, *ApJ Letters*, 513, L95

Corasaniti, P. S., Bassett, B. A., Ungarelli, C., & Copeland, E. J. 2003, *Phys. Rev. Lett.*, 90, 091303

Corasaniti, P. S. & Copeland, E. J. 2002, *Phys. Rev. D*, 65, 043004

Couchman, H. M. P. 1991, *ApJ Letters*, 368, L23

Croft, R. A. C., Weinberg, D. H., Katz, N., & Hernquist, L. 1998, *ApJ*, 495, 44

Croton, D. J., Gaztañaga, E., Baugh, C. M., Norberg, P., Colless, M., Baldry, I. K., Bland-Hawthorn, J., Bridges, T., Cannon, R., Cole, S., Collins, C., Couch, W., Dalton, G., De Propris, R., Driver, S. P., Efstathiou, G., Ellis, R. S., Frenk, C. S., Glazebrook, K., Jackson, C., Lahav, O., Lewis, I., Lumsden, S., Maddox, S., Madgwick, D., Peacock, J. A., Peterson, B. A., Sutherland, W., & Taylor, K. 2004, *Mon. Not. R. Astron. Soc.*, 352, 1232

Damour, T. 1990, in New and Exotic phenomena, 285–+

Damour, T. & Nordtvedt, K. 1993, *Phys. Rev. D*, 48, 3436

Dodelson, S., Kaplinghat, M., & Stewart, E. 2000, *Phys. Rev. Lett.*, 85, 5276

Doran, M., Lilley, M., Schwindt, J., & Wetterich, C. 2001, *ApJ*, 559, 501

Eisenstein, D. J., Annis, J., Gunn, J. E., Szalay, A. S., Connolly, A. J., Nichol, R. C., Bahcall, N. A., Bernardi, M., Burles, S., Castander, F. J., Fukugita, M., Hogg, D. W., Ivezić, Ž., Knapp, G. R., Lupton, R. H., Narayanan, V., Postman, M., Reichart, D. E., Richmond, M., Schneider, D. P., Schlegel, D. J., Strauss, M. A., SubbaRao, M., Tucker, D. L., Vanden Berk, D., Vogeley, M. S., Weinberg, D. H., & Yanny, B. 2001, *Astronomical Journal*, 122, 2267

Eisenstein, D. J., Hu, W., & Tegmark, M. 1999, *ApJ*, 518, 2

Esposito-Farèse, G. & Polarski, D. 2001, *Phys. Rev. D*, 63, 063504

Ferreira, P. G. & Joyce, M. 1998, *Phys. Rev. D*, 58, 023503

Filippenko, A. V. 2003, in From Twilight to Highlight: The Physics of Supernovae, 171–+

Fosalba, P., Gaztañaga, E., & Castander, F. J. 2003, *ApJ Letters*, 597, L89

Fosalba, P. & Gaztanaga, E. 1998, *Mon. Not. R. Astron. Soc.*, 301, 535

Freedman, W. L., Madore, B. F., Gibson, B. K., Ferrarese, L., Kelson, D. D., Sakai, S., Mould, J. R., Kennicutt, R. C., Ford, H. C., Graham, J. A., Huchra,

J. P., Hughes, S. M. G., Illingworth, G. D., Macri, L. M., & Stetson, P. B. 2001, *ApJ*, 553, 47

Frieman, J. A. & Jaffe, A. H. 1992, *Phys. Rev. D*, 45, 2674

Fry, J. N. 1986, *ApJ Letters*, 308, L71

Gasperini, M., Piazza, F., & Veneziano, G. 2002, *Phys. Rev. D*, 65, 023508

Gaztañaga, E. 2002, *Mon. Not. R. Astron. Soc.*, 333, L21

Gaztañaga, E. & Lobo, J. A. 2001, *ApJ*, 548, 47

Giovi, F. & Amendola, L. 2001, *Mon. Not. R. Astron. Soc.*, 325, 1097

Gradwohl, B. & Frieman, J. A. 1992, *ApJ*, 398, 407

Hagiwara, K., Hikasa, K., Nakamura, K., Tanabashi, M., Aguilar-Benitez, M., Amsler, C., Barnett, R. M., Burchat, P. R., Carone, C. D., Caso, & coauthors, . 2002, *Phys. Rev. D*, 66, 010001

Halverson, N. W., Leitch, E. M., Pryke, C., Kovac, J., Carlstrom, J. E., Holzapfel, W. L., Dragovan, M., Cartwright, J. K., Mason, B. S., Padin, S., Pearson, T. J., Readhead, A. C. S., & Shepherd, M. C. 2002, *ApJ*, 568, 38

Hernquist, L. 1987, *ApJ Supplement Series*, 64, 715

Hinshaw, G., Spergel, D. N., Verde, L., Hill, R. S., Meyer, S. S., Barnes, C., Bennett, C. L., Halpern, M., Jarosik, N., Kogut, A., Komatsu, E., Limon, M., Page, L., Tucker, G. S., Weiland, J. L., Wollack, E., & Wright, E. L. 2003, *ApJ Supplement Series*, 148, 135

Holden, D. J. & Wands, D. 2000, *Phys. Rev. D*, 61, 043506

Hwang, J. & Noh, H. 2001, *Phys. Rev. D*, 64, 103509

Jenkins, A., Frenk, C. S., White, S. D. M., Colberg, J. M., Cole, S., Evrard, A. E., Couchman, H. M. P., & Yoshida, N. 2001, *Mon. Not. R. Astron. Soc.*, 321, 372

Kamionkowski, M. & Buchalter, A. 1999, *ApJ*, 514, 7

Khoury, J. & Weltman, A. 2004, *Phys. Rev. Lett.*, 93, 171104

Klypin, A., Macciò, A. V., Mainini, R., & Bonometto, S. A. 2003, *ApJ*, 599, 31

Knebe, A., Kravtsov, A. V., Gottlöber, S., & Klypin, A. A. 2000, *Mon. Not. R. Astron. Soc.*, 317, 630

Kogut, A., Spergel, D. N., Barnes, C., Bennett, C. L., Halpern, M., Hinshaw, G., Jarosik, N., Limon, M., Meyer, S. S., Page, L., Tucker, G. S., Wollack, E., & Wright, E. L. 2003, *ApJ Supplement Series*, 148, 161

Kovac, J. M., Leitch, E. M., Pryke, C., Carlstrom, J. E., Halverson, N. W., & Holzapfel, W. L. 2002, *NATURE*, 420, 772

Kravtsov, A. V. 1999, *Ph.D. Thesis*

Kravtsov, A. V., Klypin, A. A., & Khokhlov, A. M. 1997, *ApJ Supplement Series*, 111, 73

Kujat, J., Linn, A. M., Scherrer, R. J., & Weinberg, D. H. 2002, *ApJ*, 572, 1

Lee, A. T., Ade, P., Balbi, A., Bock, J., Borrill, J., Boscaleri, A., de Bernardis, P., Ferreira, P. G., Hanany, S., Hristov, V. V., Jaffe, A. H., Mauskopf, P. D., Netterfield, C. B., Pascale, E., Rabii, B., Richards, P. L., Smoot, G. F., Stompor, R., Winant, C. D., & Wu, J. H. P. 2001, *ApJ Letters*, 561, L1

Linder, E. V. 2003, *Phys. Rev. D*, 68, 083504

Lue, A., Scoccimarro, R., & Starkman, G. D. 2004, *Phys. Rev. D*, 69, 124015

Ma, C., Caldwell, R. R., Bode, P., & Wang, L. 1999, *ApJ Letters*, 521, L1

Macciò, A. V., Quercellini, C., Mainini, R., Amendola, L., & Bonometto, S. A. 2004, *Phys. Rev. D*, 69, 123516

Mainini, R., Macciò, A. V., Bonometto, S. A., & Klypin, A. 2003, *ApJ*, 599, 24

Mandelbaum, R., McDonald, P., Seljak, U., & Cen, R. 2003, *Mon. Not. R. Astron. Soc.*, 344, 776

Martel, H. 1995, *ApJ*, 445, 537

Melchiorri, A., Mersini, L., Ödman, C. J., & Trodden, M. 2003, *Phys. Rev. D*, 68, 043509

Moore, B. 1994, *NATURE*, 370, 629

Mota, D. F. & van de Bruck, C. 2004, *Astronomy & Astrophysics*, 421, 71

Multamäki, T., Gaztañaga, E., & Manera, M. 2003, *Mon. Not. R. Astron. Soc.*, 344, 761

Navarro, J. F., Frenk, C. S., & White, S. D. M. 1997, *ApJ*, 490, 493

Netterfield, C. B., Ade, P. A. R., Bock, J. J., Bond, J. R., Borrill, J., Boscaleri, A., Coble, K., Contaldi, C. R., Crill, B. P., de Bernardis, P., Farese, P., Ganga, K., Giacometti, M., Hivon, E., Hristov, V. V., Iacoangeli, A., Jaffe, A. H., Jones, W. C., Lange, A. E., Martinis, L., Masi, S., Mason, P., Mauskopf, P. D., Melchiorri, A., Montroy, T., Pascale, E., Piacentini, F., Pogosyan, D., Pongetti, F., Prunet, S., Romeo, G., Ruhl, J. E., & Scaramuzzi, F. 2002, *ApJ*, 571, 604

Padmanabhan, T. 1993, *Structure formation in the universe*, ed. Cambridge (Cambridge University Press)

Pearson, T. J. & Cosmic Background Imager Collaboration. 2002, "Bulletin of the American Astronomical Society", 34, 949

Pedichini, F., Giallongo, E., Ragazzoni, R., Di Paola, A., Fontana, A., Speziali, R., Farinato, J., Baruffolo, A., Magagna, C. E., Diolaiti, E., Pasian, F., Smareglia, R., Anaclerio, E., Gallieni, D., & Lazzarini, P. G. 2003, in Instrument Design and Performance for Optical/Infrared Ground-based Telescopes.

Edited by Iye, Masanori; Moorwood, Alan F. M. Proceedings of the SPIE, Volume 4841, pp. 815-826 (2003)., 815–826

Peebles, P. 1980, *Large−scale Structure of the Universe*, ed. Princeton (Princeton University Press)

Perlmutter, S., Turner, M. S., & White, M. 1999, *Phys. Rev. Lett.*, 83, 670

Pietroni, M. 2003, *Phys. Rev. D*, 67, 103523

Poli, F., Menci, N., Giallongo, E., Fontana, A., Cristiani, S., & D'Odorico, S. 2001, *Astrophys. J., Lett.*, 551, L45

Ratra, B. & Peebles, P. 1988, *Phys. Rev. D*, 37, 3406

Riess, A. G., Filippenko, A. V., Challis, P., Clocchiatti, A., Diercks, A., Garnavich, P. M., Gilliland, R. L., Hogan, C. J., Jha, S., Kirshner, R. P., Leibundgut, B., Phillips, M. M., Reiss, D., Schmidt, B. P., Schommer, R. A., Smith, R. C., Spyromilio, J., Stubbs, C., Suntzeff, N. B., & Tonry, J. 1998, *Astronomical Journal*, 116, 1009

Riess, A. G., Strolger, L., Tonry, J., Casertano, S., Ferguson, H. C., Mobasher, B., Challis, P., Filippenko, A. V., Jha, S., Li, W., Chornock, R., Kirshner, R. P., Leibundgut, B., Dickinson, M., Livio, M., Giavalisco, M., Steidel, C. C., Benítez, T., & Tsvetanov, Z. 2004, *ApJ*, 607, 665

Sahni, V. & Starobinsky, A. 2000, *International Journal of Modern Physics D*, 9, 373

Schuecker, P., Guzzo, L., Collins, C. A., & Böhringer, H. 2002, *Mon. Not. R. Astron. Soc.*, 335, 807

Scoccimarro, R., Sefusatti, E., & Zaldarriaga, M. 2004, *Phys. Rev. D*, 69, 103513

Scott, P. F., Carreira, P., Cleary, K., Davies, R. D., Davis, R. J., Dickinson, C., Grainge, K., Gutiérrez, C. M., Hobson, M. P., Jones, M. E., Kneissl, R.,

Lasenby, A., Maisinger, K., Pooley, G. G., Rebolo, R., Rubiño-Martin, J. A., Sosa Molina, P. J., Rusholme, B., Saunders, R. D. E., Savage, R., Slosar, A., Taylor, A. C., Titterington, D., Waldram, E., Watson, R. A., & Wilkinson, A. 2003, *Mon. Not. R. Astron. Soc.*, 341, 1076

Seljak, U. 1996, *ApJ*, 463, 1

Seljak, U. & Zaldarriaga, M. 1997, in Microwave Background Anistropies, 241–+

Sen, S. & Sen, A. A. 2001, *Phys. Rev. D*, 63, 124006

Seo, H. & Eisenstein, D. J. 2003, *ApJ*, 598, 720

Steidel, C. 1996, Bulletin of the American Astronomical Society, 28, 1313

Steidel, C. C. 1998, Proceedings of the National Academy of Science, 95, 22

Steinhardt, P. J., Wang, L., & Zlatev, I. 1999, *Phys. Rev. D*, 59, 123504

Szapudi, I., Frieman, J. A., Scoccimarro, R., Szalay, A. S., Connolly, A. J., Dodelson, S., Eisenstein, D. J., Gunn, J. E., Johnston, D., Kent, S., Loveday, J., Meiksin, A., Nichol, R. C., Scranton, R., Stebbins, A., Vogeley, M. S., Annis, J., Bahcall, N. A., Brinkman, J., Csabai, I., Doi, M., Fukugita, M., Ivezić, Ž., Kim, R. S. J., Knapp, G. R., Lamb, D. Q., Lee, B. C., Lupton, R. H., McKay, T. A., Munn, J., Peoples, J., Pier, J., Rockosi, C., Schlegel, D., Stoughton, C., Tucker, D. L., Yanny, B., & York, D. G. 2002, *ApJ*, 570, 75

Tocchini-Valentini, D. & Amendola, L. 2002, *Phys. Rev. D*, 65, 063508

Uzan, J. 1999, in Recent Developments in Theoretical and Experimental General Relativity, Gravitation, and Relativistic Field Theories, 300–+

Wands, D., Copeland, E. J., & Liddle, A. R. 1993, in Texas/PASCOS '92: Relativistic Astrophysics and Particle Cosmology, 647–+

Wang, L. & Steinhardt, P. J. 1998, *ApJ*, 508, 483

Wang, X., Tegmark, M., & Zaldarriaga, M. 2002, *Phys. Rev. D*, 65, 123001

Wetterich, C. 1988, *Nuclear Physics*, 302, 668

Wetterich, C. 1995, *Astronomy & Astrophysics*, 301, 321

Witten, E. 2000, hep-ph/0002297

Zlatev, I., Wang, L., & Steinhardt, P. J. 1999, *Phys. Rev. Lett.*, 82, 896